Novel Chalcopyrites for Advanced Photoelectrochemical Water Splitting

Final Technical Report

United States Department of Energy
Award Number DE-EE0008085

Submitted by
Hawai‘i Natural Energy Institute
School of Ocean and Earth Science and Technology
University of Hawai‘i at Mānoa

August 2023

Final Technical Report

Project Title:	Novel Chalcopyrites for Advanced Photoelectrochemical Water Splitting
PI:	Dr. Nicolas Gaillard Phone: 808-956-2342 Email: ngaillar@hawaii.edu
Project Period:	October 1, 2017 – December 31, 2021
Recipient:	University of Hawaii / Hawaii Natural Energy Institute 2440 Campus Road, Box 368 Honolulu, HI 96822
Award Number:	DE-EE0008085
Working Partners:	University of Nevada, Las Vegas (C. Heske, A. Hua, J. Kearney, J. Napoles, D. Hauschild, L. Weinhardt) Stanford University (T. Jaramillo and D. Palm) Lawrence Livermore National Laboratory (T. Ogitsu and J.Varley) National Renewable Energy Laboratory (K. Zhu, C. Muzzillo, A. Zakutayev and I. Khan) Lawrence Berkeley National Laboratory (J. Cooper and F. Babbe)

Executive Summary

With the support of DoE's EERE office, our team has established a unique tool-chest of capabilities, including theoretical modeling (Lawrence Livermore National Laboratory: LLNL), state-of-the-art synthesis (Hawaii Natural Energy Institute: HNEI, Stanford, and the National Renewable Energy Laboratory: NREL) and advanced materials and interfaces characterization (University of Nevada, Las Vegas: UNLV, and Lawrence Berkeley National Laboratory: LBNL), to accelerate the development of high efficiency and durable chalcopyrite materials for advanced photoelectrochemical (PEC) water splitting. Using this synergistic approach, we have successfully created new wide bandgap chalcopyrite photocathodes generating over 10 mA/cm^2, developed innovative strategies to protect them from corrosion, and engineered novel integration methods to circumvent thin film materials mechanical, chemical and thermal incompatibility.

In Task 1 "Modeling and synthesis of chalcopyrite photocathodes", we expanded our library of wide bandgap chalcopyrites for PEC water splitting. With support from LLNL's "Computational Materials Diagnostics and Optimization of PEC Devices", LBNL's "photophysical" and NREL's "I-III-VI Compound Semiconductors for Water-Splitting" nodes, we investigated two new chalcopyrite candidates for PEC water splitting: $Cu(In,Al)Se_2$ and $Cu(In,B)Se_2$. We also further developed ordered vacancy compounds, such as $CuGa_3Se_5$, with unprecedented durability during PEC waters splitting in acidic solutions.

In Task 2 "Interfaces engineering for enhanced efficiency and durability", we addressed both the non-ideal band-edge positions of chalcopyrites with respect to water redox potentials, as well as their chemical instability under PEC water splitting, with a buried-junctions approach. With help from NREL's "High-Throughput Experimental Thin Film Combinatorial Capabilities" and "Corrosion Analysis of Materials" nodes, we engineered environmentally friendly n-type buffers, including $Mn_xZn_{1-x}O$, to adjust the chalcopyrite band-edge positions and achieved photovoltages as high as 925 mV. Also, we integrated non-precious catalytic-protecting layers, such as WO_3, to enhance the water splitting long-term stability of chalcopyrite absorbers.

Finally, in Task 3 "Hybrid photoelectrode device integration", we proposed an innovative method to bond wide bandgap photocathodes onto narrow bandgap PV drivers at room temperature using conductive polymers. Our *semi-monolithic* approach addressed fundamental processing incompatibility issues, as both the photocathode and the PV driver are processed separately. Proof-of-concept whole-chalcopyrite tandems were obtained by consecutive exfoliation and transfer of fully integrated 1.85 eV $CuGa_3Se_5$ and 1.13 eV $CuInGaSe_2$ stacks from their Mo/SLG substrates onto a new single FTO host substrate.

Acknowledgments

This material is based upon work supported by the U.S. Department of Energy's Office of Energy Efficiency and Renewable Energy (EERE) under the Hydrogen Fuel Cells Technology Office (HFTO) under Award Number DE-EE0008085. N. Gaillard would like to express his utmost gratitude to all faculty members, students, postdoctoral fellows, and senior scientists involved in this multi-year program, including Drs. Chong, Horsley, Prasher, Septina and Mr. Deangelis at the University of Hawaii, Prof. Jaramillo, Drs. Hellstern and Palm at Stanford, Prof. Heske, Drs. Blum, Weinhardt and Carter at UNLV, Drs. Ogitsu and Varley at LLNL, Drs. Cooper and Babbe at LBNL, and Drs. Zhu, Muzzillo, Contreras, Wang and Deutsch at NREL.

Table of Contents

1. Introduction

a. Background

For the past two decades, the Hawaii Natural Energy Institute (HNEI) at the University of Hawaii has been conducting cutting-edge photoelectrochemical (PEC) water-splitting research on advanced materials, functional interfaces, and integrated devices. HNEI's major contributions to the field include the development of low-cost PEC material classes and their integration into standalone multi-junction Hybrid Photo-Electrode (HPE, Figure 1a) devices. Such devices are capable of unassisted water-splitting with solar-to-hydrogen (STH) efficiencies in the range of 3.1%[1] (WO_3) to 7.8% (a-Si).[2] With the support of DOE's EERE office, HNEI partnered in 2014 with the University of Nevada, Las Vegas (UNLV, Prof. Heske), Stanford University (Prof. Jaramillo), the National Renewable Energy Laboratory (NREL, Drs. Wang, Deutsch, Contreras and Zhu) and Lawrence Livermore National Laboratory (LLNL, Dr. Ogitsu) to develop the next generation of thin film materials for PEC water-splitting. In this project, we established a team with a unique tool chest of ***theoretical modeling***, ***state-of-the-art synthesis,*** and ***advanced material and interface characterization*** to accelerate the development of promising wide-bandgap chalcopyrite materials.

The chalcopyrite materials class, typically identified by its most popular alloy $Cu(In,Ga)Se_2$ (CIGSe), provides exceptionally good candidates for PEC water-splitting and has the potential to meet DOE EERE's ultimate target of \$2/kg of H_2. A key asset of this bandgap tunable thin film semiconductor material is its outstanding photon-to-electron conversion (> 90%) and Faradaic (> 85%) efficiencies, two major requirements for efficient H_2 production via PEC water-splitting. Using our synergistic *modeling-synthesis-characterization* approach, we have successfully developed multiple photocathode alloys compatible with the HPE integration, including $CuGaSe_2$,[3] $Cu(In,Ga)S_2$ (CIGS),[4] $CuGa(S,Se)_2$ (CGSSe),[5] and $CuGa_3Se_5$.[6] Our studies demonstrate that these 1.7 – 1.8 eV bandgap materials can generate photocurrent densities above 10 mA/cm^2 (Figure 1b), a key milestone to achieve STH efficiencies greater than 12%. Simultaneously, our group has developed innovative strategies to protect chalcopyrites from corrosion using ultra-thin MoS_2 layers, achieving 350 hours of continuous water-splitting operation at photocurrent densities (8 mA/cm^2) relevant to a STH efficiency of 10%. Finally, we have made progress toward monolithic HPE device integration with the development of temperature-resistant transparent conductive oxides (TCOs) to serve as intermediate contact layers between each sub-cell of a multi-junction HPE device. These TCOs were integrated into monolithic Si/TCO/$CuGaSe_2$ structures, generating open circuit voltages over 1.23 V.

b. Project goals

The current record STH efficiency of the chalcopyrite material class (10%) was achieved using three series-connected CIGSe PV cells with identical bandgaps.[7] However, this co-planar structure makes poor use of area, which in turn limits the overall STH efficiency. The HPE multi-junction approach is a preferred architecture, making better use of the solar spectrum per unit area for higher conversion efficiency. Our research program aimed to develop novel wide-bandgap chalcopyrite photocathodes compatible with the multi-junction HPE integration scheme. Our project was subdivided into 3 tasks, each targeting specific improvements towards *high efficiency*, *low-cost*, and *durable* chalcopyrite-based PEC devices.

To demonstrate the potential of the chalcopyrite to meet DOE's cost targets, we conducted a cost analysis using the H2A model. All calculations were done using so-called "Type 4" hydrogen production reactors equipped with thin film-based absorber planar arrays, optical concentrators, and solar tracking systems. For the base-case scenario, we assumed a total device cost of $100/m^2 and 20% STH efficiency. A 25× concentration factor was chosen to reduce constrains on the materials durability target. A 2-year PEC material lifetime was used for the base-case scenario, equivalent to 4,400 hours of continuous operation (assuming a 25% capacity factor for a diurnal cycle). The Tornado plot in Figure 1c presents the effect of STH efficiency (15, 20 and 25%), materials lifetime (0.5, 2 and 10 years) and cost ($60, $100 and $200/m^2) on the cost of hydrogen. Each calculation reported in this figure represents the variation of a single parameter from the base-case scenario (20%, 2-year durability, $100/m^2). Clearly, the STH efficiency is the variable with the most leverage on PEC hydrogen production cost. Decreasing efficiency to 15%, which is the maximum theoretical efficiency for any co-planar device, leads to a cost of $4.09/kg H_2 (2-year durability, $100/m^2). Increasing the STH efficiency to 25% leads to a cost of $2.54/kg H_2 (2-year durability, $100/m^2). As we show later, this efficiency is theoretically achievable with chalcopyrite-based multi-junction PEC devices. Our calculations also show that increasing both STH efficiency to 25% and materials durability to 10 years could lead to a cost per kg of H_2 of $1.95, meeting DOE's hydrogen production cost target of $2/kg H_2. Ultimately, it is the strong economic lever that comes from having a significantly higher efficiency limit that makes investigating HPE devices a particularly relevant route to achieve low-cost water-splitting.

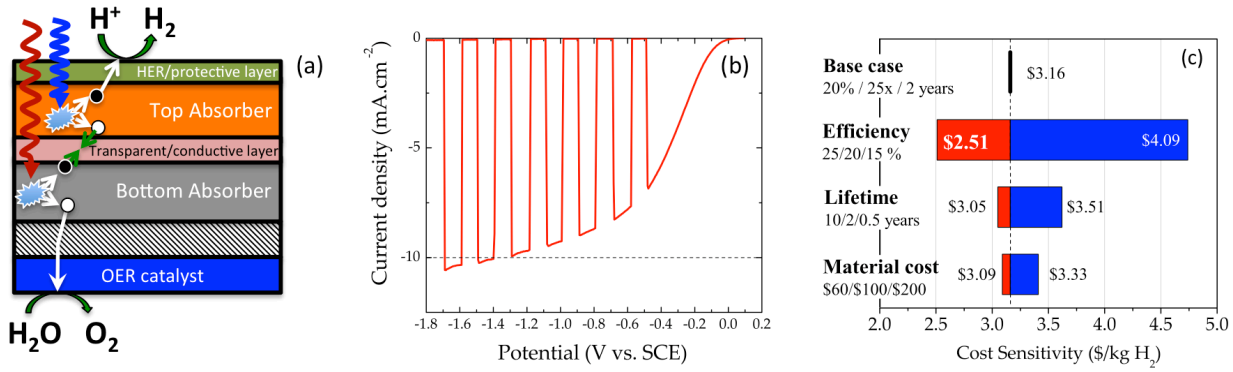

Figure 1. (a) Schematic diagram of a multi-junction HPE device, (b) linear sweep voltammetry measured on NREL's 1.8 eV-bandgap $CuGa_3Se_5$ photoelectrode (0.5M H_2SO_4, simulated AM1.5$_G$ illumination), and (c) effect of efficiency, materials lifetime, and cost on the cost of H_2 for a "Type 4" PEC reactor (25×).

c. Technical barriers

The previous section briefly discussed the relevant information that aided in identifying this project's specific technical barriers as outlined in DoE EERE's Multi-Year Research, Development, and Demonstration Plan, namely the achievable STH efficiency as well materials durability and manufacturing cost. The following list gives the four primary technical barriers which needed to be addressed to achieve DoE's ultimate targets for hydrogen production costs:

Material Efficiency barrier: Achieving STH efficiencies above 15% requires materials with proper solid-state properties, as demonstrated with high-purity III-V PEC devices. In this regard, we have recently identified the top wide-bandgap chalcopyrite absorbers (e.g. CIGS, CGSSe) as the main bottleneck of our HPE devices.[8] In fact, our optical and electronic studies thus far show that wide-bandgap chalcopyrites containing gallium and/or sulfur exhibit poor optical transmission (compared to their In- and Se-containing relatives), resulting in tandem structures with sub-optimal photocurrent densities. This could be due in part to Ga-related defects well-known in the PV community.

Research performed in this program to address this barrier: with support from LLNL's "Computational Materials Diagnostics and Optimization of PEC Devices" node, we evaluated passivation strategies (e.g., alkali doping) to improve the quality of the Ga-containing wide-bandgap chalcopyrite photocathodes studied by our team, including $CuGaSe_2$, CIGS, CGSSe, and $CuGa_3Se_5$. We also investigated novel wide-bandgap absorbers, already identified by the LLNL theory group, that contain neither gallium nor sulfur, such as $Cu(In,Al)Se_2$ and $Cu(In,B)Se_2$. These activities were supported by advanced spectroscopic analysis (UNLV) to characterize the absorber electronic structure and chemical composition. Figure 2 illustrates an example of our synergistic approach, in which *theoretical modeling*, *state-of-the-art synthesis*, and *advanced characterization* were integrated for the development of bandgap-tunable CGSSe photocathodes.

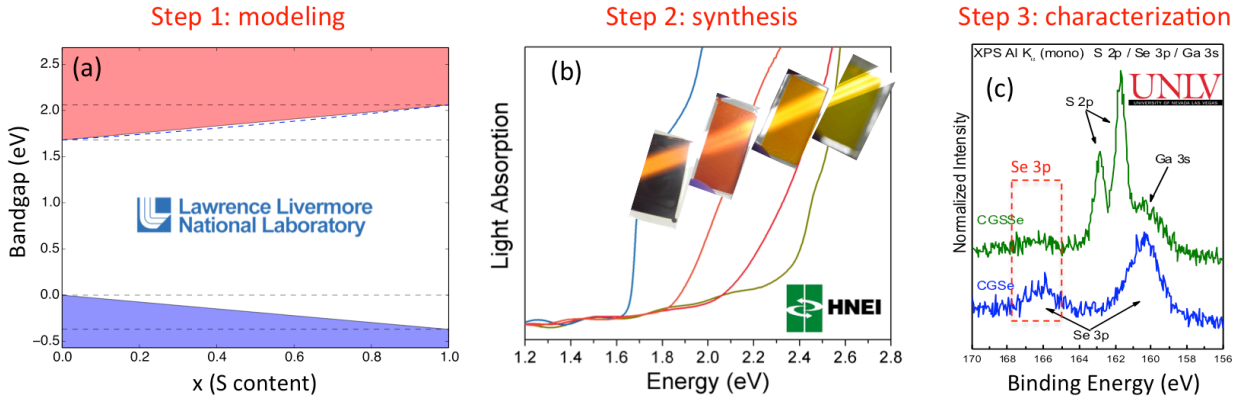

Figure 2. The *theory-synthesis-characterization* synergy used by our team to develop wide-bandgap chalcopyrites. (a) Calculated bandgap of $CuGa(Se_{1-x}S_x)_2$ as a function of x (LLNL), (b) Tauc plots of $CuGa(S,Se)_2$ samples containing various amounts of sulfur and selenium (HNEI), and (c) high-resolution X-ray photoelectron spectra measured on $CuGaSe_2$ and $CuGa(S,Se)_2$ thin film absorbers (UNLV).

Synthesis and Manufacturing barrier: Our techno-economic analysis revealed that the cost for the complete PEC device must remain under \$100/m^2 to meet DOE's ultimate target of \$2/kg H_2. Using industrial, well-established vacuum technologies (co-evaporation), Solar Frontier, Inc. currently manufactures commercial single-junction $CuInSe_2$ PV modules with 14% efficiency at \$0.63/W, or \$100/m^2. Building chalcopyrite-based tandem devices today with vacuum-based processes would lead to PEC materials cost of at least double that of single junction modules (i.e. > \$200/m^2). Thus, it is critical to investigate alternative deposition methods to meet DOE's materials cost target.

Research performed in this program to address this barrier: With support from NREL's "I-III-VI Compound Semiconductors for Water-Splitting" node, we developed a low-cost *solution*-based technique to fabricate bandgap-tunable chalcopyrite materials. This method relied on environmentally friendly molecular inks (Figure 3a) that can be easily printed using high-throughput techniques. Printed films were further annealed near ambient pressure to form dense and highly crystalline thin films (Figure 3b), comparable to those obtained with conventional vacuum-based processes. This approach was demonstrated by HNEI with printed $Cu_2ZnSnSe_4$ (CZTSe) and $CuInSe_2$ (CISe) solar cells with 7% (Figure 3c) and 12%[9] efficiency, respectively.

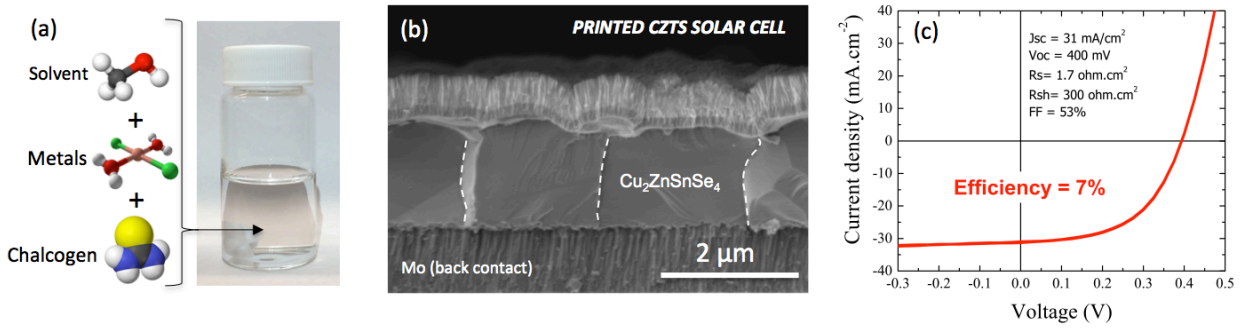

Figure 3. (a) HNEI's CZTSe molecular ink, (b) cross-sectional scanning electron micrograph of a CZTSe solar cell made from printed molecular ink, and (c) electrical characteristic of HNEI's 7% CZTSe solar cell.

Durability barrier: Chalcopyrite photocathodes suffer from non-ideal band-edge positions with respect to the redox potentials of water-splitting. We have overcome this before by depositing n-type CdS on $CuGaSe_2$ to create an additional electric field, as shown in Figure 4a. Although highly effective (anodic shift of 800 mV), this surface treatment is not durable (Figure 4b). Not only is this short lifetime insufficient for achieving cost-effective hydrogen production, but the use of CdS and its dissolution into the electrolyte also raises environmental concerns.

Research performed in this program to address this barrier: A 2-year PEC material replacement schedule is equivalent to 4,400 hours of continuous operation. This target represents only 3 times the durability already achieved by Stanford on atomically flat Si electrodes protected with a 10 nm thick MoS_2 film (Figure 4c). However, achieving a pinhole-free MoS_2 coating on rough chalcopyrite surfaces is challenging, currently resulting in a durability of 350 hours; a promising value, but with further work needed. With support from NREL's "Corrosion Analysis of Materials" node, we developed conformal deposition that yielded pinhole-free MoS_2 layers on CdS-coated chalcopyrites, successfully extending durability in strong sulfuric acid electrolyte.[10] Also, we investigated more environmentally friendly buffers, such as In_2S_3 and MgZnO[11] with help from NREL's "High-Throughput Experimental Thin Film Combinatorial Capabilities" node. Characterization of buffers and protective layers was performed at UNLV.

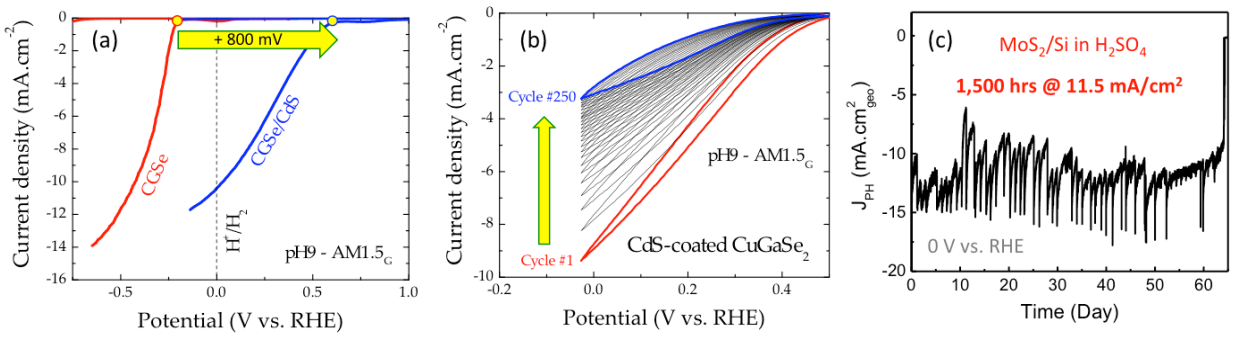

Figure 4. (a) Linear sweep voltammetry scans measured at HNEI on a bare and a CdS-coated $CuGaSe_2$ photocathode, (b) 250 cyclic voltammetry scans measured consecutively on a $CuGaSe_2$/CdS sample (HNEI), and (c) 65-day chronoamperometry study, measured at Stanford on MoS_2-coated Si in H_2SO_4 at 0 V vs. RHE.

Integrated Device Configurations barrier: Materials compatibility is the biggest challenge in multi-junction device integration. Essentially, the deposition process of each layer must not damage the previous layers and interfaces in any way. With current chalcopyrite PV technology, it is impossible to fabricate high efficiency monolithic multi-junction devices by directly depositing a wide-bandgap photocathode, because the required temperatures for high quality films ($T_{process}$=500°C) deteriorate the underlying narrow-bandgap CIGSe device.[12]

Research performed in this program to address this barrier: When chalcopyrite thin films are deposited on molybdenum substrates, interfacial $Mo(S,Se)_2$ layers naturally form (Figure 5a). The chalcopyrite absorbers can be peeled from the substrates by mechanically delaminating these interfacial layers. (Figure 5b). We proposed to take advantage of this unique situation to transfer wide-bandgap chalcopyrites grown on molybdenum substrates onto fully processed CIGSe PV drivers to create a "semi-monolithic" device. With this approach, both devices can be integrated independently without any processing constraints. Transparent conductive polymers, such as microsphere/polyepoxy composites, were developed to contact the photocathode and the PV driver. Quantum efficiency (QE) measurements of a CIGSe solar cell shaded by a $CuGaSe_2$ photocathode confirmed that such semi-monolithic device could generate photocurrent densities (10 mA/cm^2) relevant to STH efficiencies > 10% (Figure 5c).

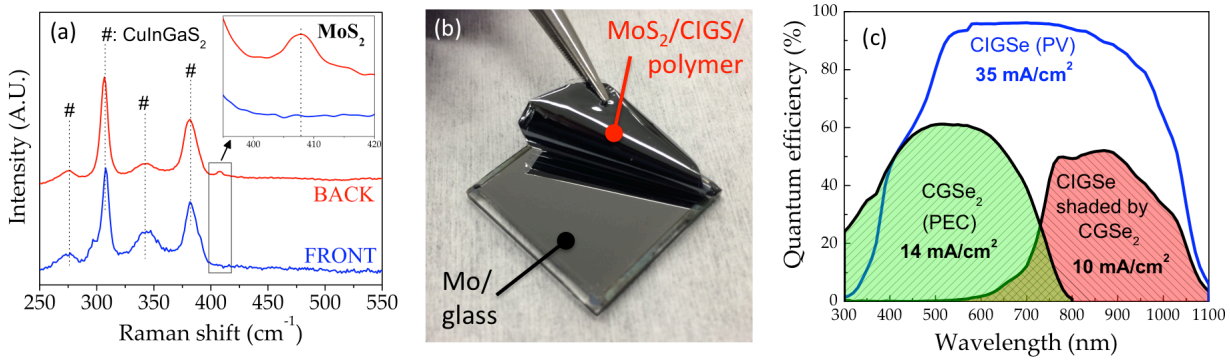

Figure 5. (a) Raman shift measured on the front side and back side of $CuInGaS_2$ (HNEI), (b) exfoliated $CuInGaS_2$/MoS_2 stack bonded to a polymer (HNEI), and (c) QE measured on a 1.1 eV $CuInGaSe_2$ solar cell, a 1.6 eV $CuGaSe_2$ photocathode, and on $CuInGaSe_2$ shaded by $CuGaSe_2$ (HNEI).

2. Work Plan

Our past research successes would not have been possible without the close collaboration with other research groups to combine advanced synthesis techniques, unique characterization, and theoretical approaches, as well as accurate test protocols for PEC device benchmarking. Therefore our multi-disciplinary ***modeling-synthesis-characterization*** approach remained the foundation of our cross-cutting research team and was instrumental to further develop chalcopyrites for high-efficiency water-splitting. Our program was supported by 5 nodes within the HydroGEN consortia: 1) NREL's "I-III-VI Compound Semiconductors for Water-Splitting" (hereafter the "Chalcopyrite Node"), "High-Throughput Experimental Thin Film Combinatorial Capabilities" (the "Combinatorial Node"), "Corrosion Analysis of Materials" (the "PEC Node"), LLNL's "Computational Materials Diagnostics and Optimization of PEC Devices" (the "Theory Node") and LBNL's "Photophysical" Node. A brief description of each task is outlined below. Specific milestones and Go/NoGo metrics for this program are provided in Table 1.

Task 1: Modeling and Synthesis of Chalcopyrite Photocathodes

Objectives of this Task: Further validate our materials development strategy with integrated *theoretical modeling*, *state-of-the-art synthesis*, and *advanced characterization*. In **sub-task 1.1 – defect passivation**, we modelled and validated methods to heal point defects in Ga-based chalcopyrites, including CIGS, CGSSe, $CuGaSe_2$, and $CuGa_3Se_5$. In **sub-task 1.2 – printed chalcopyrites**, we develop two new promising Ga-free, wide-bandgap chalcopyrite candidates for PEC water-splitting: $Cu(In,Al)Se_2$ and $Cu(In,B)Se_2$.

Theoretical Foundation: Our team members at LLNL have calculated (Figure 6a) that Ga_{Cu} anti-site defects are deep donors in $CuGaSe_2$ and $CuGaS_2$, which agrees with other theoretical work done to explain the limited performance of high-Ga CIGSe PV devices. These defects are also ~0.5 eV deeper in $CuGaS_2$ than in $CuGaSe_2$, suggesting that they are even more harmful in sulfides. Such deep defects can cause Fermi level pinning if their concentrations are high enough, and could explain the voltage deficit measured on high-Ga CIGS samples [$Ga/(Ga+In) > 0.5$, $E_G > 1.8$ eV] currently investigated by our team. Thus, theory was used to guide materials synthesis and develop passivation strategies to improve the solid-state properties of these chalcopyrites, and at the same time investigate other promising chalcopyrites that do not contain gallium.

Synthesis Approach: The "Chalcopyrite Node" and HNEI synthesized chalcopyrite materials with *proven* and *scalable* techniques. In **sub-task 1.1**, $CuGaSe_2$, $CuGa_3Se_5$, CIGS, and CGSSe were synthesized by direct vacuum co-evaporation and post-deposition sulfurization annealing of metal alloys or selenides (Figure 6b). Passivation of these Ga-containing absorbers was accomplished primarily by alkali doping, following recommendations from the "Theory Node". In **sub-task 1.2**, HNEI established a baseline for the *solution*-based approach by first synthesizing $CuInSe_2$ absorbers. Aluminum or boron-based reagents (e.g., chlorides) were then added to create Ga-free $Cu(In,Al)Se_2$ or $Cu(In,B)Se_2$ chalcopyrites. The "Theory Node" assisted by calculating their optimal compositions and identify the best synthesis conditions (Figure 6c).

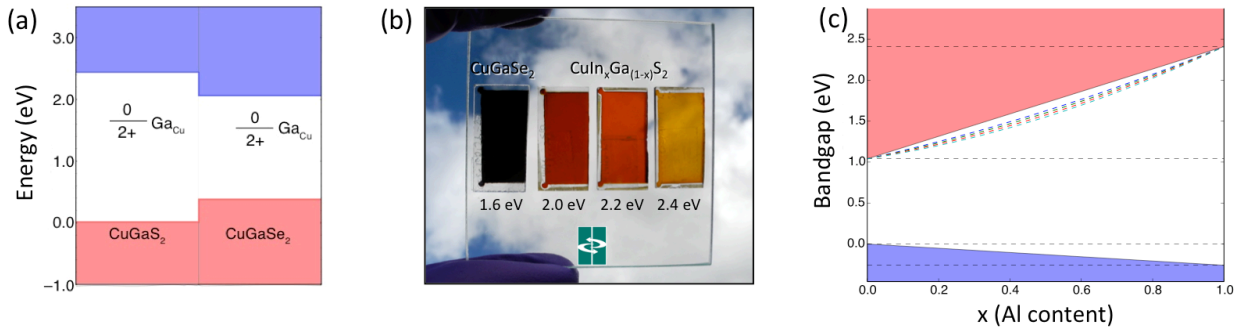

Figure 6. (a) Calculations of trap levels associated with expected defects in $CuGaS_2$ and $CuGaSe_2$ (LLNL). A (+2/0) deep donor transition level of the Ga_{Cu} anti-site relative to the band edges is included, (b) photograph of HNEI's bandgap-tunable CIGS obtained from post-deposition sulfurization of co-evaporated selenide materials, and (c) calculated bandgap of $CuIn_{1-x}Al_xSe$ as a function of x (LLNL).

Task 2: Interface Engineering for Enhanced Efficiency and Durability

Objectives of this Task: Use a buried junction to address the non-ideal band-edge positions of chalcopyrites with respect to water redox potentials, as well as chemical material instabilities during operation. In **sub-task 2.1 – interface energetics**, we developed new n-type buffers, then combine them with p-type absorbers to adjust the band-edges. In **sub-task 2.2 – interface durability**, we integrated non-precious catalytic-protecting layers to enhance the water-splitting efficiency of buffer layer/chalcopyrite systems and ensure long-term stability. We also developed techniques to interrogate chalcopyrite photoelectrodes and understand the durability limitations of devices as currently synthesized.[10]

Theoretical Foundation: Our approach relied on the combination of two unique surface treatments to address distinct fundamental issues. The role of the buffer layer was to enhance charge separation in the photocathode. In an ideal situation, the conduction band offset (CBO) between this layer and the absorber is close to zero. In the case of a positive CBO, an energetic barrier, or "spike", can block electrons from reaching the photocathode surface (e.g. $CuGaSe_2$/ZnS in Figure 7a). A negative CBO could also significantly impede charge flow by forming a "cliff" with many surface recombination sites ($CuGaSe_2$/CdS and, more pronounced, $CuGaSe_2$/ZnO in Figure 7a). Thus, the surface energetics of both the chalcopyrite absorber and buffer must be carefully modeled, characterized, and tailored to identify the best buffer/chalcopyrite combinations for optimum charge carrier separation. The chalcopyrite/buffer junction must also be protected to ensure long-term PEC hydrogen production, which can be achieved with "impermeable" layered structures (such as MoS_2), intrinsically stable materials (TiO_2, WO_3), or a combination of both.

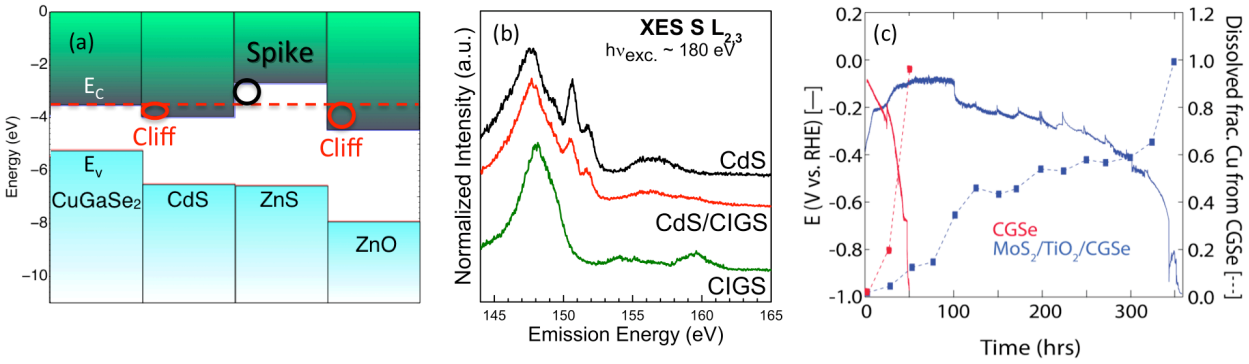

Figure 7. (a) Calculated unstrained band offsets of $CuGaSe_2$ with respect to CdS, ZnS, and ZnO (LLNL), (b) S $L_{2,3}$ soft X-ray emission spectra measured by UNLV on a bare and CdS-coated CIGS sample, as well as a CdS reference sample. (c) Dissolved fraction of copper in electrolyte measured at Stanford by ICPMS during a 350-hr durability test on a bare and a MoS_2/TiO_2-coated $CuGaSe_2$ photocathode.

Synthesis Approach: In **sub-task 2.1**, the "Combinatorial Node", Stanford and HNEI will integrate promising buffers identified by theory onto chalcopyrite absorbers using *scalable* and *proven* deposition techniques. Bandgap-tunable $ZnO_xS_{(1-x)}$ buffers will be fabricated using reactive-sputtering. In_2S_3 and $Zn_xIn_{(1-x)}Se$ layers will be synthesized using various solution-based approaches, including chemical bath deposition (CBD) and printing techniques with molecular inks. In **sub-task 2.2**, we will continue to study MoS_2 (evaporated or deposited by atomic layer deposition) as a catalytic protecting layer, because it shows high HER activity and has an excellent track record for durability on other photocathode systems. However, we will simultaneously be investigating novel alternatives such as cobalt phosphide (CoP), which has also shown excellent HER activity and stability. We will also evaluate other passivation strategies using intrinsically stable materials, such as SiO_x and TiO_2, which will be fabricated using polydimethylsiloxane and titanium butoxide polymer, respectively.

Validation Strategy: In **sub-task 2.1**, HNEI will first perform UV-vis spectroscopy to determine the bandgaps of the proposed buffers. Then, the UNLV team will analyze the chemical purity of buffers and their electronic band alignment with certain wide-bandgap chalcopyrites using a broad suite of spectroscopic techniques (including XPS and XES, Figure 7.b). Simultaneously, HNEI will measure the solid-state properties (e.g., open-circuit voltage) of the same samples under simulated $AM1.5_G$ illumination. Through periodic data discussions between the experimentalists and theorists in our team, we will determine how the models can be adjusted to better predict chalcopyrite/buffer band alignments (month 30 milestone). In **sub-task 2.2**, Stanford and UNLV will use post-failure characterization to provide information on chemical state changes and degradation of the catalytic and buffer layers. Inductively-coupled plasma mass spectrometry (ICP-MS) of the electrolyte will provide evidence of the extent of degradation to the absorber and interface layers (Figure 7.c). Nano-scale scanning electron microscopy (SEM) will allow observation of changes in the conformity or formation of pinholes in the catalytic overlayers over the duration of PEC operation. Finally, *in situ* microscopy will allow for the coupling of optical microscopy and Raman spectroscopy to observed changes in the electrode surfaces during operation. The targets for this sub-task are 500 hrs (Go/NoGo for year 2) and 1,000 hours (month 33 milestone) of continuous operation at 8 mA/cm^2.

Task 3: Hybrid Photoelectrode Device Integration

Objectives of this Task: Develop viable alternative device integration schemes to create high-efficiency chalcopyrite-based tandem HPE devices. Our innovative approaches bridged the gap between monolithic integration and the mechanical stack approach commonly used in PEC research. It also offered a new platform to integrate wide-bandgap chalcopyrites with other "incompatible" low-cost PV technologies, including a-SiGe, CdTe, and perovskites. In **sub-task 3.1 – conductive polymers**, we developed alternative transparent conductive layers using epoxy/miscrosphere composites, aiming for optoelectronic properties comparable to that of vacuum-processed TCOs (e.g., indium-doped tin oxide). In **sub-task 3.2 – semi-monolithic HPE device,** we used our conductive polymers as both bonding materials and intermediate window layers to combine chalcopyrite photocathodes with fully processed PV drivers.

Theoretical Foundation: Figure 8a shows calculated achievable STH efficiencies for a device with losses typical for known solar absorbers: 0.49 eV free energy loss from each semiconductor, and overpotentials for Pt (HER) and RuO_2 (OER) catalysts.[13] The achievable STH efficiency for an HPE system consisting of a 1.23 eV PV driver and 1.85 eV photocathode is 22.8%. Reducing free energy loss from each absorber to 0.39 eV and adjusting bandgaps to 1.13 eV (PV driver) and 1.74 eV (photocathode), respectively, increases STH efficiency to 25.9% (Figure 8b). This model shows that there is a pathway towards achieving STH efficiency > 20% using photocathodes with bandgaps in the 1.6 – 2.0 eV range, i.e., the range that chalcopyrites can be tuned to cover.

Synthesis Approach: In **sub-task 3.1**, HNEI developed several polymers made of conductive media dispersed into transparent epoxies. The concentration of the conductive media was tuned to achieve optimal conductivity and transparency. SEM analysis were used to characterize conductive media dispersion into the host epoxy. In **sub-task 3.2**, HNEI validated the proposed HPE architecture with model $CuGaSe_2$ photocathodes deposited on Mo-coated glass, and CIGSe PV drivers. The photocathodes were then exfoliated from the glass/Mo to construct semi-monolithic HPE devices (Figure 8c). Best integration practices established with model systems were used in the final phase to create chalcopyrite-based tandem HPE devices.

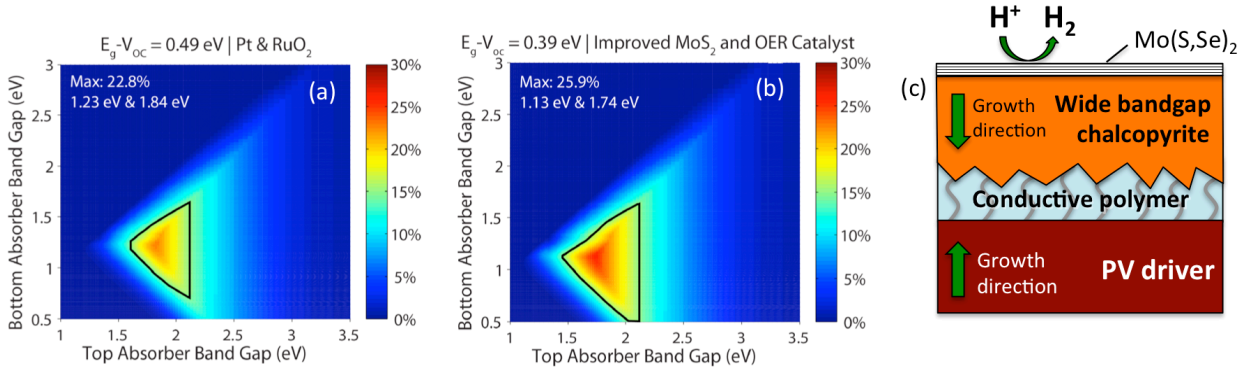

Figure 8. Contour plots showing achievable STH based on (a) commonly known semiconductors and catalysts, and (b) improved semiconductors and catalysts (Stanford). The black triangles demarcate the window within which > 15% STH is achievable. (c) Schematic of the proposed semi-monolithic HPE device.

Table 1. Project milestones and Go/NoGo criteria

Milestone ID	Description	% complete
1.1-1	A printed polycrystalline chalcopyrite thin film material made of grains at least 500 nm across and with impurity concentration less than 15%.	100%
3.1-1	Produce a nanowire and epoxy based composite demonstrating a sheet resistance below 200 Ω/sq and transparency > 70%.	100%
2.1-1	Demonstrate a stabilized chalcopyrite photocathode that retains 90% of its copper content after 100 hrs of continuous operation to achieve an initial photocurrent density of 8 mA/cm2 under simulated AM1.5G illumination.	100%
GNG#1	**A solution-processed CuIn(S,Se)2-based PV device with a short-circuit photocurrent density corresponding to at least 70% of the absorber's theoretical limit (and free-electron losses (Eg – Voc.q) less than 600 mV.**	**100%**
GNG#2	**Demonstrate 500 hrs stability in a photoelectrode operating under simulated AM1.5G illumination at a fixed potential that achieves an initial photocurrent of 8 mA/cm2 and does not drop below 5 mA/cm2 over the duration of the test.**	**100%**
2.1-1	Determine the factors contributing to increased open circuit voltage of at least 900 mV with a MgZnO:Ga-coated and surface-treated wide bandgap chalcopyrite absorbers under simulated AM1.5G illumination, with a stretch goal of demonstrating over 200 mV improvement over the baseline by the end of year 2.	100%
1.2-2	A printed polycrystalline $Cu(In,Al,B)Se_2$ thin film material losing less that 50% of photocurrent and photovoltage after exfoliation/transfer.	100%
2.2-2	Retain 90% of metal content in a thin, transparent protective coating over the course of 100 hrs of electrocatalytic HER testing at -10 mA/cm^2.	90%
GNG#1	**Using a chalcopyrite photocathode, sustain hydrogen production (initially exceeding -8 mA/cm^2) at 90% of initial photocurrent density for 200 hours.**	**100%**
GNG#2	**Create a semi-monolithic tandem device exhibiting a Voc that is at least 50% of the sum of the Voc's of the individual cells.**	**100%**
1.2-3	A printed single-phase polycrystalline $Cu(In,Al,B)(S,Se)_2$ thin film material showing photovoltage greater than 700 mV.	100%
2.1-3	Demonstrate an open circuit voltage greater than 1,000 mV on at least 10 MgZnO:Ga-coated wide bandgap chalcopyrite absorbers integrated on a Mo substrate under simulated AM1.5 G illumination.	Not met
2.2-4	Retain 90% of metal content in a thin, transparent protective coating over the course of 300 hrs of electrocatalytic HER testing at -10 mA/cm^2.	30%
Project deliverable	**A standalone semi-monolithic chalcopyrite-based device capable of producing renewable hydrogen with an STH efficiency of at least 5%, with a stretch goal of 10%.**	20%

Validation Strategy: In **sub-task 3.1**, the transparency and electrical conductivity of our polymers were characterized by means of UV-vis spectroscopy and 4-point probe electrical measurements, respectively. The target for this sub-task was composite with resistivity lower than 200 Ω/□ and transparency greater than 70%. In **sub-task 3.2**, the photoconversion efficiency of the semi-monolithic devices was characterized by means of solid-state and PEC analyses. The target for this sub-task is a semi-monolithic system with STH efficiency of at least 10% STH. The information gathered in **Task 3** regarding the optical, electric, and electrochemical loss mechanisms in our semi-monolithic devices will be used to update tandem device modeling, avoid potential pitfalls in the proposed structure, and identify avenues for improvement.

3. Achievements in Task 1 "Modeling and Synthesis of Chalcopyrite Photocathodes"

a. Theoretical modeling

Chalcopyrite alloy properties: The targeted design of solar absorbers for photoelectrochemical hydrogen production requires careful tuning of the band gap and band edges to optimize the desired absorption characteristics and necessary charge transport, respectively. Lower band gap chalcopyrite alloys based on $CuInSe_2$ and $CuGaSe_2$ have band gaps (~1.2 eV) and strong absorption characteristics that make them favorable solar absorbers in photovoltaics, but exhibit suboptimal band edge positions for PEC hydrogen production. Wider band gap absorbers (Eg~1.7 eV) are predicted to be optimal tandem cell partners to these lower-band gap materials, but also exhibit complications in the simultaneous optimization of band gap, band offsets, and other relevant electronic properties in making efficient junctions for tandem-based PEC devices. We have now surveyed a number of alloys, covering the compositional space of $(Cu,Ag)(B,Al,Ga,In)(S,Se)_2$ chalcopyrites to identify materials that exhibit the most promising combination of electronic structure and reliable synthesis. Specifically, this translates to materials with suitable band gaps, band edge positions, stability, and favorable defect properties for realizing the required properties necessary to drive photoelectrochemical hydrogen production.

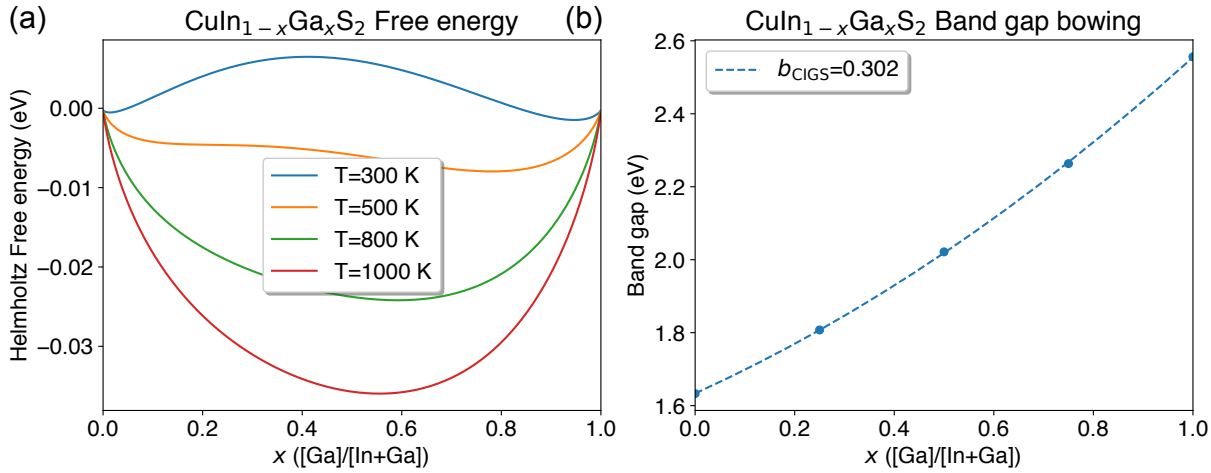

Figure 9. (a) Calculated free energy of mixing for $Cu(In,Ga)S_2$ alloys shown as a function of composition and temperature. (b) The calculated band gaps of solid solution alloys and the associated band gap bowing parameters that quantifies the non-linearity in the band gap with composition. Temperatures in excess of ~250 C are predicted as necessary for synthesizing solid solutions over the entire composition range without spinodal decomposition.

Our calculations are based on density functional theory (DFT) with hybrid functionals that are now well-established methods for evaluating the electronic structure and thermodynamic stability of candidate alloys. Specifically, the calculations utilized the Heyd-Scuseria-Ernzerhof (HSE06) range- separated hybrid functional and projector-augmented wave pseoduopotentials implemented in the VASP code. While more computationally demanding, the hybrid functionals are critical to address deficiencies of conventional DFT in describing the electronic structure of Cu and Ag-based systems like the studied chalcopyrites. For example, conventional DFT methods based on semi-local exchange-correlation functionals tend to exhibit significant errors for the Cu and Ag

materials that often predict metallic states rather than having band gaps in excess of 1 eV as confirmed by experiment. We include the calculated thermodynamic stability and expected band gaps of Cu(In,Ga)S_2 alloys in Figure 9, highlighting how these properties change with composition. These alloys, particularly in the low and intermediated Ga-content, have the desired range of band gaps and exhibit relatively facile synthesis for the desired composition solid solution alloys at modest temperatures. Another example of a different Se-based chalcopyrite alloy with instead alloying of Cu and Ag but yielding similarly favorable top-cell band gaps is included in Figure 10. While these chalcopyrite alloys exhibit similarly favorable band gaps for a range of compositions, they differ notably in their predicted band alignments with composition as we discuss later. This illustrates an important distinction and complication in targeting desired alloys that optimally satisfy several constraints for simultaneously achieving efficient light absorption and charge transport to facilitate PEC.

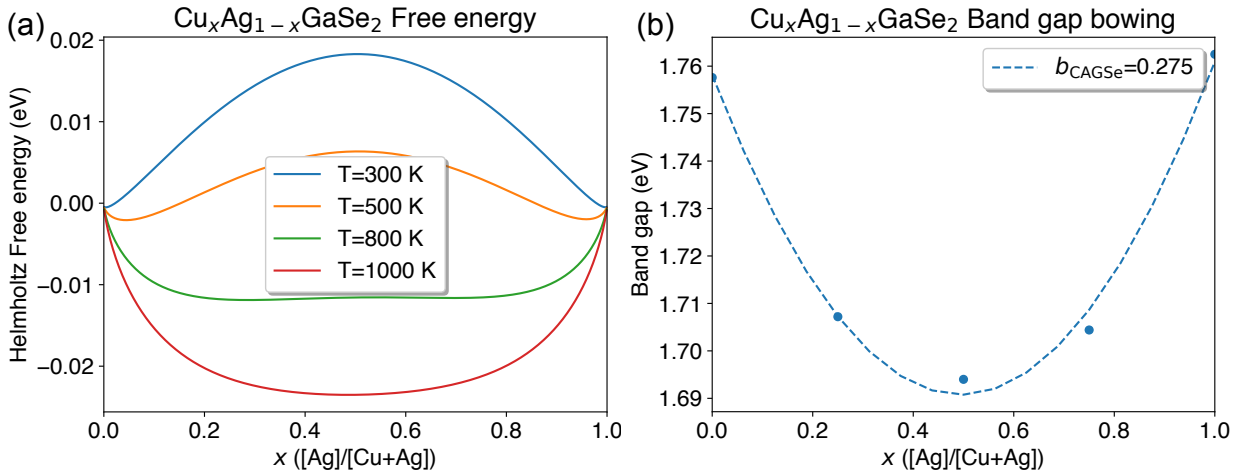

Figure 10 (a) Calculated free energy of mixing for (Cu,Ga)$GaSe_2$ alloys shown as a function of composition and temperature. (b) The calculated band gaps of solid solution alloys and the associated band gap bowing parameters that quantifies the non-linearity in the band gap with composition. Temperatures in excess of ~500 °C are predicted as necessary for synthesizing solid solutions over the entire composition range without spinodal decomposition.

Beyond calculations to identify more favorable alloy compositions, we also spent a considerable amount of time evaluating the potential role of off stoichiometric ordered vacancy compounds (OVCs) materials that can exist in the chalcopyrite family. Specifically, these are defined by lower values of the group I /group III ratios corresponding to Cu or Ag deficiency. These compounds are known to exist in conventional chalcopyrites like Cu(In,Ga)Se_2 and influence charge transport of photo-generated carriers, yet their role in other chalcopyrite alloys has been largely unexplored. An example is included in Figure 11 for Ag-based chalcopyrites, showing that these OVCs are not limited to Cu-based compounds and may form and influence the resulting performance of synthesized material and related alloys integrated into PEC devices.

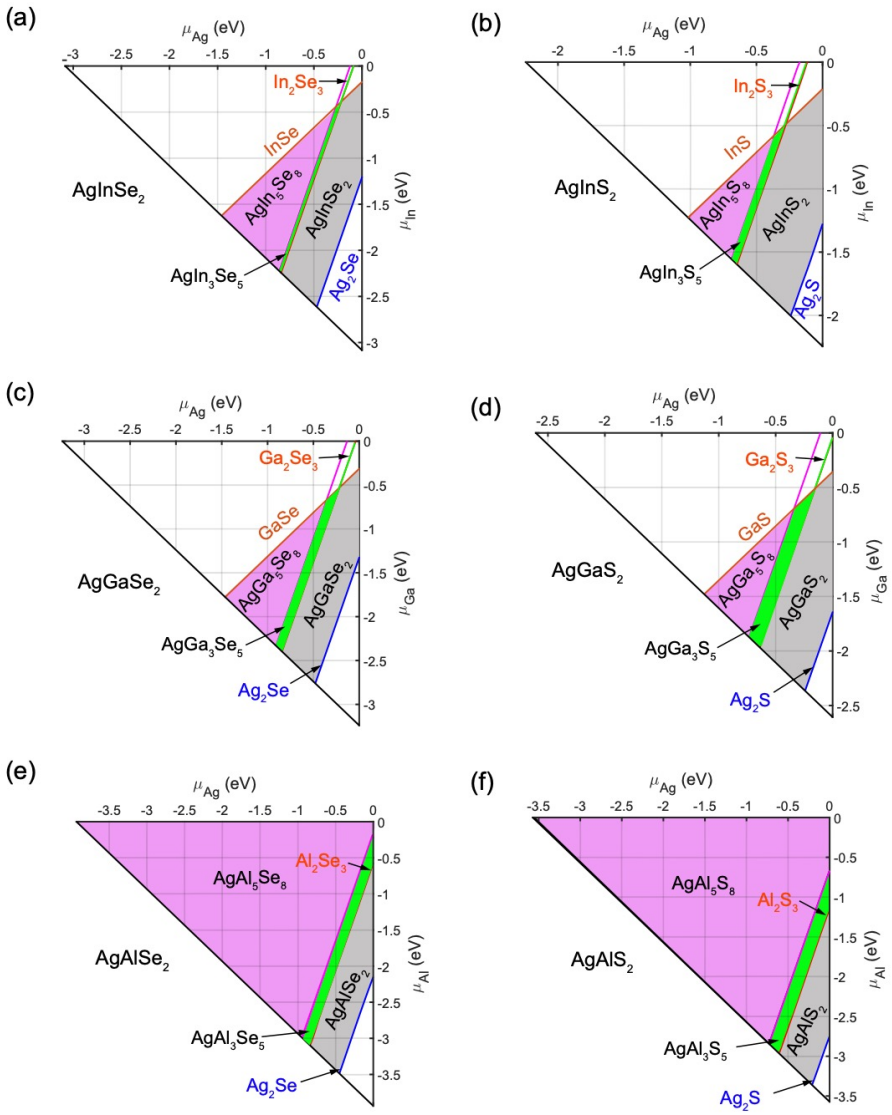

Figure 11. Calculated phase diagrams for Ag-based chalcopyrites, showing the stability regions for OVC-compounds like Ag(III)$(VI)_2$ for III=(In,Ga,Al) and VI =Se and S.

Chalcopyrite band gaps and band alignment with charge transport layers: Another primary goal of the theoretical studies was to evaluate the band alignment properties of candidate absorber materials to facilitate their integration into PEC devices with favorable charge transport. This is because PEC devices require efficient separation and transfer of the photo-generated carriers to the catalytically-active surface, which depends both on the absorber layers and other charge transport layers implemented into the device. These layers include the buffer and the possible formation of OVC or defective layers that may influence the likelihood that photo-excited carriers may participate in the surface reactions. As previously discussed, the composition of the alloy may have a strong influence on the absolute energetic positions of the conduction and valence band, affecting the electron affinity and ionization potential, respectively. Additionally, these parameters may theoretically be independently tuned via alloying on the different sublattices of the chalcopyrites to simultaneously satisfy target absorption and defect properties.

We illustrate the influence of different types of compositional variation in Figure 12 calculated for $Cu(In,Ga)S_2$ and $(Cu,Ag)GaSe_2$ alloys. For the former, larger Ga contents lead to increases in the band gap at the expense of primarily influence the energy position of the conduction band edge, which negatively influences band alignments with buffer layers where conduction band alignments are critical to efficient charge collection from the absorber. This becomes problematic for common buffer layers like CdS that are well aligned to low-band gap $Cu(In,Ga)Se_2$ absorbers, but yield cliff-like conduction band offsets with the larger band gaps materials realized with higher Ga contents. In contrast, we find that the incorporation of Ag can facilitate larger band gaps, but with larger ionization potentials and lower electron affinities. In Figure 12b it can be seen that Ag incorporation leads to only modest changes in the band gap across the full composition range, but can change the electron affinity by ~0.5 eV relative to $CuGaSe_2$, which also exhibits a problematic cliff-like offset with CdS buffers. This illustrates that the compositional flexibility of the chalcopyrite system does permit unique tunability in achieving target band gaps and band edge positions to match to existing buffer layer partners. This additionally provides a strategy to optimizing absorbers in tandem with emerging larger-band alternative buffer candidates like Mg(Zn,O), Zn(O,S) and (Cd,Zn)(O,S) to achieve ideal band alignments for efficient charge collection to drive PEC.

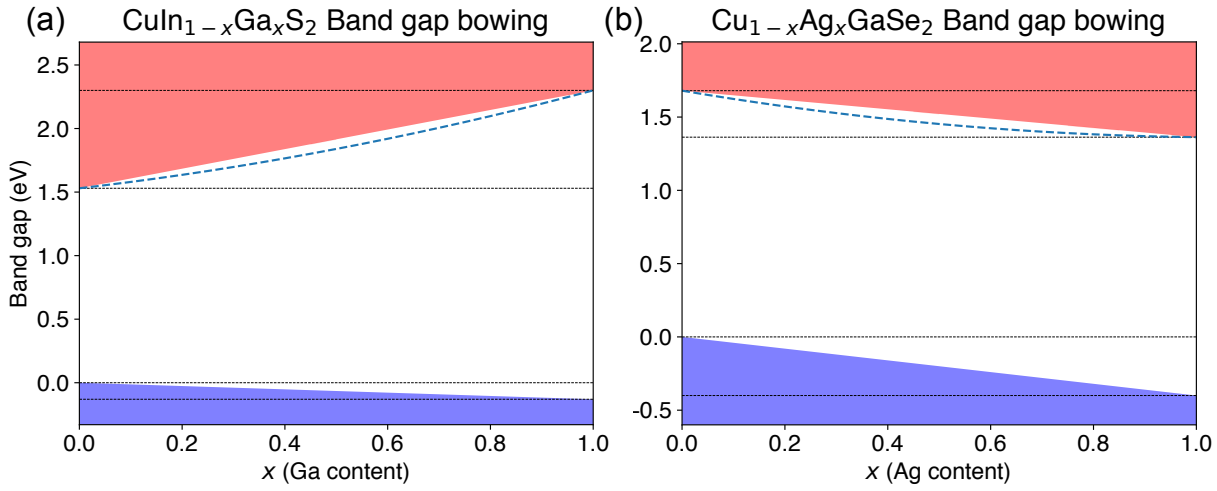

Figure 12. Calculated band gaps and band edge positions for candidate wider-band-gap absorber alloys, shown as a function of composition for (a) $Cu(In,Ga)S_2$ and (b) $(Cu,Ag)GaSe_2$ alloys. The calculated band gap bowing is included as the dashed blue line and assumed to contribute only to the conduction band position for the sake of illustration. While the incorporation of Ga leads to a noticeable increase in the relative position of the conduction band edge (decrease in the electron affinity) with increasing Ga content to realize larger band gaps in $Cu(In,Ga)S_2$, the incorporation of Ag leads to relatively little change in the band gap but a large charge in both the relative conduction and band edge positions of $(Cu,Ag)GaSe_2$.

Beyond the chalcopyrite/buffer interface the possible formation of defective or off-stoichiometry layers such as the OVC compounds can also influence interface energetics. In Figure 13, we illustrate the role of stoichiometry that has been experimentally measured in the Cu-In-Se system and we have verified with independent calculations. These results identify the role that stoichiometry can have in the absorption and band alignment properties that must be considered in conjunction with alloy composition in developing optimal PEC devices. We have additionally extended this analysis to the full family of Cu and Ag-based chalcopyrites to evaluate how the

band gaps and band edge positions are influence by stoichiometry and formation of OVC-type phases. We summarize the band gaps in Figure 14, which exhibits the general trend that decreasing the I/III ratio in the chalcopyrites leads to an increase in the band gap.[14] There are exceptions to this rule that are primarily associated with changes in the underlying electronic structure of the orbital character of the lowest-lying (highest-lying) conduction (valence) bands.

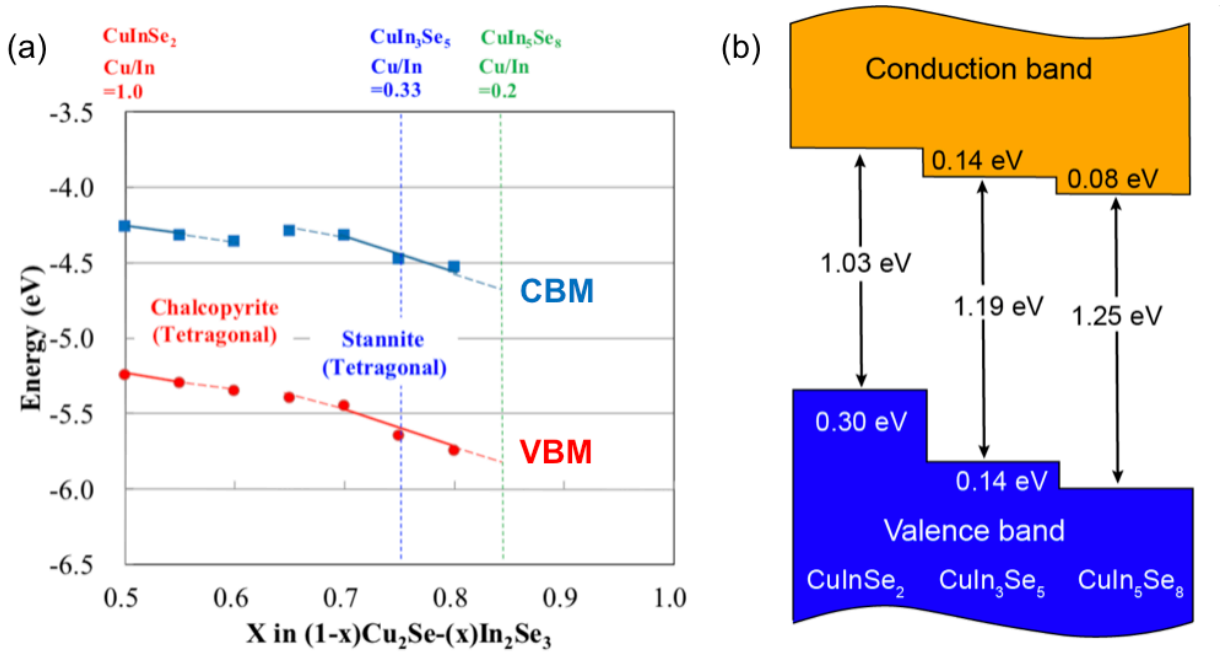

Figure 13. (a) Experimentally measure band edge positions from photoemission spectroscopy in $CuInSe_2$ as a function of the Cu/In stoichiometric ratio. The calculated band edge positions in $CuInSe_2$ and ordered vacancy compounds in the limit of lower Cu/In ratios is include in (b), showing how Cu deficiency introduces larger ionization potentials and electron affinities, that can act as hole barriers to stoichiometric $CuInSe_2$.

We also summarize the calculated band alignments for the Cu-based OVCs in Figure 15. Our results suggest that the OVC phases appear to universally lead to larger ionization potentials and electron affinities, leading to hole-blocking layers relative to the stoichiometric chalcopyrites. However, we find that the conduction band offsets between the chalcopyrites and the OVCs can be large, particularly in the Ga-containing alloys. This suggests that the formation of OVCs can lead to notable cliff-type offsets that may impede electron collection efficiencies; however stoichiometric grading may also facilitate better interfacial alignments with buffer-layers that would ordinarily be expected to perform poorly due to exceedingly large conduction band offsets. This suggest that controlled preparation of OVCs or stoichiometric grading may be a beneficial strategy to engineering improved interfaces in chalcopyrite-based solar and PEC devices.

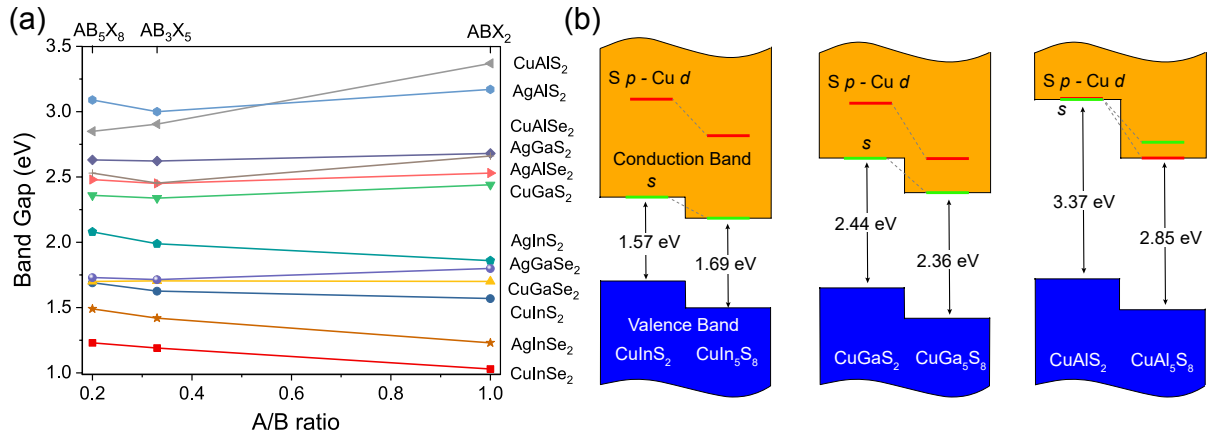

Figure 14. (a) Calculated band gaps for OVC compounds in different ABX_2 chalcopyrite families as a function of the A/B ratio. The bandgaps are generally found to increase with decreasing A/B ratios (e.g. Cu and Ag deficiency), with exceptions owing to differences in the underlying electronic structure. This is illustrated in (b) for $CuAlS_2$, where Cu deficiency leads to changes in the character of the conduction band from heavily *s*-orbital derived states to having more significant *p* and *d*-orbital character that leads to a decrease in the band gap.

Correlation of chalcopyrite absorber defects with synthesis conditions: Significant theoretical efforts were performed to assess the defect thermodynamics in alloys of the $Cu(In,Ga)S_2$ system to supplement the experimental synthesis and characterization efforts. Figure 16, we include a calculated phase diagram and associated defect formation diagram to evaluate the possible role of buffer-layer intermixing at the absorber-buffer interface of fabricated $Cu(In,Ga)S_2$-based PEC devices. We highlight conditions more relevant to experimental synthesis that comprise more Cu-poor and S-rich, vs more Cu-poor and III-rich conditions. Our results identify the incorporation of Cd atoms as both donors on the Cu site (Cd_{Cu}) and acceptors on the group-III sites (Cu_{Ga} and Cu_{In}), can act to shift and pin the Fermi level away from the valence band edge at the absorber-buffer interface. The results are sensitive to compositional fluctuations and are exacerbated for higher Ga-contents, as well as more anion-poor conditions, and highlight a plausible explanation for the saturated open-circuit voltage measured in synthesized $Cu(In,Ga)S_2$ devices compared to base-line $Cu(In,Ga)Se_2$ devices.[8] The high temperature associated with the saturation (200K) and low voltage (636 mV) with respect to the band gap are possibly indicative of interfacial Fermi-level pinning and interface-dominated recombination. We additionally studied several other impurities that could also be incorporated from alternative buffers such as Zn from wider-band gap buffer candidates, and identified similar detrimental effects associated with interfacial intermixing. This suggests the importance of deposition techniques that minimize potential damage and intermixing at the absorber-buffer interface, as well as compositional grading in the vicinity of interfaces or surfaces that can help reduce possible Fermi-level pinning.

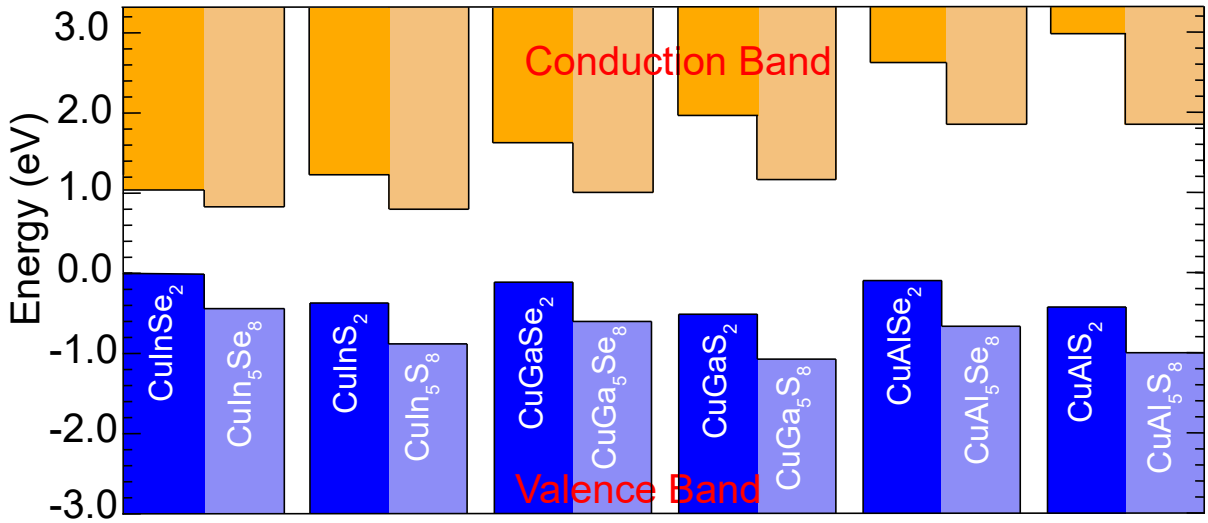

Figure 15. (a) Calculated band gaps for OVC compounds in different ABX_2 chalcopyrite families as a function of the A/B ratio. The bandgaps are generally found to increase with decreasing A/B ratios (e.g. Cu and Ag deficiency), with exceptions owing to differences in the underlying electronic structure. This is illustrated in (b) for $CuAlS_2$, where Cu deficiency leads to changes in the character of the conduction band from heavily *s*-orbital derived states to having more significant *p* and *d*-orbital character that leads to a decrease in the band gap.

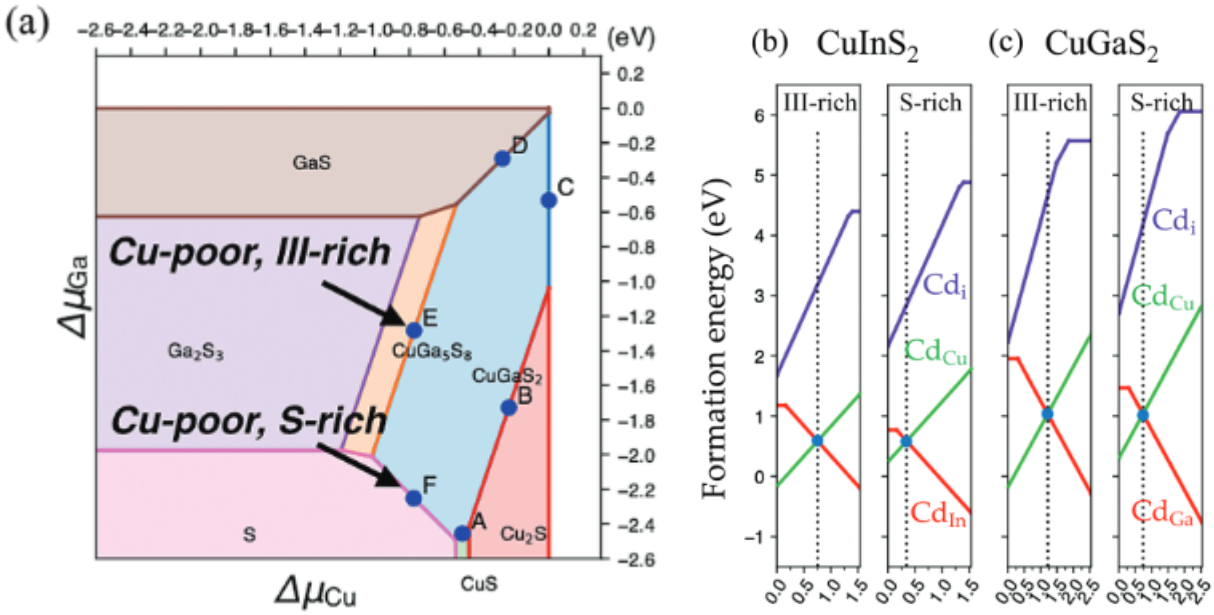

Figure 16. (a) Representative chalcopyrite phase diagram, calculated for $CuGaS_2$ and shown as a function of the Ga and Cu chemical potentials (m). The calculated formation energies of dilute Cd impurities are included for $CuInS_2$ (b) and $CuGaS_2$ (c), shown for conditions representing the regimes of Cu-poor and III-rich/S-poor and S-rich/III-poor limits, as also highlighted in (a). The Fermi level that would result from self-compensation from Cd incorporation is included as the dashed lines in (b and c).

Incorporation of chalcopyrite into HydroGEN DataHub: We additionally developed a web interface for the HydroGEN DataHub that automatically generates a thermodynamic phase diagram of a given chalcopyrite alloy with an associated defect analysis tool. The web app relies on pre-populated data of defect formation energies and compound formation enthalpies that are used to construct the phase diagram boundaries and the dependence of the formation energies on specified chemical conditions. An example plot is shown in Figure 17. The interactive experience allows the user to choose values of chemical potential for the A and B sites (e.g. Cu and In in $CuInSe_2$ or $CuInS_2$), where the phase boundaries reflect chemical equilibrium with other phases. For example, synthesis approaches that identify the incorporation of formation of CuSe-like phases would indicate the conditions are in the vicinity of the phase boundary with CuSe and $CuSe_2$. The influence of these conditions on point defect populations can be readily identified, and how changing various stoichiometric ratios in the synthesis may influence the defect populations and associated electronic properties. In the example of material with Cu_xSe_y precipitates, these interactive diagrams would suggest that changing not just the amount of In, but tuning the overall Cu/In ratio is the most effective way to realizing the best p-type conductivity of the resulting material. This app also allows for the incorporation of user-defined data sets to assess new materials, altered energetics, or new or modified defect energetics that may be chosen by the user. This provides a flexible and informative way of targeting informed synthesis of chalcopyrite alloys.

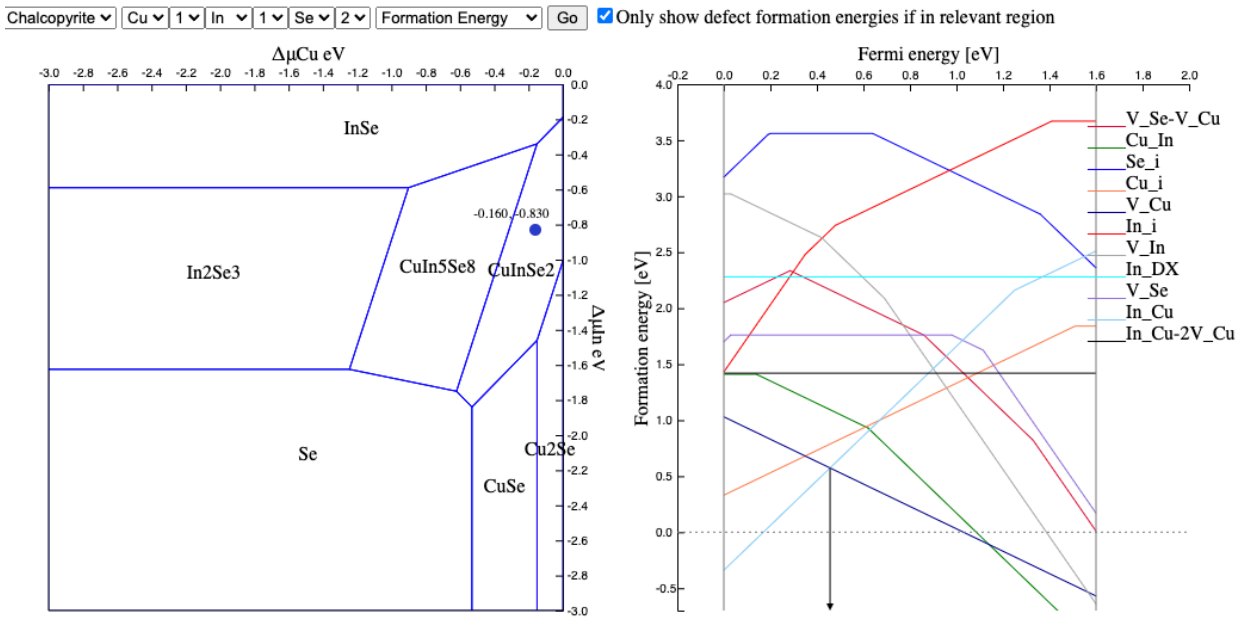

Figure 17. Screenshot of the HydroGEN DataHub web application on interactive defect thermodynamics. The user can scroll over regions within the stability window of the chalcopyrite (left) and the corresponding defect formation energy diagram is generated (right). Not only does the diagram show the dominant defects expected, it also identifies the likely Fermi level position based on the expected defect populations. This provides intuitive guidance for choosing conditions where desired Fermi levels can be targeted, or suppression of unwanted defect populations.

b. Solution-processed chalcopyrite absorbers

The purpose of this work was to develop low-cost solution-based techniques to fabricate novel chalcopyrite materials. Particular focus was to develop promising chalcopyrite materials for photovoltaic and PEC water splitting applications that are difficult to synthesize using conventional co-evaporation technique such as $Cu(In,Al)Se_2$ and $Cu(In,B)Se_2$. We choose ink-based process to synthesize the materials due to its versatility to fabricate multi-elements compound materials, such as the chalcopyrite. Through a careful ink formulation, we are able to deposit films with desired stoichiometry. The ink can be deposited into a substrate by a wide range of techniques (spin coating, dip coating, inkjet printing, spray coating) to form a precursor film which later on can be converted into a high crystalline film by high-temperature annealing. We started the work with synthesizing $CuIn(S,Se)_2$ film, a well-known material in the chalcopyrite family, through molecular-ink method. This material acted as baseline for incorporation of other elements (aluminum and boron). Then, we attempted to synthesize $Cu(In,Al)Se_2$ and $Cu(In,B)Se_2$ using the similar method. Details of the synthesis methods and results of the works are explained below.

Synthesis of $CuIn(S,Se)_2$ film from molecular-ink solutions: We started our efforts by fabricating phase pure $CuIn(S,Se)_2$ (CISSe) thin films by molecular ink technique. We synthesized molecular ink as a precursor made by mixing of 0.26 M CuCl and 0.33 M $InCl_3$ as metals source, 1.77 M thiourea as chalcogen source, into methanol as solvent (Figure 18a). Apart from the addition of $InCl_3$ which was done in N_2-filled glove box (O_2<0.1 ppm, moisture<0.6 ppm), all other chemicals were added in air. We targeted ink with a Cu-poor metal ratio (Cu/In= 0.8) which has been reported to result in a high-efficiency CIGS device, and to avoid the need of a toxic KCN-etching to remove Cu_xSe_y which would form at the absorber's surface with Cu-rich composition. This ink, in principle, can be applied with multiple deposition methods such as spin coating, spray coating, dip coating, and inkjet printing. In this project, we used spin coating method to deposit the ink to the substrate. The spin coated film was then selenized at 550 ^oC for 10 min. to convert the low-crystalline as-deposited $CuInS_2$ precursor film into a high-crystalline CISSe. Figure 18b presents a SEM image of the CISSe film 1.5 μm thick made of large grains. The PV device was completed with chemical bath deposition of 70-80 nm CdS film and sputtering of 200 nm-ZnO/100-nm ITO bilayer. The CISSe device had a maximum efficiency of 8.3% with J_{SC}, V_{OC}, and FF of 34.5 mA/cm^2, 424 mV, and 56.0%, respectively. The absorber has a band gap of 1.03 eV estimated from EQE spectrum of the device (Figure 18c).

Synthesis of aluminum-containing CISSe films: We then used the above CISSe as a baseline to explore the possibility of synthesizing novel chalcopyrite materials. Our first attempt was to synthesize Al-containing CISSe (Al-CISSe). The Al-containing films were made following the same recipe as the baseline CISSe except with addition of $AlNO_3$ as the Al source. The metallic ratios of the Al-containing ink were Cu/(In+Al)=0.8, Al/(Al+In)=0.1, and thiourea/(Cu+In+Al)=3.0. Instead of alloying directly with CISSe, our study showed that Al formed amorphous nanosized-Al_2O_3 covering parts of the film top and bottom surfaces as well as embedded into the bulk. Interestingly, we observed an efficiency enhancement of CISSe solar cells via this in-situ incorporation of Al_2O_3. Defect passivation via in-situ formed Al_2O_3 is thought to play a major role in the improvement of the solar cell performance through decreased interface and bulk recombination.

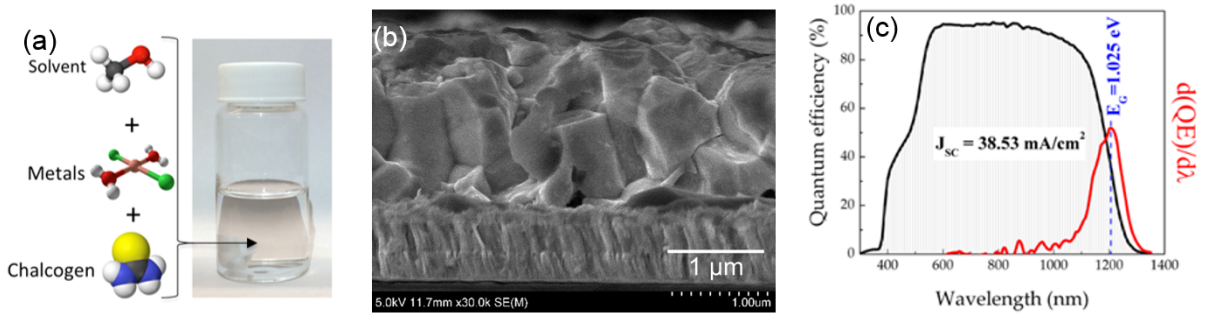

Figure 18. (a) Picture of typical molecular-ink solution used in this work which consists of methanol as solvent, CuCl and $InCl_3$ as metal sources, and thiourea as chalcogen source. (b) Cross-sectional SEM image of CISSe film synthesized by selenization of the spin-coated molecular-ink. (c) EQE spectrum of one of CISSe PV device showing an estimated band gap of 1.025 eV with an integrated J_{SC} of 38.53 mA/cm^2

Figure 19 shows TEM images of the Al-CISSe sample. The image in Figure 19a reveals several bright spots dispersed throughout the film, suggesting the presence of different compounds other than CISSe. These bright spots are particularly obvious at the bottom area of the CISSe film where smaller grains formed. These segregated compounds were found to be as big as ~200 nm across, as evident in Figure 19b. A point EDX analysis performed in the bright region in Figure 19b revealed an Al/O atomic ratio of 0.65, a value very close to stoichiometric Al_2O_3 (Al/O: 0.67). An electron diffraction pattern performed on the same bright spot shows a halo ring feature, revealing the lack of long-range ordering. In contrast, well-defined diffraction spots were observed on the CISSe grain next to the bright spot (dark region in Figure 19b). Therefore, we conclude that the Al-CISSe films fabricated with our molecular ink process are made of highly crystalline CISSe with isolated amorphous Al_2O_3 grains dispersed throughout. Higher magnification images reveal the presence of nanometer sized amorphous Al_2O_3 (~3-15 nm) covering parts of the absorber top surface (Figure 19c) as well as at the grain boundaries (Figure 19d). The detection of both aluminum and oxygen throughout the bulk by AES (Figure 19e) implies that nano-scale amorphous Al_2O_3 is present over the entirety of the Al-CISSe film, although only few remarkable spots are observed in the TEM micrographs.

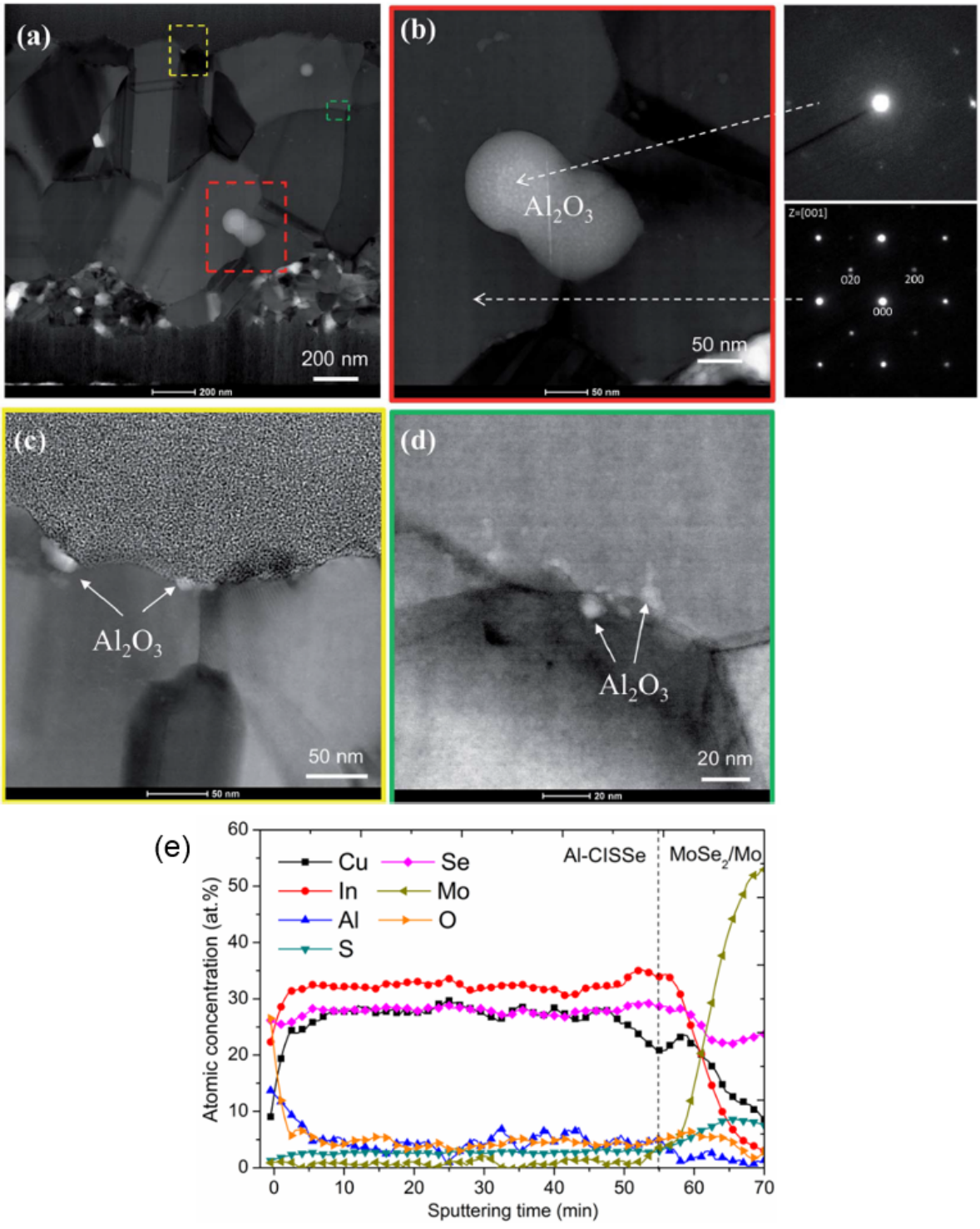

Figure 19. Bright-field TEM images taken from multiple areas on the Al-CISSe film: (a) entire cross-section of film, (b) grain interior, (c) near-surface and (d) grain boundaries within film. Insets at Fig. 4b show electron diffraction patterns from the bright spot and surrounding material. The bright spot has an Al/O atomic ratio of 0.65, which is very close to the ratio of stoichiometric Al_2O_3 (Al/O: 0.67). (e) AES depth profiling of Al-CISSe film.

Photovoltaic devices were then fabricated by chemical bath deposition of a CdS layer onto the absorbers, followed by sputtering of a ZnO/ITO bilayer. Figure 20a shows the statistical distribution of photovoltaic performances from the Al-CISSe solar cells fabricated from multiple batches. Photovoltaic performance of CISSe solar cells fabricated through similar methods are also shown for comparison. Overall, power conversion efficiency (PCE) of Al-CISSe devices are consistently higher than that of CISSe. Al-CISSe devices had PCE ranging from 9.1% to a maximum efficiency of 11.6% (champion Al-CISSe cell: J_{SC} = 35.8 mA cm^{-2}, V_{OC} = 518 mV, FF = 62.2%, no anti reflective coating) with an average PCE of 10.1%, whereas CISSe devices showed PCE from 5.5% to a maximum of 8.3% (champion CISSe cell: J_{SC} = 34.5 mA cm^{-2}, V_{OC} = 424 mV, FF = 56.0%) and an average PCE of 6.4%. Figure 20b shows the photocurrent density-voltage curves from the champion Al-CISSe and CISSe devices. The average J_{SC} of Al-CISSe devices (34.5 mA cm^{-2}) was found to be slightly higher compared to that of the CISSe devices (32.8 mA cm^{-2}), as seen from the increased EQE in almost entire wavelength range (Figure 20c). The electronic (as measured by EQE) and optical (as measured by diffuse reflectance, data not shown) bandgaps of Al-CISSe (E_{EQE} = 1.01 eV, $E_{reflec.}$= 1.01 eV) and CISSe (E_{EQE} = 1.03 eV, $E_{reflec.}$= 1.01 eV) where found to be nearly identical, confirming that Al does not alloy with CISSe to form Cu(In,Al)Se_2 in our experiment.

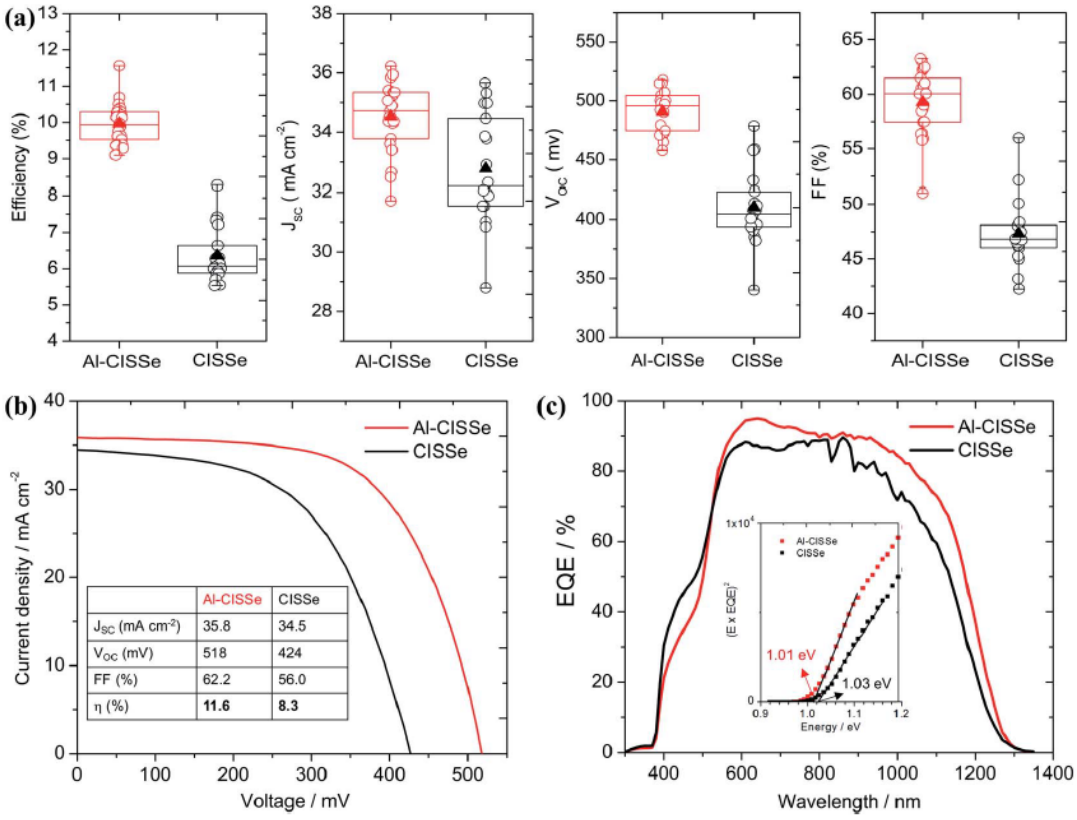

Figure 20. (a) Statistical box charts illustrating distribution of photovoltaic properties of Al-CISSe (total number of devices: 22) and CISSe (total number of devices: 18) solar cells. Filled triangles indicate average values. (b) Current density-voltage curves measured on Al-CISSe and CISSe champion cells. (c) EQE spectra of Al-CISSe and CISSe champion cells (inset shows estimation of band gaps). The J_{SC} integrated from EQE are 36.4 mA cm-2 and 34.0 mA cm-2 for Al-CISSe and CISSe cells, respectively.

We performed capacitance-voltage (C-V) measurement to CISSe solar cells with and without Al_2O_3 incorporation to evaluate their defect density. Figure 21a shows the apparent doping density (N_{CV}) vs. depletion width extracted from the C-V measurement. It is can be observed that the devices with Al_2O_3-incorporation have lower N_{CV} compared to without Al_2O_3. At 0 V, the average N_{CV} of Al_2O_3-incorporated devices was estimated to be 3.14 x 10^{15} cm^{-3}, while that of devices without Al_2O_3 had an average N_{CV} of 7.40 x 10^{15} cm-3. Since bulk and interface defects are responsive to C-V measurement, the lower N_{CV} of Al_2O_3-incorporated devices implies a reduced overall defect density of CISSe with the presence of Al_2O_3. Apart from the reduced defect density, the space charge region (SCR) is wider in Al_2O_3-incorporated devices (average SCR = 0.48 μm) than that in devices without Al_2O_3 (average SCR = 0.34 μm). We also performed V_{OC}-T measurement to understand the recombination mechanism (Figure 21b). As presented in the figure, a difference of 70 mV in activation energy was observed between Al_2O_3-incorporated (E_A = 1.06 eV) and without Al_2O_3 (E_A = 0.99 eV), indicating that interface recombination is more severe in the latter devices. Using the results obtained from both V_{OC}-T and C-V measurements, we conclude our in-situ Al_2O_3 incorporation process reduces defect density in the absorber (as evidenced by a widening of SCR) as well as at the junction with CdS (as demonstrated by an increase in E_A).

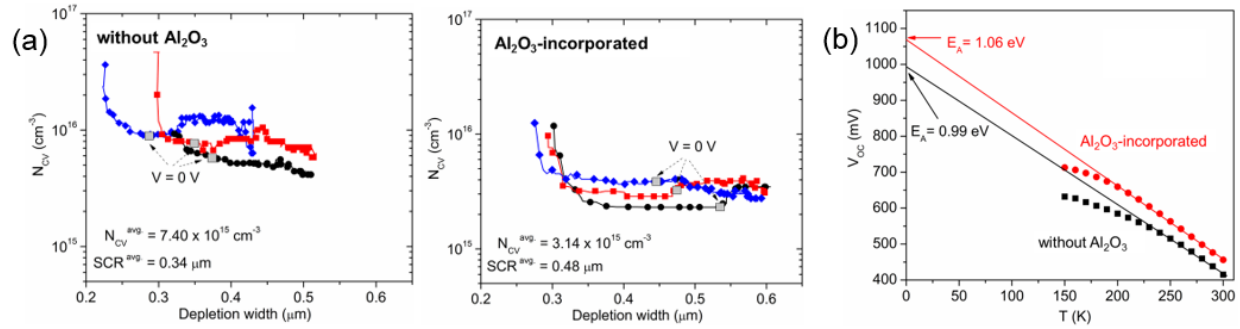

Figure 21. (a) Comparison of depth profiles of apparent doping density (N_{CV}) deduced from C-V measurements of three without Al_2O_3 and three Al_2O_3-incorporated CISSe solar cells. Gray filled squares indicate V = 0 V. (b) Temperature-dependent VOC measurements performed on the devices.

Synthesis of boron-containing CISSe films: We also explored boron (B)-incorporation to CISSe through the similar molecular ink method. Boric acid (H_3BO_3) was used as B-source. The B-containing CISSe film and solar cells were fabricated identical as CISSe and Al-CISSe films and devices above. We synthesized B-containing samples from molecular ink with various B/(B+In) ratios which were 0, 0.1, 0.3, and 0.5, labeled as CISSe, B(0.1)-CISSe, B(0.3)-CISSe, and B(0.5)-CISSe, respectively. Figure 22a shows XRD spectrum at (112) orientation of B-CISSe films with various boron concentration. In general, all films have identical position of (112)-orientation which suggest no boron-alloying into CISSe on all films. XPS analysis to the films suggest that boron element is detected from the films. However, further analysis is undergoing to characterize the nature of boron inside the film which highly likely exist as its oxides not bonding to the CISSe. Figure 22b shows photocurrent-density curves of photovoltaic devices fabricated from the films. Solar cell using B(0.1)-CISSe has higher efficiency than that without boron (CISSe) with maximum efficiency of 9.2% (J_{SC} = 33.6 mA cm^{-2}, V_{OC} = 456 mV, FF = 60.1%). The improvement comes from a slightly higher V_{OC} and FF. The efficiency has significantly dropped with higher boron concentration and the solar cell using B(0.5)-CISSe was shorted (~0% efficiency).

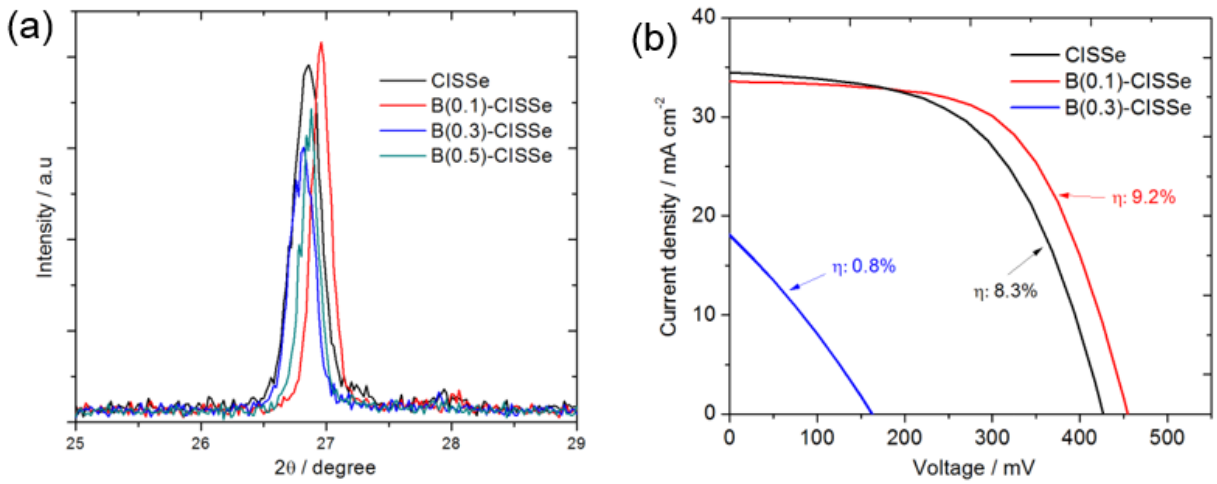

Figure 22. (a) XRD spectrum at (112) peak of boron-containing CISSe films with various B/(B+In) ratios. (b) Current-density and voltage curves of boron-containing CISSe solar cells.

Figure 23 shows surface SEM images of the boron-containing CISSe films. CISSe and B(0.1)-CISSe films appear to have identical grain structures with large grains throughout the film. However, B(0.1)-CISSe film appear to be made of denser and more interconnected grains, while CISSe film has distinct grain boundaries. This denser and flatter surface could be one of the reasons for the higher efficiency. Relatively large isolated grains (>3 μm-across) are detected on B(0.3)-CISSe and B(0.5)-CISSe films, which appear to enlarge with higher boron content. In addition, voids near the big grains are clearly seen on B(0.5)-CISSe film. This would suggest that the boron-content could correlate with the extent of the grain growth of the film. While inks with B/(B+In)= 0.1 appear to be optimal for the grain growth of the present film as it produced dense-interconnected grains, while higher B/(B+In) would result in voids. These voids and isolated large grains could explain the relatively poor efficiencies of the solar cells. Despite the absence of any boron-alloying to CISSe, nevertheless, our finding suggest that Boric acid could act as grain growth agent for CISSe synthesized by molecular ink-approach. Balance between film thickness and amount of Boric acid in the ink is necessary to obtain void-free films made of large grains.

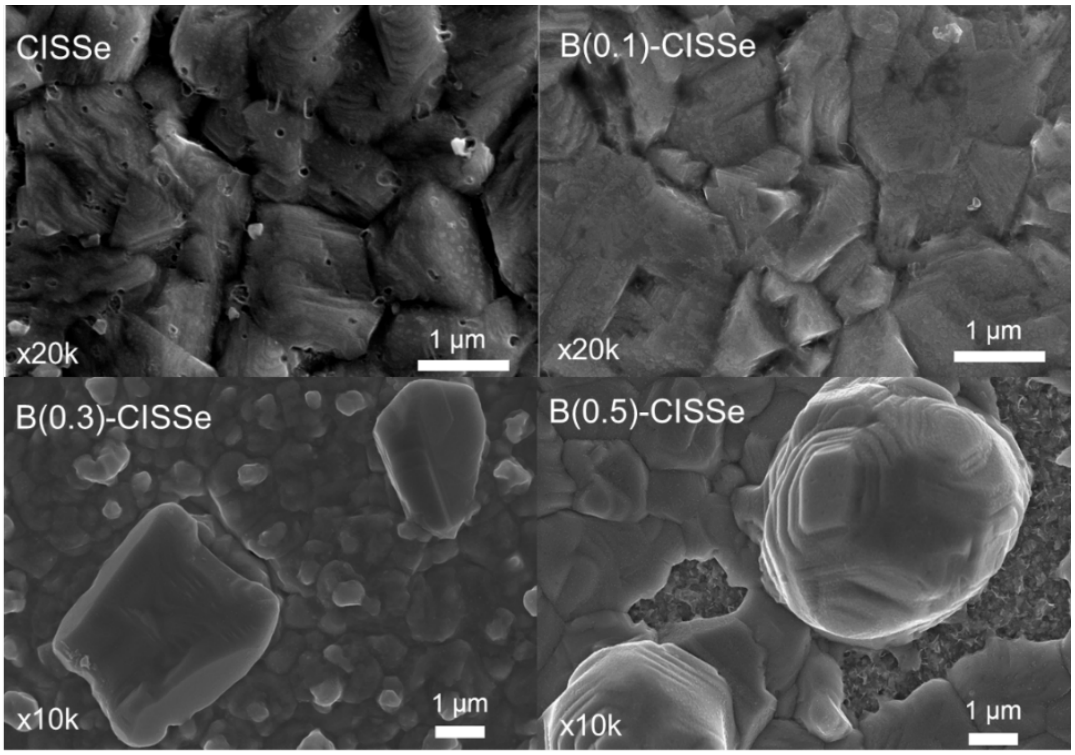

Figure 23. SEM images of Boron-containing CISSe films with various B/(B+In) ratios.

Summary: The original goal of this study was to develop low-cost solution-based technique to fabricate novel chalcopyrite materials. We developed solution-based techniques to fabricate high-crystalline and phase-pure $CuIn(S,Se)_2$ films prepared from selenization of spin-coated molecular ink containing CuCl, $InCl_3$, and thiourea dissolved in methanol. Then, this material was used as a baseline material to incorporate aluminum or boron into the CISSe with original aims to fabricate aluminum or boron-alloyed CISSe for wide-gap chalcopyrite materials. Either $AlNO_3$ or H_3BO_3 were added into the molecular ink to synthesized those materials.

We found out that our synthesis method did not result on Al-alloying or B-alloying to CISSe which could be due to easier formation of Al or B oxides compounds during the synthesis process in air. However, on the other hand, we observed higher efficiency of solar cells from both Al-containing CISSe and B-containing CISSe compared to the CISSe baseline. We report for the first time on an in-situ incorporation of Al_2O_3 in solution-processed CISSe thin film.[9] The solar cell fabricated from Al_2O_3-incorporated film had a maximum efficiency of 11.6%, a value significantly higher than that of solar cells made from the ink without the addition of Al (efficiency: 8.3%). The improvements stemmed primarily from increased V_{OC} as well as FF. Defect passivation via in-situ formed Al_2O_3 is thought to play a major role in the improvement of the solar cell performance. Solar cell using boron-containing CISSe film had a maximum efficiency of 9.2%. The improvement was thought to come from denser grain structures compared to the CISSe baseline. We expect that this Al_2O_3 in-situ passivation approach and grain-growth assistance via addition of H_3BO_3 method can be extended to other chalcogenide materials synthesized by the molecular-ink approach.

c. Ordered vacancy Compounds absorbers co-evaporation

Absorber 3-stage growth: For narrow band gap Cu(In,Ga)Se_2 photovoltaic absorbers, a 3-stage co-evaporation process is known to achieve superior power conversion efficiencies, although the mechanism is still debated. The process starts with In-Ga-Se deposition, followed by Cu-Se and ends with In-Ga-Se. This process was adapted to $CuGa_3Se_5$ absorbers by excluding In and extending the 3rd stage to reach the more Cu-poor $CuGa_3Se_5$ compositions. In all our previous $CuGa_3Se_5$ results, 1-stage growth was used (constant rate co-evaporation of Cu, Ga and Se). In this project, PEC performance was measured for 1-stage and 3-stage $CuGa_3Se_5$ absorbers, which have wide band gaps (~1.8 eV). The left of Figure 24 shows that the 3-stage process improved both the PEC turn-on voltage and saturated photocurrent density. The absorbers had similar compositions and band gaps, and IPCE indicated better collection of high energy photons (300 – 470 nm) in the 3-stage absorber (not shown). Next, the effect of absorber thickness was examined for the 3-stage process. The right of Figure 24 shows that increasing the absorber thickness from 1 to 2.5 μm increased the saturated photocurrent density from 6 to 10 mA/cm^2, while the turn-on voltage decreased slightly. IPCE showed most of the photocurrent enhancement was at longer wavelengths, which require a thicker film to be absorbed. Similar results were observed for 1-stage recipes and different substrate glasses. The optical absorption path is likely improved, while the series resistance is increased with thicker absorbers. Thus, switching from 1-stage to 3-stage growth and from 1 to 2.5 μm thick absorbers both improved the baseline PEC performance.

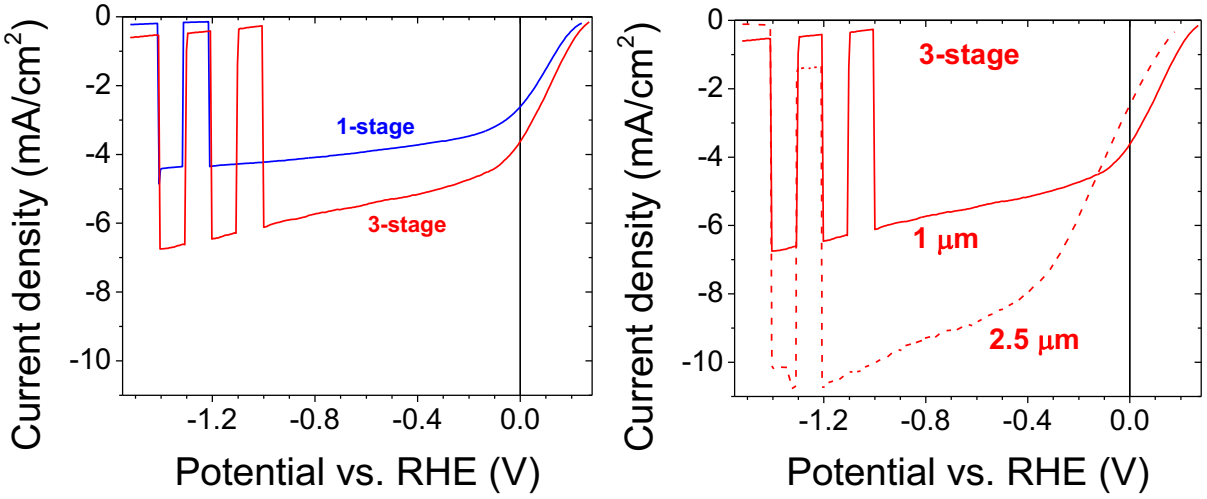

Figure 24. PEC chopped-light current-voltage characteristics of (left) 1-stage (blue solid line) and 3-stage (red solid line) $CuGa_3Se_5$ photocathodes, and (right) 3-stage $CuGa_3Se_5$ photocathodes with 1 μm (red solid line) and 2.5 μm (red dashed line) thick absorbers grown on aluminosilicate glass/Mo substrates.

Si doping: For chalcopyrite-based absorbers, CdS is the best passivating buffer layer. However, the small band gap of CdS (2.4 eV) leads to parasitic absorption, and its electron affinity is too large in magnitude, leading to a 'cliff' band alignment with $CuGa_3Se_5$. To address this, an alternative surface passivation strategy was explored. A very recent report used Si doping of $Cu_{0.8}In_{0.7}Ga_{0.3}Se_2$ photovoltaic absorbers to achieve excellent performance without a CdS buffer.[15] Those results suggested that Si was passivating at grain boundaries and the absorber surface. To test this for $CuGa_3Se_5$ we co-evaporated Si during the final stage of growth. On venting the

chamber to air, we discovered that $SiSe_2$ reacts with H_2O to form SiO_2 and toxic H_2Se gas, which was detected by the continuously monitoring hydride gas system directly above the system. As a result, we developed an extremely cautious venting procedure that has kept H_2Se levels below the detection limit (50 ppb).

Soda-lime glass/Mo/$CuGa_3Se_5$ photocathodes doped with 3.2 and 6.2 nm Si were characterized, and CLIV are in Figure 25. Si doping improved the onset potential monotonically from 0.3 to 0.36 V, and the photocurrent density at 0 V vs. RHE increased from -6.3 to -8 mA/cm^2. The improved PEC properties suggest that Si passivates the $CuGa_3Se_5$ surface, similar to the effect of Si on $Cu_{0.8}In_{0.7}Ga_{0.3}Se_2$ for photovoltaics.

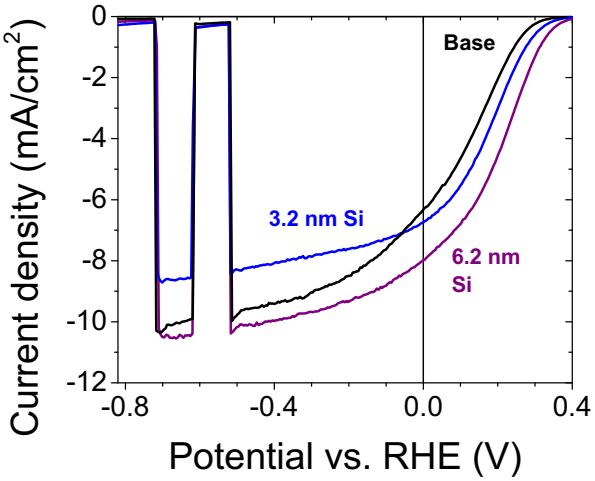

Figure 25. CLIV characteristics of standard photocathodes (glass/Mo/$CuGa_3Se_5$): the best baseline (black), 3.2 nm Si (blue) and 6.2 nm Si (purple).

In situ Zn surface treatment: We previously found that a Cd partial electrolyte (PE) treatment improved the PEC CLIV characteristics of bare $CuGa_3Se_5$ photocathodes and boosted performance in solid-state solar cells that used sputtered $Zn_{1-x}Mg_xO$ buffers.[11] To expand on that success, the prospect of introducing a group IIB surface treatment in situ was studied. It was hypothesized that performing the surface passivation before air exposure should lead to better control of the process and final surface microstructure. Cd evaporation was prohibited due to safety concerns, so Zn evaporation was used instead. Zn (6 – 22 nm) was evaporated near the end of $CuGa_3Se_5$ growth. Adding Zn during $CuGa_3Se_5$ co-evaporation or while the substrate was still at 600 °C was detrimental to performance. Instead, the best results were obtained by allowing the substrate to cool to 340 – 400 °C and evaporating 16 – 22 nm of Zn (Figure 26). The solar cells with CdS buffers had substantially better open-circuit voltages, short-circuit current densities and efficiencies than the baseline. The Zn surface also allowed a thinner CdS buffer to be used, increasing current at constant fill factor to reach 4.2% efficiency. For comparison, the previous best efficiency for these absorbers was 3.0%. The in situ Zn surface treatment likely passivates the $CuGa_3Se_5$ surface. Unfortunately, the improvement did not translate to the 3-electrode CLIV measurements, which used bare photocathodes in 0.5 M H_2SO_4 electrolyte (Figure 27). If ZnSe formed at the surface, then it should rapidly etch in the acidic electrolyte. Combining the Zn surface treatment with a 2nd buffer and/or protective layers may help translate the observed PV passivation to PEC water splitting.

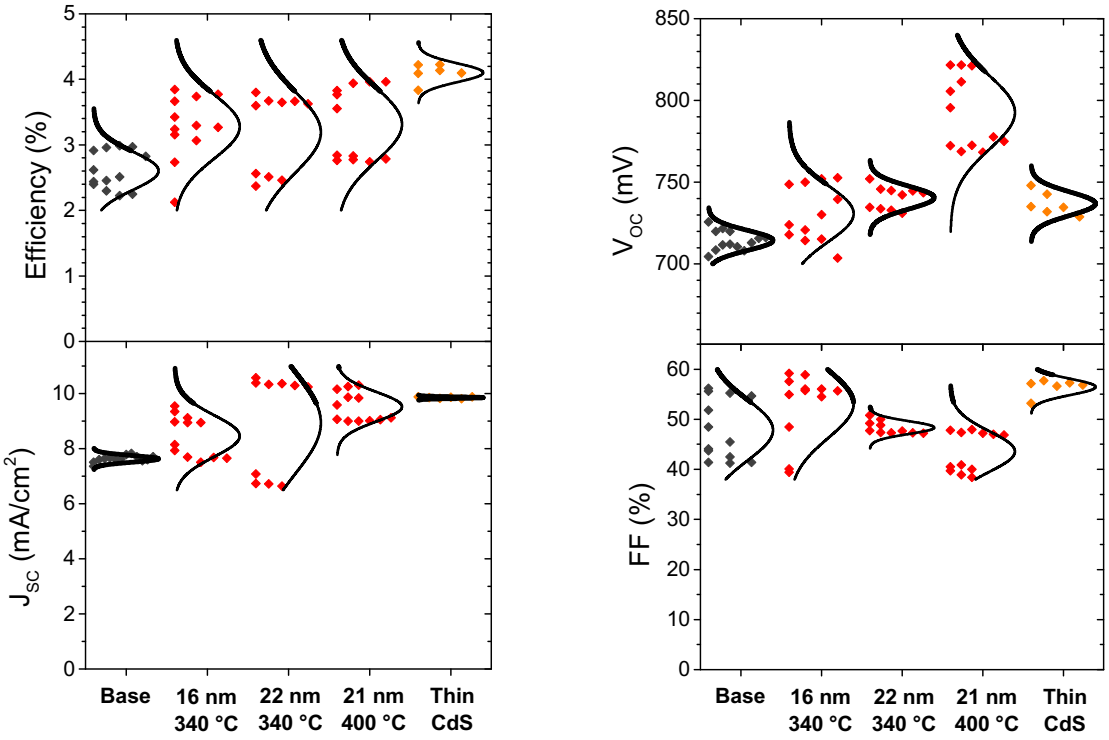

Figure 26. Efficiency, open-circuit voltage (V_{OC}), short-circuit current density (J_{SC}) and fill factor (FF) of solid-state Mo/$CuGa_3Se_5$/CdS/i-ZnO/Al:ZnO/grid solar cells with various amounts of Zn evaporated onto their surfaces in situ at different temperatures during cool-down after absorber growth. The "16 nm 340 °C" sample was repeated with thin CdS, showing the Zn surface acts as a buffer.

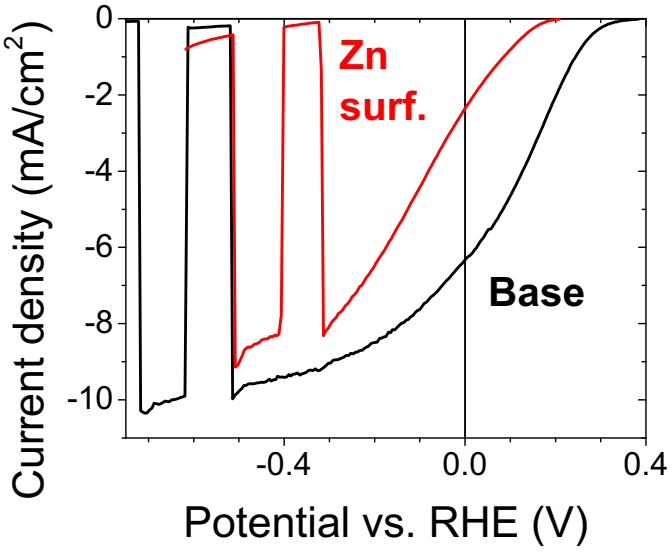

Figure 27. CLIV showing that the in situ Zn surface (red; "16 nm 340 °C" sample from Figure 26) degraded performance relative to the baseline (black) Mo/$CuGa_3Se_5$ photocathode.

Cd partial electrolyte treatment + In_2S_3 buffer: Improving the $CuGa_3Se_5$ onset voltage to more anodic values would enable a tandem device for unassisted water splitting. To accomplish that we applied a catalyst layer to our best surface treatment and buffer combinations. We used a standard photocathode HER catalyst: PtRu sputtered for 3 s, which leads to discontinuous, 2 – 5 nm particles covering roughly 30% of the surface. Our best surface treatments were previously discussed: an in situ Zn surface treatment to $CuGa_3Se_5$ led to mean efficiency of 4.1% in solid state solar cells that employed CdS buffers, compared to a baseline mean efficiency of 2.6%. Since CdS dissolves in the sulfuric acid electrolyte for PEC, we added a second buffer of spin-coated In_2S_3 for 3-electrode CLIV measurements (blue line in Figure 28). We also tested a Cd partial electrolyte treatment (Cd PE) on the $CuGa_3Se_5$ surface (green line in Figure 28) and combined a Cd PE with the In_2S_3 buffer (red line in Figure 28). While the Cd PE $CuGa_3Se_5/In_2S_3$/PtRu photocathode had a photocurrent onset approaching +0.5 V vs. RHE, the $CuGa_3Se_5$/PtRu baseline exhibited the best current-voltage characteristics in terms of power production. In conclusion, the PtRu catalyst improved the performance of $CuGa_3Se_5$, and optimization of the Cd PE treatment and In_2S_3 buffers may lead to further improvements in the future.

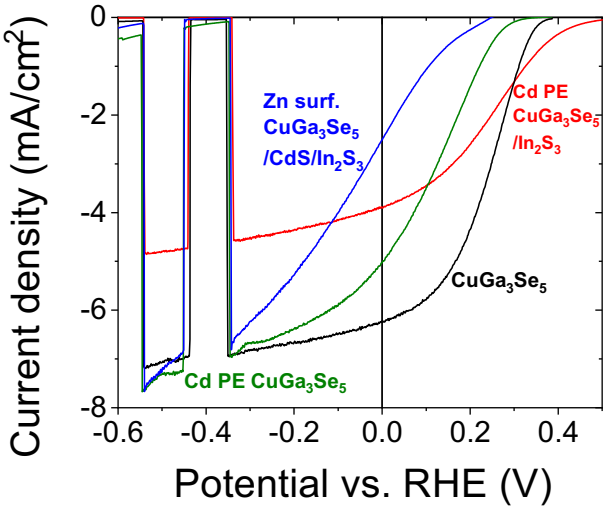

Figure 28. CLIV of a baseline glass/Mo/$CuGa_3Se_5$/PtRu photocathode (black), Cd PE-treated $CuGa_3Se_5$/PtRu (green), Cd PE-treated $CuGa_3Se_5/In_2S_3$/PtRu (red), and in situ Zn surface-treated $CuGa_3Se_5$/CdS/In_2S_3/PtRu (blue) samples using 3-electrode measurements with mercury sulfate reference electrode, Pt counter electrode, and 1 sun illumination in 0.5 M sulfuric acid electrolyte.

Evaluation of Ga_2O_3 buffer: Finally, we explored the use of Ga_2O_3 as a protective layer for $CuGa_3Se_5$ photocathodes. Our previous work showed that $CuGa_3Se_5$ exhibits the best PEC HER durability of any polycrystalline photocathode.[6] X-ray photoelectron spectroscopy characterization of $CuGa_3Se_5$ films indicated that a thin native oxide of predominantly Ga_2O_3 forms on the surface of our $CuGa_3Se_5$ films.[16] Interestingly, Ga_2O_3 is resistant to etching in sulfuric acid and has been used as a photoanode for water splitting in sulfuric acid. To understand what role Ga_2O_3 may play in $CuGa_3Se_5$'s superior durability, we intentionally drove the formation of the native oxide by annealing films in air for 3 min at 100 °C and 200 °C. The best chopped-light current-voltage (CLIV) characteristics for each sample type are in Figure 29. The air oxidation improved photocurrent density and onset potential, possibly by acting as a passivating layer or catalyst.

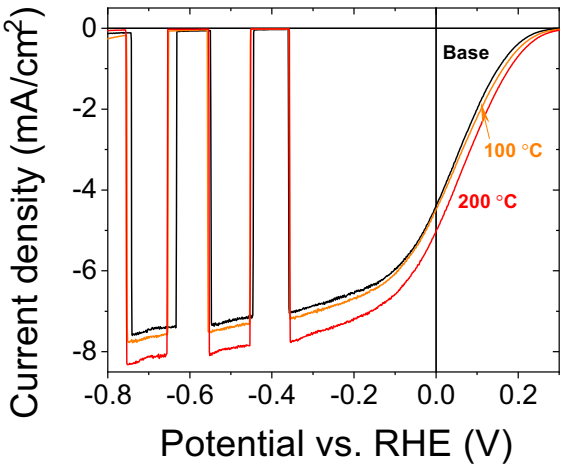

Figure 29. CLIV of a baseline glass/Mo/$CuGa_3Se_5$ photocathode (black), and that sample oxidized in air for 3 min at 100 °C (orange) and 200 °C (red). 3-electrode measurements were performed with mercury sulfate reference electrode, IrO_x counter electrode, and 1 sun illumination in 0.5 M sulfuric acid electrolyte.

Next, we sputtered 20 nm of Ga_2O_3 onto $CuGa_3Se_5$ at 160 °C. We then fabricated solar cells to test whether Ga_2O_3 passivates defects. The $CuGa_3Se_5$ with the thick native oxide had similar photovoltaic (PV) efficiency to the baseline (Figure 30a), but when the CdS buffer was removed, efficiency decreased. The sputtered Ga_2O_3 maintained photovoltage, albeit at low current density (Figure 30b). These results indicate that the native Ga_2O_3 does not passivate $CuGa_3Se_5$ well but conducts current, whereas the sputtered Ga_2O_3 may passivate while blocking current.

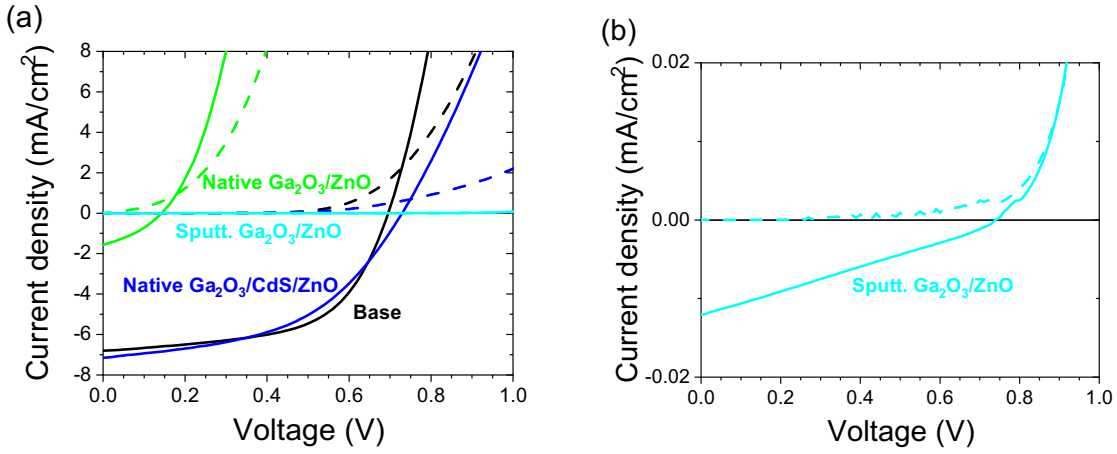

Figure 30. (a) Current density-voltage of a baseline glass/Mo/$CuGa_3Se_5$/CdS/ZnO solar cell (black), and that sample oxidized in air for 3 min at 200 °C with CdS (blue) and without CdS (green), as well as 20 nm of Ga_2O_3 sputtered onto $CuGa_3Se_5$ at 160 °C without CdS (cyan). Dashed lines are dark and solid lines are illuminated with 1 sun. (b) The sputtered Ga_2O_3 data rescaled to reveal the photovoltage at very low current density.

We then measured the CLIV characteristics of those same glass/Mo/$CuGa_3Se_5$/Ga_2O_3 samples after depositing a standard photocathode HER catalyst (PtRu sputtered for 3 s, which leads to discontinuous, 2 – 5 nm particles covering roughly 30% of the surface). In agreement with the solar cell data, both the sputtered Ga_2O_3 samples had diminished onset potential (Figure 31). However, the sample with native Ga_2O_3 had improved photocurrent density, relative to the

$CuGa_3Se_5$/PtRu baseline. Although we did not perform durability measurements, Ga_2O_3's resistance to sulfuric acid may also improve durability by protecting $CuGa_3Se_5$. In summary, native Ga_2O_3 may already play a role in $CuGa_3Se_5$'s superior durability, and better control over Ga_2O_3 buffers may be a route to further enhance PEC performance/durability.

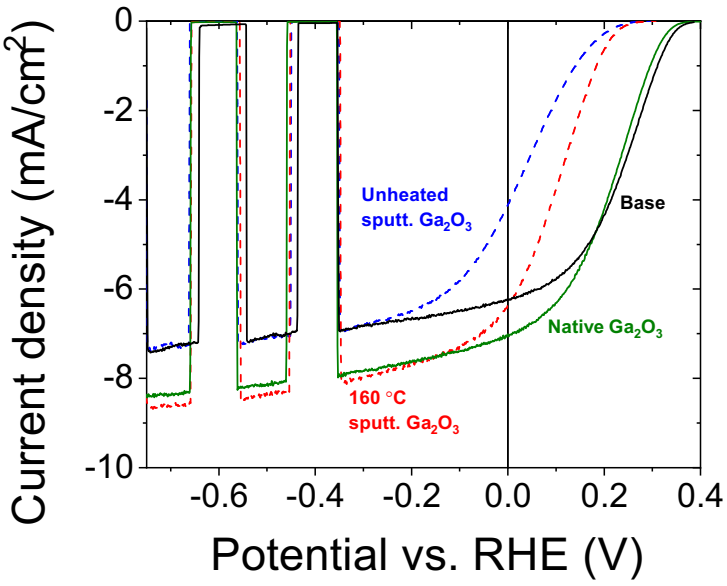

Figure 31. CLIV of a baseline glass/Mo/$CuGa_3Se_5$/PtRu photocathode (black solid) and that same photocathode structure, except with 20 nm Ga_2O_3 sputtered onto unheated $CuGa_3Se_5$ (blue dashed), with 20 nm Ga_2O_3 sputtered onto $CuGa_3Se_5$ at 160 °C (red dashed), and with native Ga_2O_3 formed at the surface of $CuGa_3Se_5$ by annealing in air at 200 °C for 3 min (green solid). 3-electrode measurements were performed with mercury sulfate reference electrode, IrO_x counter electrode, and 1 sun illumination in 0.5 M sulfuric acid electrolyte.

Summary: In conclusion, we found that the 3-stage co-evaporation process improves the properties of wide band gap $CuGa_3Se_5$ photocathodes for PEC water splitting, relative to a 1-stage process. Increasing $CuGa_3Se_5$ thickness from 1 μm to 2.5 μm reached photocurrent densities of 10 mA/cm^2. Si doping further improved the onset voltage and photocurrent density in the CLIV of $CuGa_3Se_5$ photocathodes, probably through passivation. We also found that while an in situ Zn surface treatment of $CuGa_3Se_5$ enabled more efficient solar cells than ever before, this did not translate to PEC due to the instability of ZnSe in sulfuric acid. Instead, we coupled a Cd partial electrolyte treatment with an In_2S_3 buffer to passivate $CuGa_3Se_5$ for PEC. Finally, our results indicate that native Ga_2O_3 may have played a role in the superior durability of $CuGa_3Se_5$ photocathodes, where intentionally introducing a Ga_2O_3 buffer should help realize further gains.

d. Optical characterization of wide bandgap Cu(In,Ga)(Se,S)$_2$

Wide bandgap Cu(In,Ga)(S,Se)$_2$ chalcopyrite's are a promising material system for tandem photovoltaic, direct water splitting and hybrid photo-electrode devices. A major challenge however are hampered device performances due to the considerably low voltage achieved in general by devices with a bandgap above 1.4 eV. Possible origins for these losses are non-radiative recombination due to deep defects, tailing defects states close to the band edges, and unfavorable band alignments with the buffer and charge transport layers. Within this project we investigated all three possibilities and found that all three possibilities lead to major losses in achievable open

circuit voltage. This leads to the conclusion that alternative buffer layers like (Mg,Zn)O or Zn(O,S) and advance processing routes, suppressing deep defect formation and bandgap fluctuations, need further development.

Investigation of Urbach tailing in Cu(In,Ga)S_2: The density of sub bandgap states, leading to Urbach tailing, are directly linked to an increase in radiative and non-radiative recombination as is nicely shown by Wolter et al. for various materials systems ranging from Si to CdTe, CIGS and perovskites.[17] In general values below 20 meV for the Urbach energy are targeted. It can be determined by using absolute calibrated photoluminescence measurements (PL) or by measuring the absorption coefficients by photo thermal deflection (PDS), which yields a much higher sensitivity for sub-bandgap absorption compared to UV-VIS or quantum efficiency measurements. A Cu(In,Ga)S_2 absorber on FTO cover glass prepared by the HNEI group was studied by PDS, as shown in Figure 32.

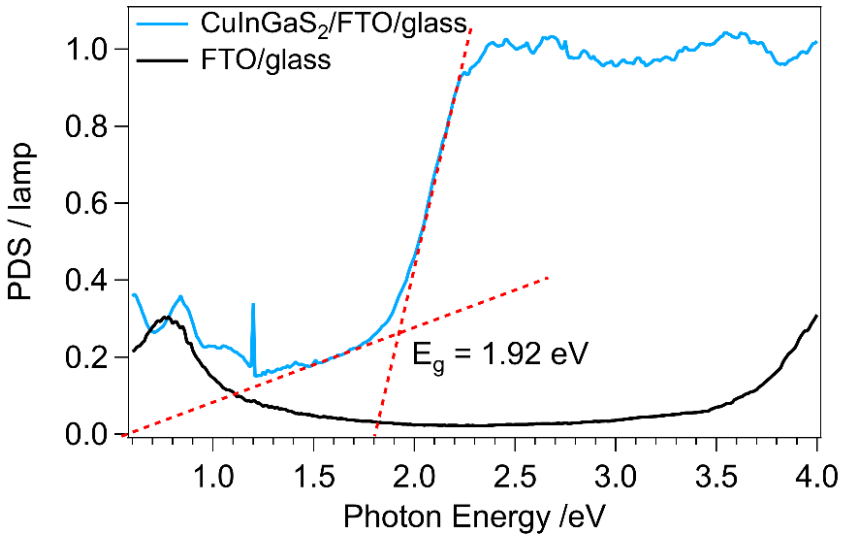

Figure 32: Photothermal deflection spectrum of $CuInGaS_2$ on FTO glass substrate (blue) and FTO/glass (black). Red lines indicate the approximate position of the absorption edge and the background from defect absorption and/or thin film interference.

From the data, a bandgap of 1.92 eV and an Urbach energy of 56 meV is determined. The Urbach energy is very large compared to high efficiency photovoltaic devices with less than 20 meV and possibly originates from a high density of near band edge defect states or from a distribution of band gaps caused by compositional fluctuation. The latter are stemming from inhomogeneities in the In/Ga and S/Se alloying. In both cases an optimized absorber quality could yield improvements here.

Quasi Fermi level splitting of Cu(In,Ga)S_2 absorber layers: The quasi Fermi level splitting (qFLs) is an upper limit for the open circuit voltage of a finished device and can be determined from absolute calibrated PL measurements, which were carried out on the previously studied Cu(In,Ga)S_2 sample. The PL response showed a very broad peak at 1.5 eV at room temperature, as shown in Figure 33a), and thus considerably below the bandgap value close to 1.95 eV. This luminescence possibly originated from defect states and/or from regions which were not fully

sulfurized, thus having a lower Eg, and act as recombination centers. Since the room temperature PL did not originate from the expected band-band transition, an evaluation of the qFLs using Planck's generalized law commonly used in the community is not possible.

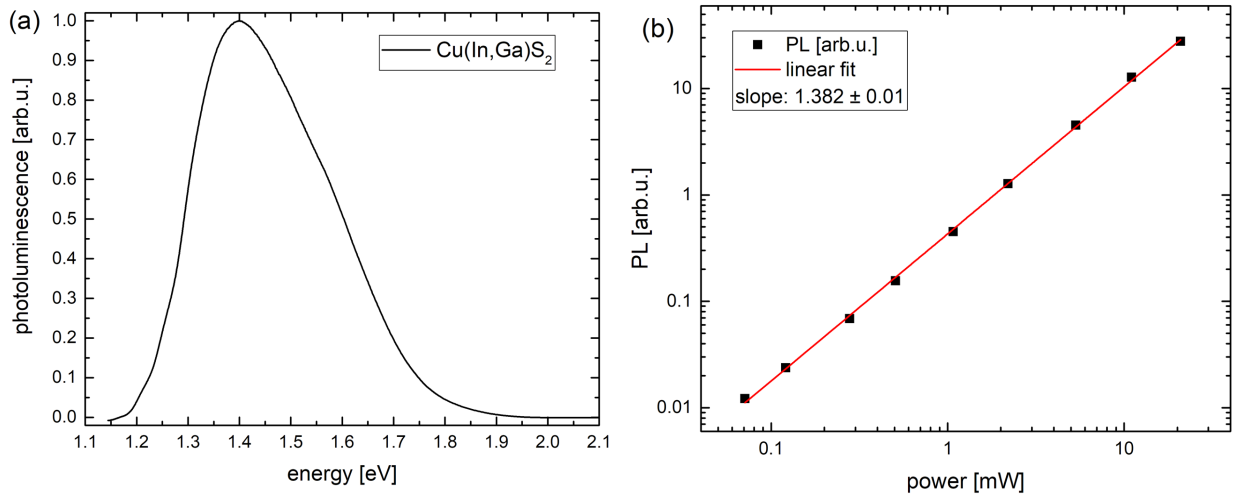

Figure 33: (a) Photoluminescence spectrum of a Cu(In,Ga)S_2 absorber layer measured at room temperature under 405 nm excitation. (b) Log-log plot of the integrated PL intensity measured over 2.5 decades of excitation. The slope of the linear fit gives the optical diode factor.

As a work around the external radiative efficiency (ERE) relative to a known standard was determined. From the ERE of about 1.2E-4 % a $qFLs_{loss,}$ being the difference between the maximal qFLs reachable within the Shockley-Queisser limit and the measured qFLs, of 340 meV was calculated. Using the maximal reachable $qFLs_{SQ}$ (1.672 eV) and the $qFLs_{loss}$ (340 meV) a qFLs at high excitation (~ 100 suns) of 1.332 eV is calculated. To correct for the high excitation density used during the determination of the ERE the "optical diode factor" (see next paragraph) was utilized to reach a final qFLs of (1.17 ± 0.05) eV and a $qFLs_{loss}$ of approximately 500 meV at room temperature using 1 equivalent sun.

The loss value of 500 meV is higher than what has been shown in literature for high efficiency cells (300 - 420 meV), but it is a decent value. The found qFLs valueof 1.17 eV is much higher than the open circuit voltage of 0.590 eV measured on finished devices, using a CdS buffer layer.[8] This massive difference corroborates the suspicion of an unfavorable band alignment and possibly interface recombination at the CdS/Cu(In,Ga)S_2 interface. A further indication for this bad interface is the difference between the optical diode factor of 1.38 measured on the bare absorber as shown in Figure 33b), compared to the electrical diode factor measured on full devices which is above 2. The increase in diode factor after device fabrication has been linked to recombination close to the buffer/absorber interface in low bandgap Cu(In,Ga)Se_2 solar cells.[18] Equation linking the $qFLs_{loss}$ to the external radiative efficiency:

$$qFLs_{loss} = qFLs_{SQ} - qFLs = k_bT \ln(ERE) \quad (1)$$

Summarized, the determined qFLs value shows a high absorber quality, giving a relatively high upside for the open circuit voltage. However, the poor band edge alignment between the absorber and the buffer layer leads to a large voltage drop and limits the device performance.

Defect spectroscopy via low temperature PL on Cu-poor $CuGaSe_2$ and $CuGa_3Se_5$: One root cause of low qFLs can be deep defects acting as non-radiative recombination centers. A common way to investigate chalcopyrite's for defects are PL measurements at low temperatures (10 K) as well as temperature dependent measurements. In this kind of analysis in general Cu-poor and Cu-rich compositions give two distinct kinds of spectra. While Cu-rich composition exhibit multiple narrow peaks corresponding to various optical transitions involving defects and excitons, Cu-poor composition normally show broad asymmetric peaks well below the bandgap.

Looking at Cu-poor compositions first, we studied a $CuGaSe_2$ fabricated at HNEI and a $CuGa_3Se_5$ sample fabricated at NREL. Temperature dependent photoluminescence under low excitation conditions were performed and are shown in Figure 34. Both samples show broad peaks likely originating from quasi-DA transitions. In Cu-poor composition a high degree of compensating defects states lead to local varying charge carrier densities which get screened by distorting the band edges. The sustained red shift observed from 15-150 K as well as a strong blue shift when measuring with varying excitation density at 15K (≈ 30 meV/dec) corroborate the assumptions of strong compensation effects in the materials.

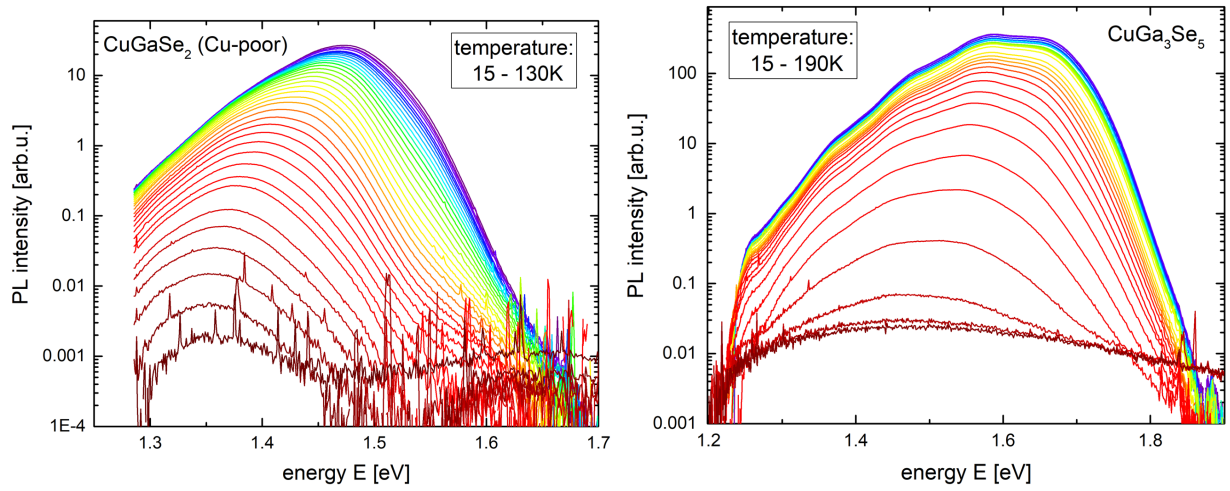

Figure 34: Temperature dependent photoluminescence spectrum of a Cu-poor $CuGaSe_2$ (left) and a $CuGa_3Se_5$ sample (right) measured with low excitation density.

The observed PL quenches with increasing temperature and the deep defect transition vanishes for both samples around 150 K. For the $CuGaSe_2$ sample the band-band transition around 1.68 eV appears for higher temperatures, whereas only noise is detected at room temperature for the $CuGa_3Se_5$ sample. The latter indicates a very high degree of non-radiative recombination taking place at room temperature, drastically reducing the open circuit voltage. To extract the activation energies of the defects involved in the optical transition the PL data is integrated and plotted over the inverse temperature in Figure 35. The spectra of the $CuGa_3Se_5$ sample are superimposed by thin film interference effects (visible as wiggles in the signal mainly at energies below 1.6 eV) and the determined activation energies should thus be treated cautiously. Fitting a quenching model to the data a shallow defect around 15 meV is found in both samples. Likely related to the well-known shallow D1 donor (≈10 meV) related to the copper interstitial or the indium on copper anti-site. For the $CuGaSe_2$ sample the second activation of 120 meV is close to what is expected for the copper vacancy forming a shallow acceptor type defect (≈ 100 meV). The $CuGa_3Se_5$ sample

quenches stronger with increasing temperature, resulting in a higher defect activation energy of about 240 meV. We preliminary do not assignment this transition to a point defect. On a side note, it should be stated that the activation energy especially of deep defects (> 100 meV) is prone to be underestimated when using high excitation densities and that the activation energies could be higher. The 120 meV defect in $CuGaSe_2$ should not majorly impact the possible open circuit voltage. However, a defect which is more than 240 meV deep, will act as recombination center even in case of the large bandgap of 1.85 eV in $CuGa_3Se_5$.

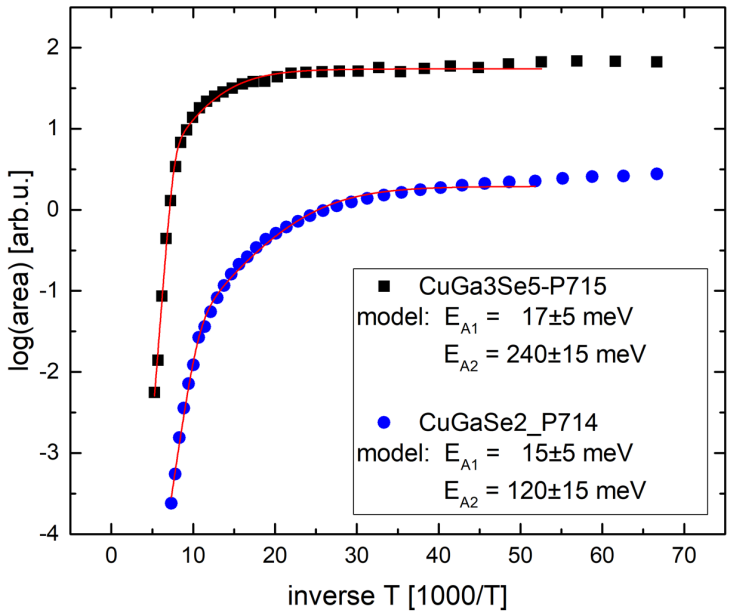

Figure 35: Integrated PL intensity of the two selected samples plotted over the inverse temperature and fitted with a quenching model.

Defect spectroscopy via low temperature PL on Cu-Rich $CuGa(S,Se)_2$: In general defect spectroscopy via low temperature PL is done on Cu-rich samples, which don't exhibit potential fluctuations and thus allow to directly observe various optical transitions. While there is some literature about the $CuGaSe_2$ ternary, publications about the $CuGaS_2$ ternary and the influence of sulfur alloying are sparse. Within the project we performed low temperature PL measurements on a batch of four $CuGa(Se,S)_2$ samples grown Cu-rich on FTO covered glass in a low temperature process with varying sulfur content (S/(S+Se) ~ 0 / 0.15 / >0.95). All samples in this series have been tested for water splitting before PL characterization.

The PL spectra of the pure selenide sample between 40 K and 170 K are shown in Figure 36. Just above the bandgap a luminescence peak originating from an excitonic transition is detected. Around 1.64 eV, the well-known DA2 transition is observed, involving the acceptor type Cu on Ga antisite defect typical for Cu-rich grown $CuGaSe_2$. Between 1.3 eV and 1.5 eV a broad luminescence feature dominating the spectrum is detected, which does not match up with any of the commonly observed intrinsic defect transitions. To learn more about the transition an excitation dependent measurement series is caried out spanning two orders of magnitude. The normalized data is shown on the right in Figure 36. With increasing excitation intensity the 1.45 eV peak develops a shoulder on the high energy side, leading to a substantial broadening and red shift. Such

behavior could indicate the saturation of a defect within a DA transition leading to shift from a DA-transition to a free-bound transition. It could be speculated that the shallow defect involved in the transition is the Cu on Ga antisite (~ 120 meV), which is an acceptor. This would imply a new donor type defect below the conduction bad edge with an activation energy between 100 and 250 meV, depending on the strength of the phonon coupling and the Huang Rhys factor. At room temperature (not shown) the band-band transition dominates the spectrum while the deep defect transition is still visible around 1.35 eV. The fact that it is still visible at room temperature implies that it slightly reduces the achievable open circuit voltage. Since the sample was tested for water splitting before it cannot be excluded that the observed defect luminescence originates from extrinsic defects and we thus do no try to assign it to a point defect.

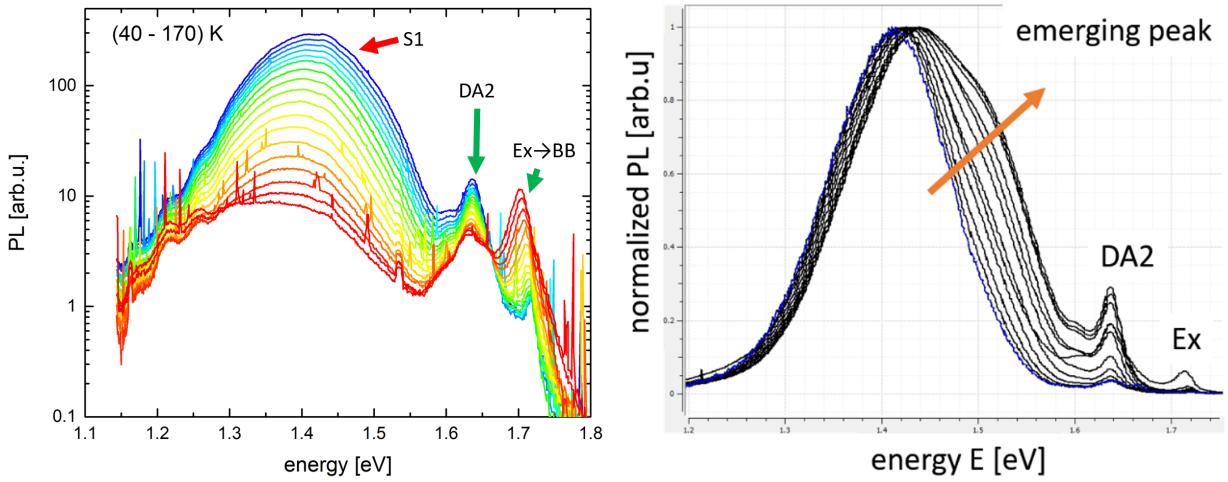

Figure 36: Left: Photoluminescence spectrum of a $CuGaSe_2$ sample glass measured between 40 and 170 K. Right: Normalized spectra of the same sample measured with various excitation intensities at 13.5 K.

The temperature dependent PL series a fully sulfurized sample from 15 K to 300 K in Figure 37 exhibits the known excitonic transition and a DA transition can be seen as a shoulder at 2.3 eV. Besides that, two broad peaks centered around 1.5 eV and 2.0 eV are observed. It could be speculated that the optical transition at 1.5 eV has the same origin as the one observed in the pure selenide sample. The signal around 2.0 eV quenches rather fast with temperature hinting a low activation energy of an involved defect state. At room temperature the intensity of the deep defect transition at 1.5 eV is more than an order of magnitude larger than the band to band transition, thus strongly limiting the devices performance.

Comparing samples with different sulfur content, as shown on the right side of Figure 37, it could be speculated that S1 is present in all samples and does not shift with sulfur content. S_2 is only observed in sulfur containing samples and it follows the band edges. Further studies on absorber layers not tested for water splitting and with a wider selection of S/Se-ratios would be needed to try linking the defect states to intrinsic defects and to give guidance on how to avoid or mitigate them.

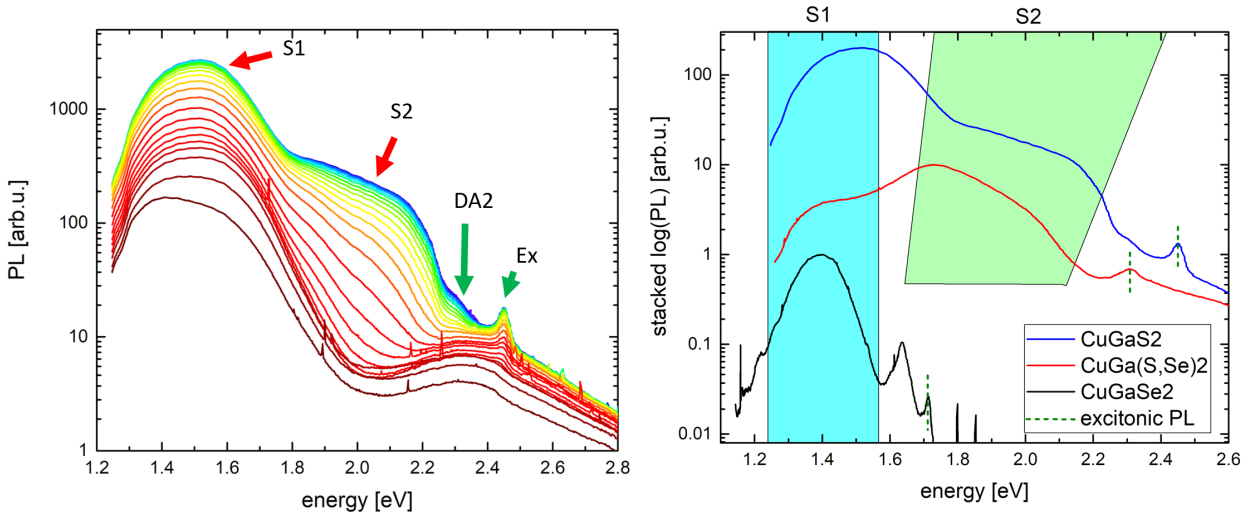

Figure 37: Left: Temperature dependent photoluminescence measured between 13.5 K and 296 K of a of $CuGaS_2$ absorber. Right: Comparison between different of $CuGa(Se,S)_2$ samples with varying sulfur content.

Summary: Within this project various $Cu(In,Ga)(S,Se)_2$ samples with Cu-rich and Cu-poor composition have been investigated. Although quasi-Fermi level splitting values indicate a high upside for the device performance, only low open circuit voltage values are reach likely due to an unfavorable band alignment between absorber and CdS buffer layer. Compositional fluctuations and the possibility of external defects hamper the qualitative evaluation of the defect spectroscopy measurements executed. However, the fact that deep defect transitions are strongly visible even at room temperature means that they limit the device performance. For future enhancements in device efficiency it will be important to investigate alternative buffer materials and to suppress bandgap fluctuations as well as deep defect formation.

4. Achievements in Task 2 "Interface Engineering for Enhanced Efficiency and Durability"

a. Surface and interface characterization by photoelectron spectroscopy

This task was performed to investigate the chemical and electronic structure of chalcopyrite thin films for photoelectrochemical (PEC) water splitting. To complete this task, experimental techniques at UNLV and at Beamline 8.0.1 of the Advanced Light Source (ALS), Lawrence Berkeley National Laboratory, were utilized to derive a description of surfaces and interfaces in chalcopyrite-based PEC systems. At UNLV, XPS (x-ray photoelectron spectroscopy) and UPS (ultraviolet photoelectron spectroscopy) were used to provide the chemical structure at the *surface*. At the ALS, XES (x-ray emission spectroscopy) was utilized to provide the chemical structure at the *surface-near bulk*. To gain insights into the electronic properties of the materials, UPS and IPES (inverse photoemission spectroscopy) were used to determine the valence band maximum (VBM) and conduction band maximum (CBM), respectively, together providing the electronic surface band gap. This combination of techniques provides a comprehensive description of the chalcopyrite materials under study.

Chemical characterization of solution-processed $CuInSe_2$ absorber and $CuInS_2$ precursor surfaces : As an initial study to gain insights into solution-processed sample surfaces and the impact of a selenization treatment (see section for details III.b), UNLV used XPS and XES to characterize a sample set consisting of a $CuInSe_2$ "selenized" and a $CuInS_2$ "as-deposited" sample. Inks were formulated in air. The $CuInS_2$ "as-deposited" sample was spin-coated in air onto a molybdenum-coated soda lime-glass substrate, using a solution based on CuCl, $InCl_3$, and thiourea in methanol. The "$CuInSe_2$ selenized" sample was further annealed in a selenium atmosphere. The "$CuInS_2$ as-deposited" sample thus serves as a 'precursor' to the "$CuInSe_2$ selenized" sample.

Figure 38 shows the XPS survey of the "$CuInSe_2$ selenized" and "$CuInS_2$ as-deposited" samples. As expected, copper, indium, oxygen, and carbon atoms are present in both samples. Sulfur is present in the "$CuInS_2$ as-deposited" sample, while selenium is present after selenization, as indicated by the Se 3p peaks at ~161 eV and Se 3d peaks at ~52 eV. After selenization, oxygen and carbon signals increase, and a sodium signal is found as well. Significant nitrogen and chlorine signals (likely from excess starting material) are found (only) before selenization, indicating that any excess starting material is removed by the selenization process. Note that the "$CuInSe_2$ as-deposited" sample survey spectrum shows a distorted background (and lower overall intensity due to a decaying channeltron in the analyzer – during the project, the old channeltron-based detector system was replaced by a high-count-rate delay-line detector).

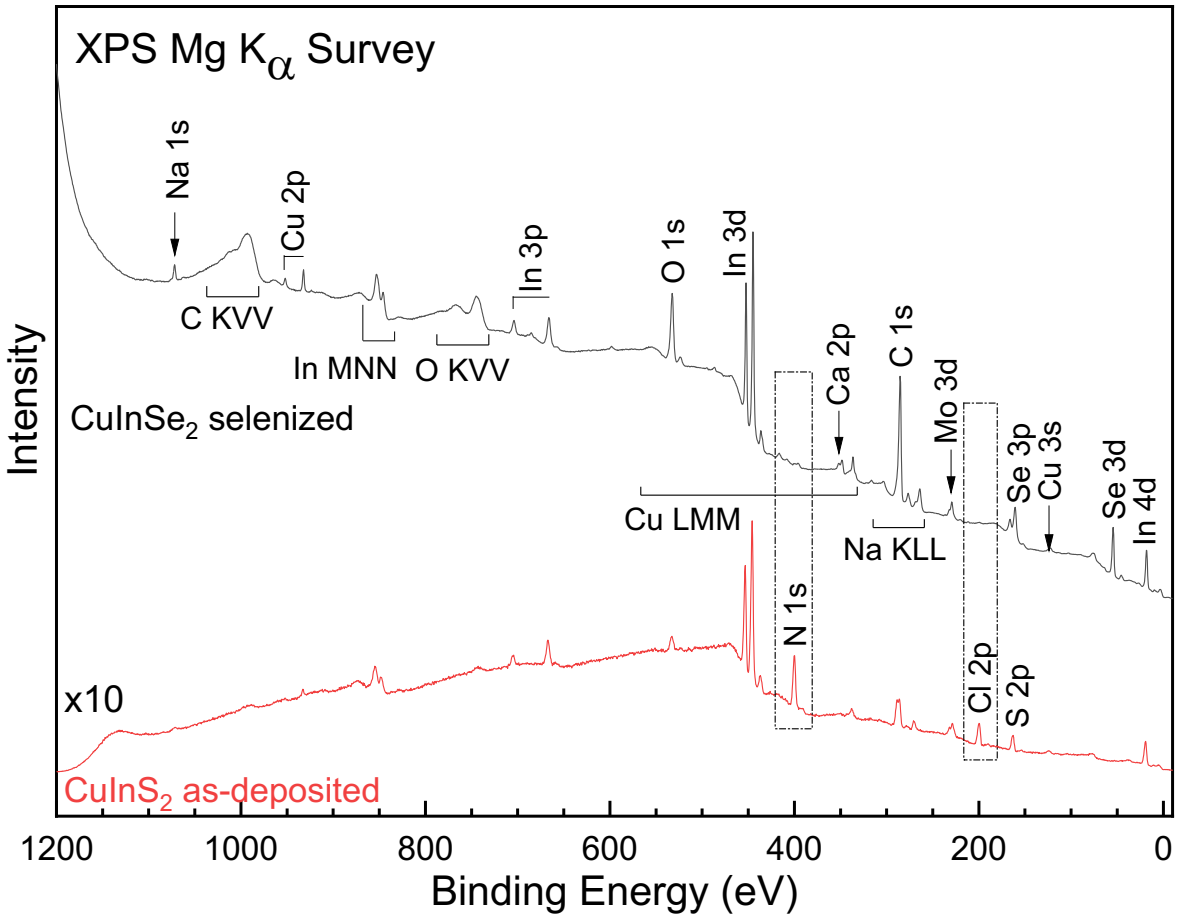

Figure 38. XPS survey spectra of the "$CuInSe_2$ selenized" and "$CuInS_2$ as-deposited" samples. Core level peaks and corresponding Auger transitions are identified. Several peaks are highlighted to indicate differences between each sample (see text).

Figure 39 shows the XES sulfur $L_{2,3}$ emission spectra of the "$CuInSe_2$ selenized" and "$CuInS_2$ as-deposited" samples (taken at a photon energy of 180 eV). In XES, core holes are created in a selected core level (here: S 2p), and the subsequent photon emission due to relaxation by electrons from the valence band is detected. XES hence gives combined insights into the chemical shifts of core levels and the valence electronic structure, which contains information about the local chemical bonding environment. Due to the photon-in-photon-out nature of the approach, this information is not only obtained from the surface, but also the surface-near bulk region.

Using In_2S_3 and $In_2(SO_4)_3$ reference materials (shown here), and previously published Cu-S-based systems, characteristic lines of various chemical environments of sulfur can be identified – corresponding to sulfur bonding with indium, copper, and oxygen. The "$CuInS_2$ as-deposited" sample shows transitions at ~153 eV (labeled (2)) and above, which indicates S-In bonding, and at ~159.5 eV, which reflects S-Cu bonding in the material. These peaks also appear in the $CuInSe_2$ annealed sample, in addition to peaks at ~155, ~156, and ~162 eV that correspond to sulfur in a S-O bonding environment.

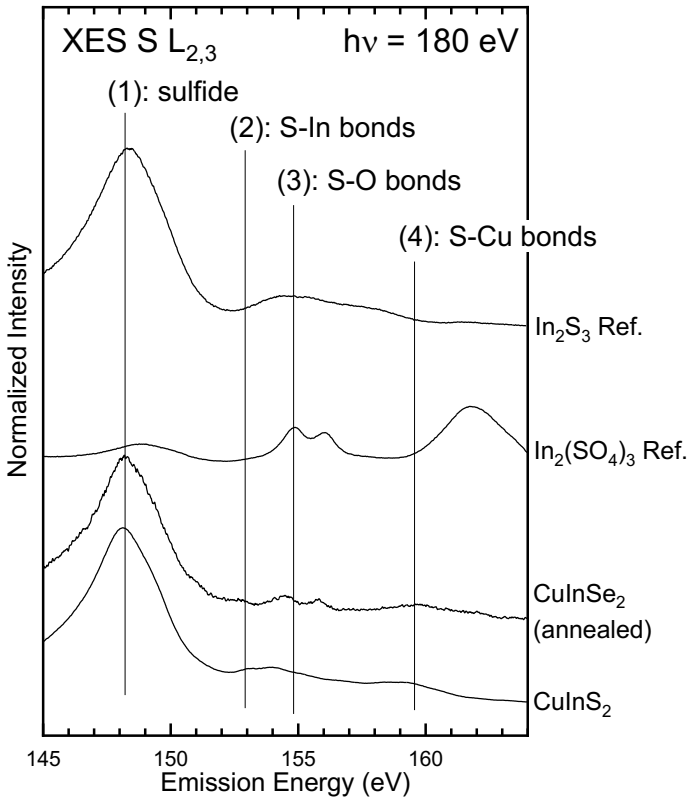

Figure 39. Sulfur $L_{2,3}$ XES spectra of "$CuInSe_2$ selenized" and "$CuInS_2$ as-deposited" samples, in addition to $In2S_3$ and $In_2(SO_4)_3$ references. Several chemical environments of sulfur can be identified (1-4) using the references.

Chemical characterization of solution-processed $CuIn(S,Se)_2$ absorber and $CuInS_2$ precursor synthesized using inks formulated in a controlled glovebox environment: To study the impact of different synthesis environments, especially with higher ambient control, another set of samples was prepared using a procedure similar to that described above, except that this time inks were synthesized in a glove-box (GB) and then spin-coated in air. One of the resulting $CuInS_2$ samples (labeled "GB HPLC $CuInS_2$ as-deposited") was then annealed in a selenium atmosphere to produce a $CuIn(S,Se)_2$ sample (labeled "GB HPLC $CuIn(S,Se)_2$ selenized"). The "HPLC" abbreviation refers to the HPLC-grade methanol used to prepare the inks. Figure 40 shows the XPS survey spectra of these samples. Like for the samples in the previous section, sodium is present, and chlorine and nitrogen are removed, after selenization. Additionally, oxygen is increased. Sulfur signals can be identified at ~162 eV (S 2p peaks) in the "GB HPLC $CuInS_2$ as-deposited" sample, and selenium can be identified at ~54 eV (Se 3d peaks) in the "GB HPLC $CuIn(S,Se)_2$ selenized" sample.

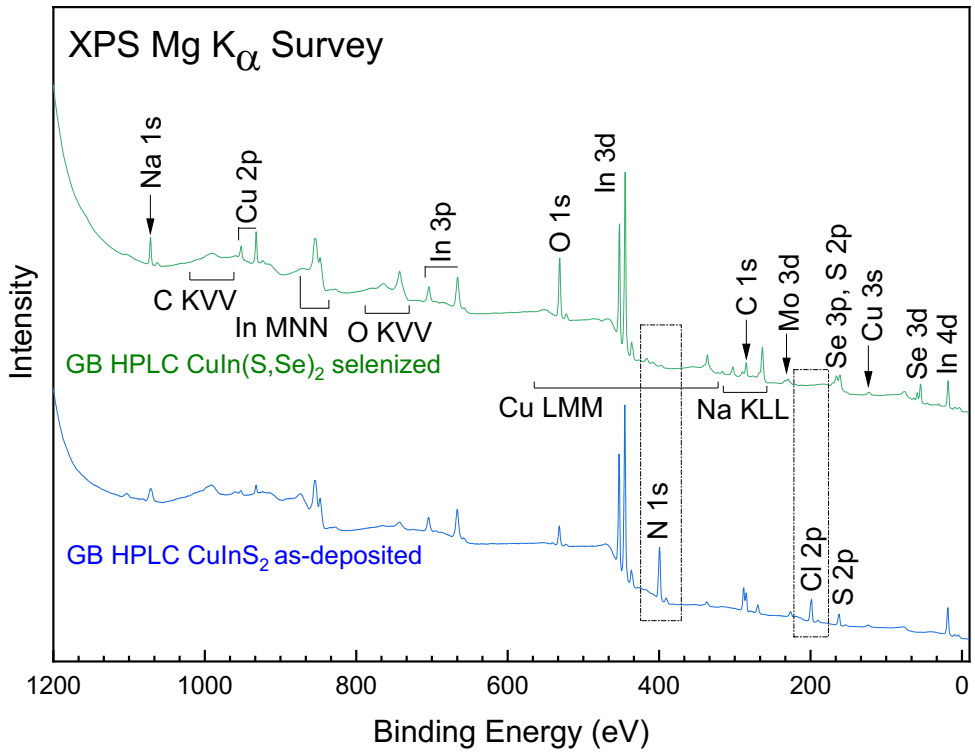

Figure 40. XPS survey of the "GB HPLC CuIn(S,Se)$_2$ selenized" and "GB HPLC CuInS$_2$ as-deposited" samples. Core level peaks and corresponding Auger transitions are identified. Several peaks are highlighted to indicate differences between each sample (see text).

Figure 41 shows XPS detail spectra of the Se 3d peaks of the "GB HPLC CuIn(S,Se)$_2$ selenized" (i.e., synthesized using an ink formulated in a glovebox environment) and "CuInSe$_2$ selenized" samples (i.e., synthesized using an ink formulated in air). The gray boxes represent the range of binding energies commonly found for various chemical environments of selenium. The "CuInSe$_2$ selenized" sample shows selenium in selenide environment. In contrast, the "GB HPLC CuIn(S,Se)$_2$ selenized" sample shows a selenide chemical environment in addition to a Se-O chemical environment. Apparently, at that stage of deposition development, one of the involved steps included an exposure to oxygen or moisture that led to an additional oxidation of Se atoms at the surface in this sample series.

Chemical and electronic characterization of "as-deposited" and "selenized" chalcopyrite absorbers with differing synthesis environments: Two sample sets were prepared in different synthesis and spin-coating environment to further understand the chemical and electronic differences between air-processed and glovebox-processed samples, in particular the oxidation behavior of the various chalcopyrite constituents. One sample set was synthesized using inks formulated in air and spin-coated in air ("Air"), and the other was synthesized using inks formulated in the glovebox *and* spin-coated in the glovebox ("GB"). Both sample sets each consist of a CuInS$_2$ (labeled "CIS as-deposited") and a CuIn(S,Se)$_2$ (labeled "CIS selenized") sample. The CuIn(S,Se)$_2$ samples were both processed by annealing as-deposited CuInS$_2$ samples in a selenium atmosphere.

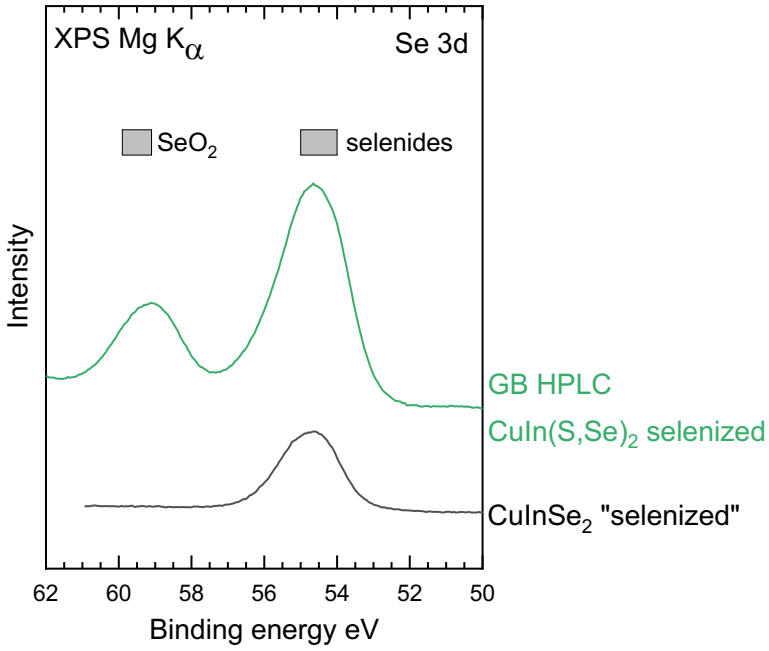

Figure 41. Detailed XPS spectra of the Se 3d region for the "GB HPLC $CuIn(S,Se)_2$ selenized" and the "$CuInSe_2$ selenized" sample. Grey boxes represent the range of Se 3d peak position for different candidate of selenium species.

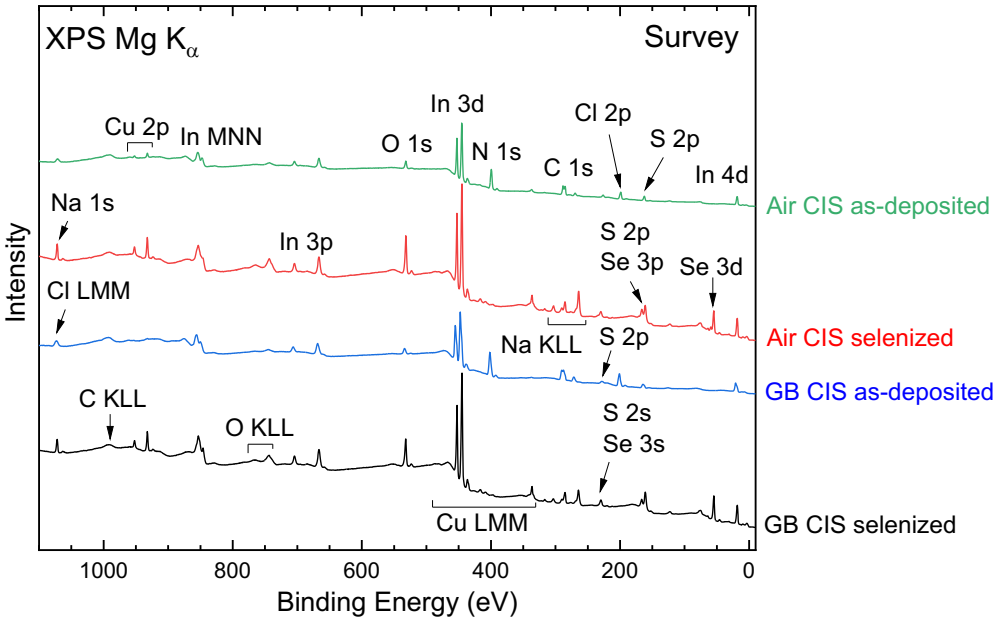

Figure 42. XPS survey spectra of the four samples studied, synthesized in Air or in Glove Box (GB), and before and after the selenization process.

Figure 42 shows the XPS survey spectra of both samples sets. All samples show the expected lines of copper, indium, sulfur, and selenium, in addition to carbon and oxygen adsorbates. Slightly larger adsorbate signals are found on the sample set that was synthesized using an ink formulated in air and spin-coated in air. The oxygen signals clearly increase after the selenization process for both types of samples. As for the sample sets in the previous sections, the selenization process also resulted in the removal of nitrogen and chlorine, as well as a significant presence of sodium (Na 1s at ~1072 eV and Na KLL Auger at ~266 eV in Fig. 5).

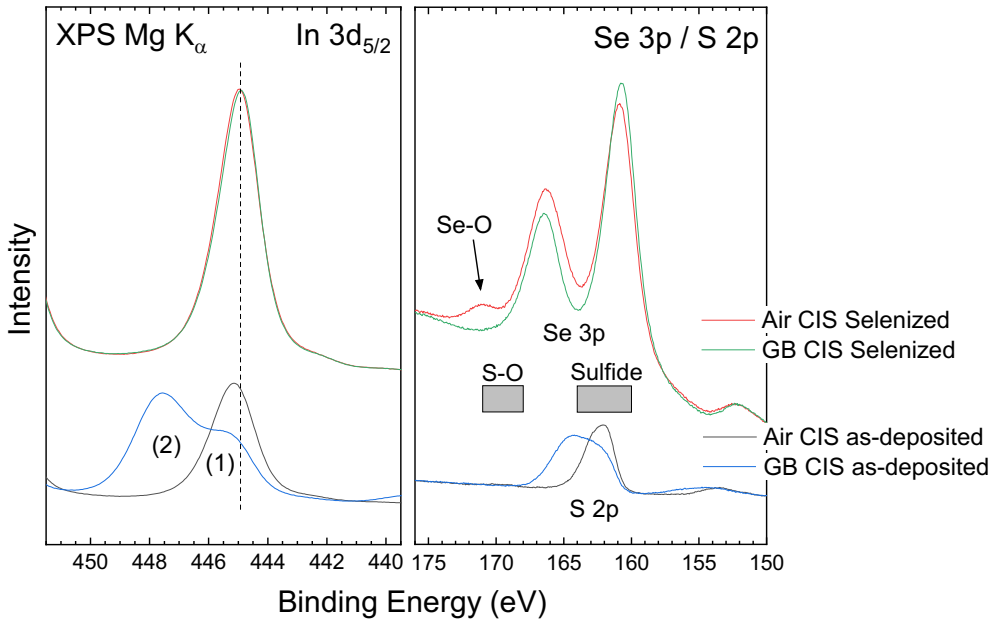

Figure 43. Mg K_α XPS detailed regions of the In $3d_{5/2}$, Se 3p, and S 2p peaks. For the In spectra, the dotted line indicates the binding energy of the selenized samples. Grey boxes in the Se 3p /S 2p panel represent different chemical environments of sulfur.

To identify the chemical environments of indium, selenium, and sulfur, Figure 43 shows the XPS detail regions of In $3d_{5/2}$, Se 3p, and S 2p. Furthermore, a Wagner plot to analyze the detailed chemical environment of In is shown in Figure 44 (more details of the spectra in Figure 43 will be discussed below). A Wagner plot uses the XPS binding energy and the kinetic energy of the most prominent Auger line (not shown) to create a two-dimensional depiction of the involved energy levels and transitions. As diagonals, the Wagner plot also shows the 'modified Auger parameter', which is created by adding the core level binding energy (i.e., of the In $3d_{5/2}$ core level) and the kinetic energy of the respective Auger peak (i.e. In $M_4N_{45}N_{45}$). The advantages of the modified Auger parameter include the elimination of any band-bending or charging effects (since they would result in an identical shift of both the photoelectric and Auger peak, which then cancel in the calculation).

The "GB CIS Selenized" and "Air CIS Selenized" samples show very similar chemical environments of indium. This is indicated in the In $3d_{5/2}$ peak (Figure 43) and very similar modified Auger parameters (red and green triangles in Figure 44). When comparing to reference data from the NIS database, it is evident that both samples show a $CuInS_2$-type bonding environment for In.

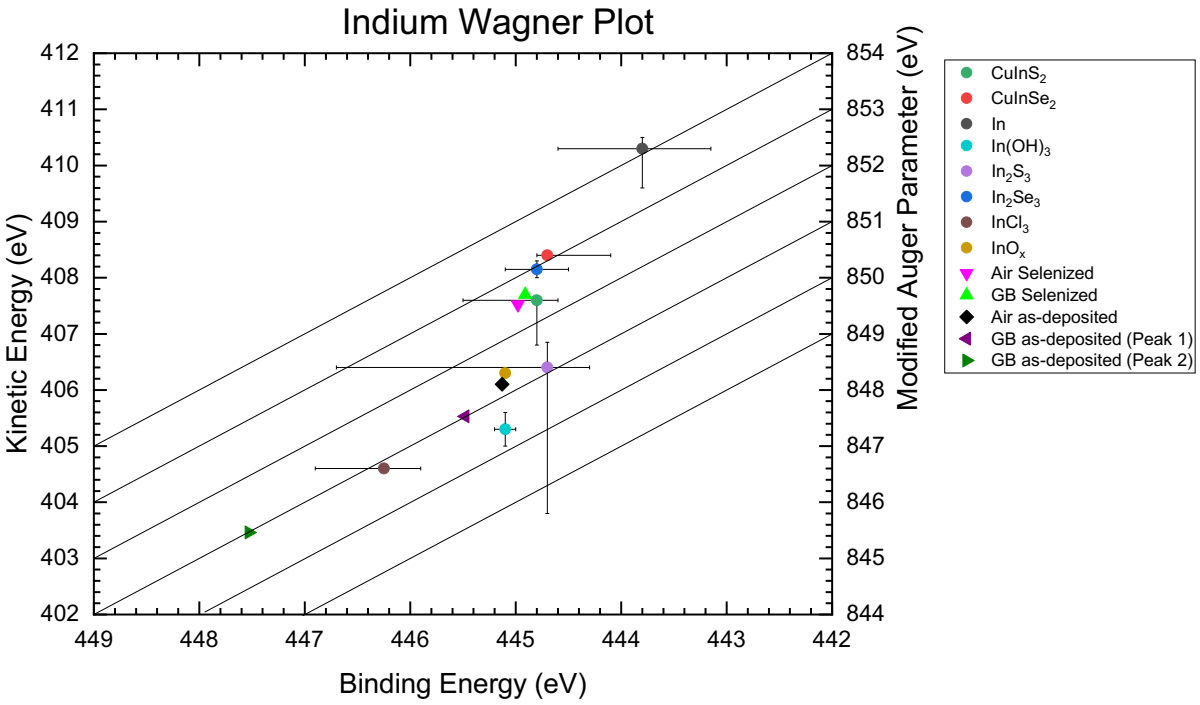

Figure 44. Wagner plot for indium. The kinetic energy is derived from the In $M_4N_{45}N_{45}$ Auger peak, and the binding energy is taken from the $3d_{5/2}$ photoemission peak. The modified Auger parameter (diagonal lines and right ordinate) is the sum of the two energies. The samples of this sample series are compared to several reference values from the NIST database.

The In peak of the "Air CIS as-deposited" sample is shifted in comparison to the selenized samples. Using the Wagner Plot in Figure 44, the "Air CIS as-deposited" sample is better described by an In_2S_3-like bonding. This is supported by the sulfide environment in the S 2p region of the "Air CIS as-deposited" sample (Figure 43, right panel). Two clearly different types of chemical environments are present at the surface of the "GB CIS as-deposited" sample, labeled (1) and (2) in Figure 43. Peak 1 represents an In-O type bonding (purple triangle in Figure 44), while Peak 2 likely represents In-Cl bonding (dark green triangle in Figure 44). The presence of Cl is confirmed in the Cl 2p region (not shown).

In the Se 3p and S 2p region (Figure 43), the "Air CIS as-deposited" sample is dominated by sulfide bonding, with a very weak contribution from S-O type bonding (represented by a spectral feature at ~171 eV). The sulfide bonding is likely due to In-S bonds, as discussed for the indium results. Similar to the findings for the indium region, the "GB CIS as-deposited" sample has multiple species of sulfur at the surface, as shown through a broadened sulfur 2p peak (to be discussed in more detail below). In the selenized samples, the 2p signature of the sulfur atoms has been completely replaced with the Se 3p lines. As in the case of the GB HPLC selenization, we find a clear indication of Se-O bond formation as well.

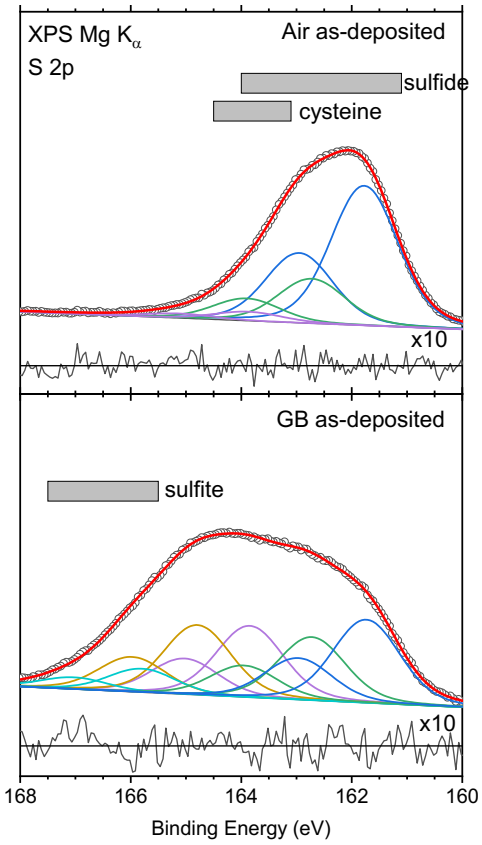

Figure 45. Sulfur 2p XPS peaks of the "Air as-deposited" (upper panel) and "GB as-deposited" (lower panel) samples. Voigt function doublets were used to fit the experimental data. The red lines represent the fit result, and the grey boxes represent tabulated binding energy ranges of different possible chemical environments of sulfur. The x10 magnified residual of both fits is show at the bottom of each panel.

To gain more insights into the various sulfur chemical environments in the "as-deposited" samples, several Voigt function spin-orbit doublets were fitted to the experimental data in Figure 45. Both spectra were fitted simultaneously, with coupled Lorentzian and Gaussian widths. The area of the 2p peaks were fixed with a 2:1 spin-orbit split ratio, according to the multiplicity of 2j+1. From the fits, several sulfur chemical environments are likely contributing to the signal for the "Air as-deposited" sample, in particular sulfur in a sulfide environment and sulfur in an organic, precursor-related environment (here represented by a cysteine reference). In detail, the components at ~161.7 and ~162.7 eV (Figure 45, upper panel) likely represent sulfur in slightly differing sulfide environments (such as Cu-In-S and S-In). The indium 3d peaks (Figure 43) support the presence of the two (or more) indium-sulfide-based species. The purple doublet with its main peak at ~164.0 eV is best ascribed to organic residue (indicated by comparison with the cysteine literature data).

Similar to the "Air as-deposited" sample, the analysis of the "GB as-deposited" sample also suggests multiple sulfide environments, albeit with a different relative spectral strength. Furthermore, the "organic" sulfur peak has a significantly greater contribution. And, finally, the additional peaks at ~164.8 and ~165.7 eV (Figure 45, lower panel) possibly represent additional thiol-like and S-O chemical bonding environments, respectively.

Using XES, the study of the local chemical environment of sulfur was completed with information about the valence states of these samples. As in XPS, XES shows multiple local bonding environments of sulfur as well, even with its more bulk-sensitive character. Figure 46 shows the S $L_{2,3}$ XES spectra of the two sample sets, together with various references to identify the different local bonding environments of sulfur. To analyze these spectra in a more detailed and quantitative way, two approaches were followed, namely (1) a multi-component fit with reference spectra, and a (2) a difference spectrum approach.

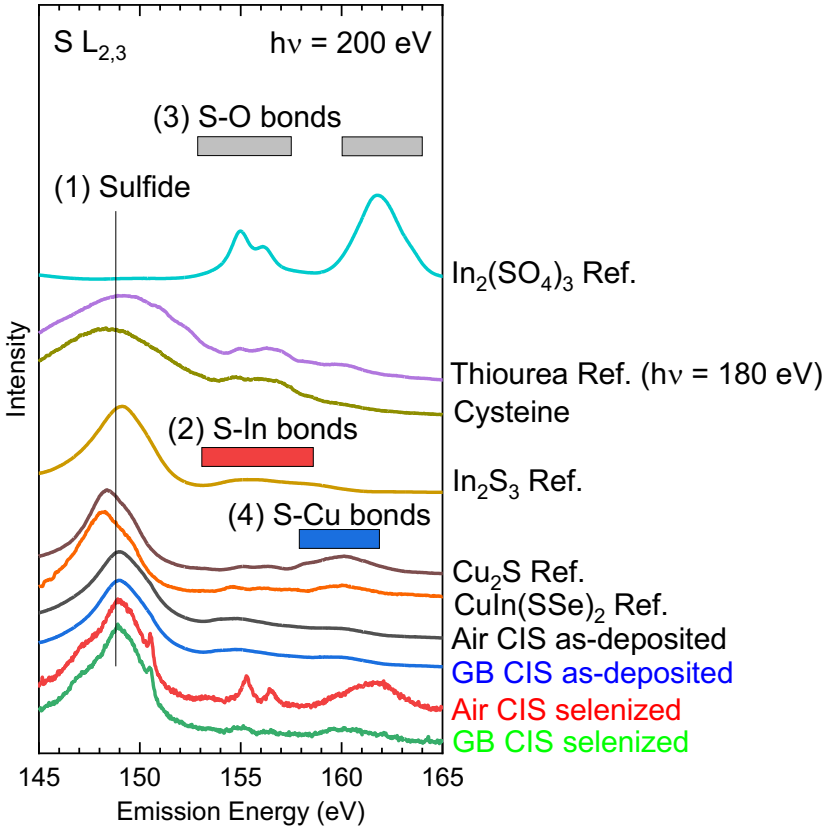

Figure 46. S $L_{2,3}$ XES spectrum of the "Air as-deposited" and "GB as-deposited" samples. References are shown to identify various spectral features that correspond to different local bonding environments, such as (1) sulfide, (2) S-In, and (3) S-Cu bonds.

First, a multi-component fit using reference spectra (namely In_2S_3, $CuInS_2$, Cu_2S, and cysteine) was performed to quantify the various components in the "GB as-deposited" spectrum. This is shown for the upper valence band region of the "GB as-deposited" sample in Figure 47. The fit shows that a combination of such binary references, plus a suitable "organic" component, can be well employed to describe the electronic structure of this complex sample. Clearly, S-Cu bonds need to be included to account for the intensity at ~160 eV, while S-In bonds are at play when describing the intensity at ~155 eV and below. Note that the S $L_{2,3}$ XES spectrum of the "GB CIS selenized" has a similar spectral shape as the "CISSe reference" spectrum, in particular the regions indicating S-In and S-Cu bonding, and is thus not reproduced here.

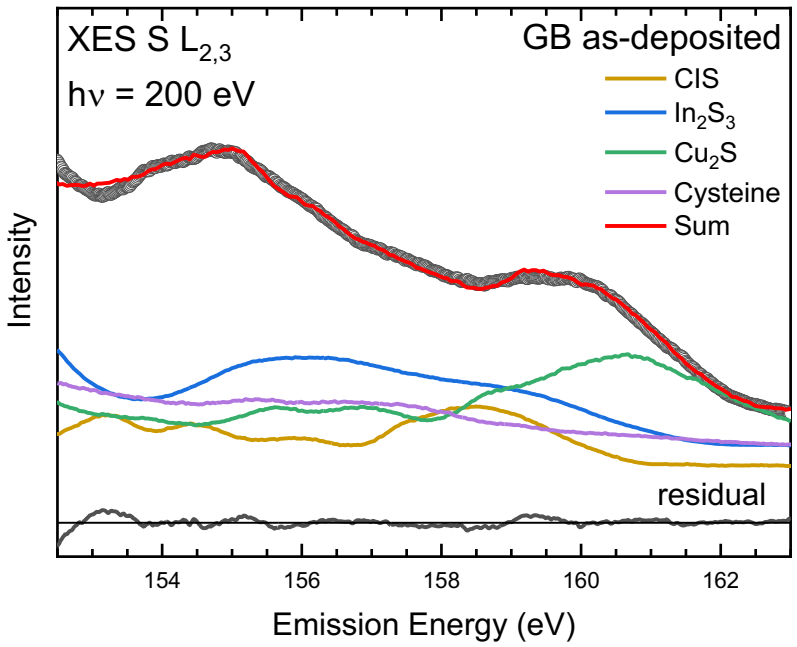

Figure 47. Resulting fit of the upper valence band region in the S $L_{2,3}$ XES spectrum of the "GB as-deposited" sample. $CuInS_2$, In_2S_3, Cu_2S, and cysteine references with varying ratios and appropriate energy shifts were applied to give an optimal description of the experimental data.

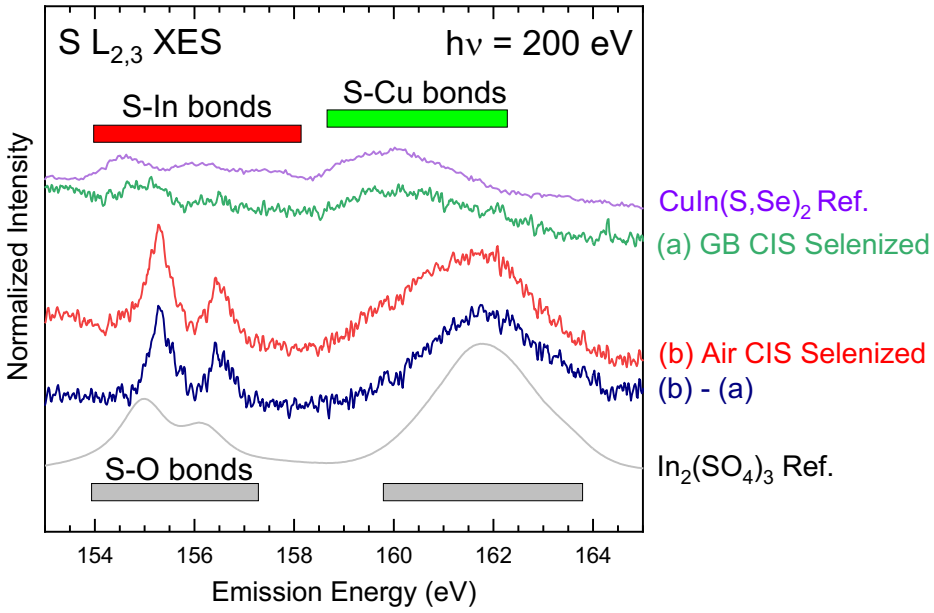

Figure 48. XES spectra of the "GB CIS Selenized" and "Air CIS Selenized" samples, compared with $CuIn(S,Se)_2$[19] and $In_2(SO_4)_3$ references. "(b) – (a)" represents a difference spectrum of "Air CIS Selenized" minus "GB CIS Selenized". Colored boxes indicate peaks of primary relevance for different bonding environments (S-In, S-Cu, and S-O bonds).

A direct comparison of the reference and the "GB CIS selenized" spectra, together with a difference spectrum approach, is shown in Figure 48. The "Air CIS selenized" sample shows spectral features similar to the "CISSe reference", but also clear spectral features at ~154, ~155, and ~161 eV, similar to the $In_2(SO_4)_3$ reference. This is quantified by subtracting the "GB CIS Selenized" sample from the "Air CIS Selenized" sample, which reveals a spectrum similar to the $In_2(SO_4)_3$ reference, most noticeably the removal of the S-Cu spectral feature at 161 eV shown in Figure 48. This suggests that the "Air CIS Selenized" sample consists of two components, $CuIn(S,Se)_2$ and sulfur oxides, at/near the surface. This is not unexpected, as oxides are also found at the surface in the Se 3p/ S 2p region (Figure 45).

To gain insights into the electronic structure of the samples, the VBMs of the four sample surfaces were determined using linear extrapolations of the leading edge in UPS spectra. The results are shown in Figure 49. Both "as-deposited" samples have a larger VBM in comparison to the "selenized" samples, likely due to the presence of excess starting material (such as $InCl_3$ and nitrogen-containing species) overlaying the true $CuInS_2$ absorber spectrum. This is apparent from the peak fits in the "GB as-deposited" sample in Figure 45; $CuInS_2$ is not a dominant species at the surface of the sample. With the removal of $InCl_3$ and other excess starting materials after the selenization process, the VBM becomes smaller (i.e., an upward shift), more closely representing the VBM of $CuIn(S,Se)_2$. The reduction in the VBM is not as drastic for the sample set spin coated in air using ink formulated in air, since the spectrum of the "Air as-deposited" sample already contains a larger fraction of the "true" absorber surface. From the valence band structure shown in Figure 49, Cu 3d-derived states can also be seen at ~3 eV. The spectral weight of the Cu 3d-derived states increases after the selenization process, which is also supported by the increase in Cu 2p XPS peak intensity in the selenized samples (not shown).

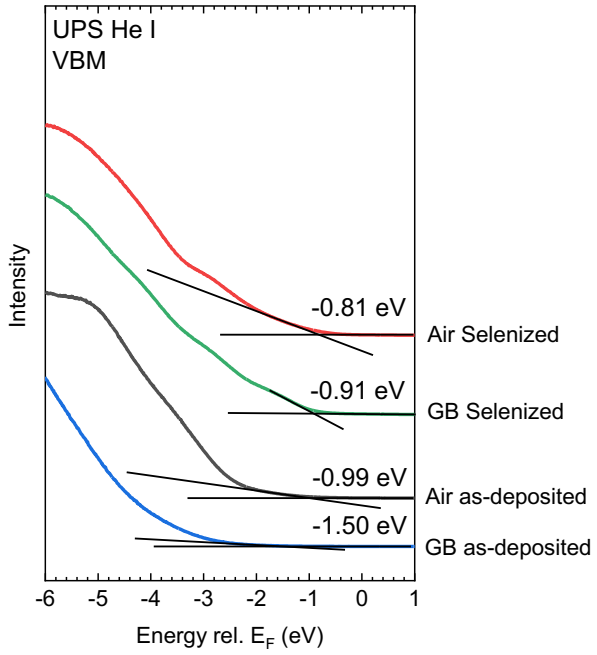

Figure 49. UPS (He I) Valence band spectra of the four samples. The valence band maxima were determined using linear extrapolations of the leading edge.

Lastly, AFM was used to uncover the differences in surface morphology of the "Air as-deposited" and "Air selenized" samples. Figure 50 shows 15x15 μm^2 images of the two samples. Horizontal lines near the top of each image mark the position of the line profiles presented in Figure 51. The sample morphology changes significantly between the as-deposited and selenized samples. In the left image, the as-deposited sample exhibits smaller grains with a diameter of ~1 µm, distributed throughout the substrate. In contrast, after selenization (Figure 50, right image), larger grains with a size of ~3 µm are formed. Overall, both samples have a rough surface, as shown by the line profiles in Figure 51. Additionally, Figure 50 suggests that the distribution of the material is not homogenous for both the "Air as-deposited" and "Air Selenized" samples. This is indicated by darker regions, especially in the lower left corner of both images.

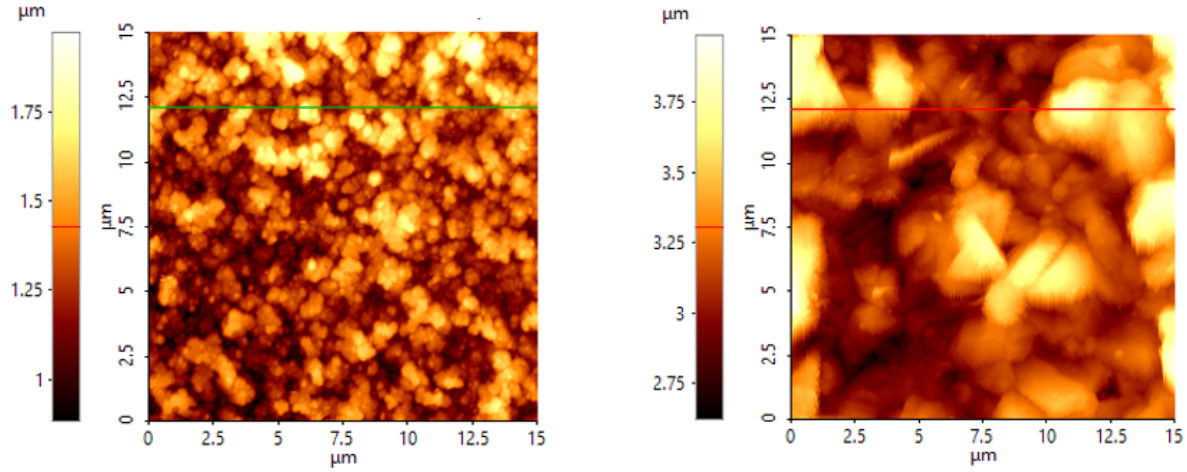

Figure 50. 15x15 μm^2 AFM images of the "Air as-deposited" (left image) and "Air selenized" (right image) samples. Differences in color shades represent differences in height; the height scale (in µm above an assumed zero) is shown on the left of each image. Lines present on the images indicate the location of the line profiles depicted in Figure 51.

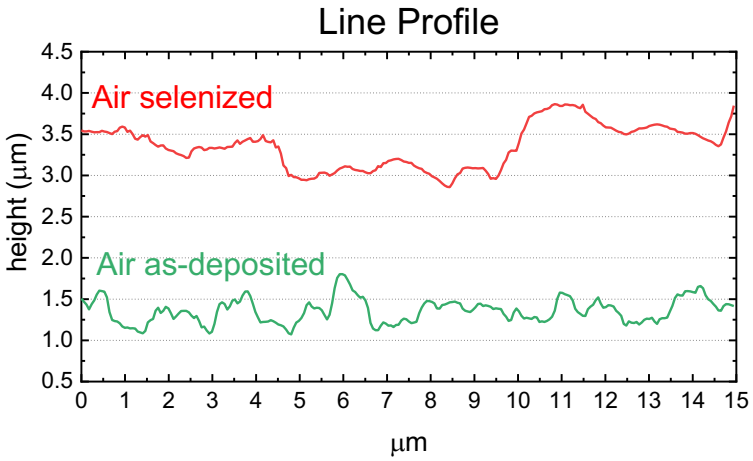

Figure 51. Line profiles of the "Air selenized" (red) and "Air as-deposited" sample (green). The locations of the line profiles are indicated near the top of the images in Figure 50.

Chemical characterization of boron-containing chalcopyrite absorbers: Initial studies of boron incorporation into chalcopyrite absorbers were performed on a sample set consisting of two $CuInB(S,Se)_2$ (CIBSSe) absorbers with different B/(B+In) ink ratios - 30% and 10% (labeled as "CIBSSe 30%" and "CIBSSe 10%", respectively). These samples were measured with XPS and XAES to identify the presence of boron, uncover their composition, and, if possible, gain insights into the local chemical bonding environment of boron at the surface.

Figure 52 shows the XPS survey spectra of the "CIBSSe 30%" and "CIBSSe 10%" samples. Expected peaks of copper, indium, sulfur, and selenium are present. Adsorbate-related peaks, such as oxygen and carbon, are also found, together with sodium (as indicated by the Na 1s peak), likely from the Mo-coated soda lime glass substrate. At this scale, no indication of a B 1s peak is seen / this will be discussed below in conjunction with detail spectra of that region. Although the samples were made with similar processing techniques, the Cu/(Cu+In) ratio is much higher in the "CIBSSe 30%" sample in comparison to the "CIBSSe 10%" sample. This can be easily seen by comparing the peak intensity of the Cu 2p peaks to the In MNN Auger peaks.

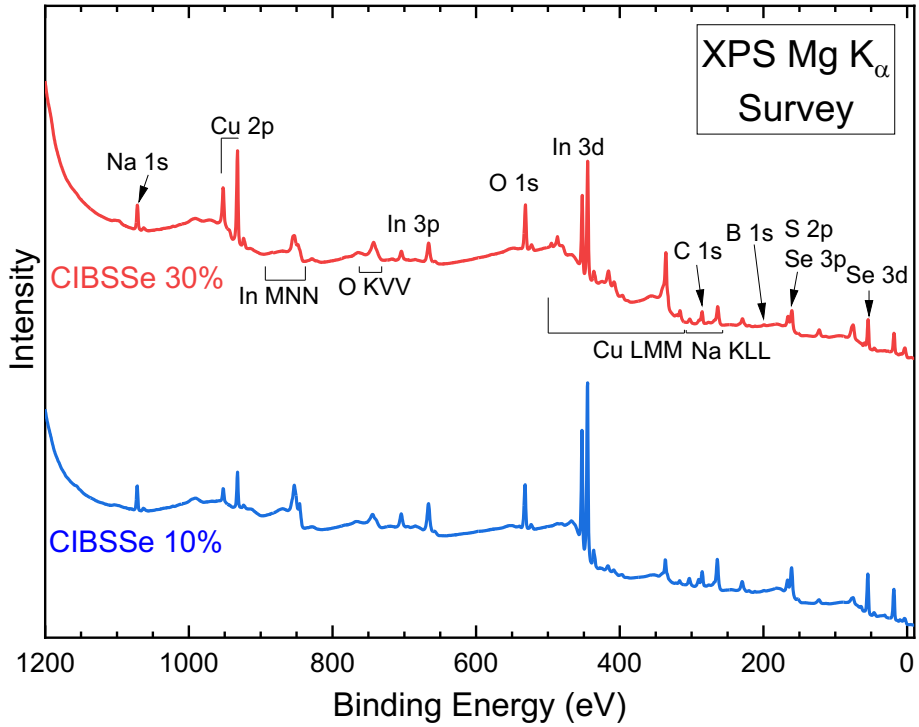

Figure 52. Mg K_α XPS survey spectra of the "CIBSSe 30%" and "CIBSSe 10%" samples. Prominent photoemission and Auger peaks are labeled.

Detail regions of the B 1s peak region are shown in Figure 53 for both samples. The as-measured spectra are shown in the upper panel. Due to the low intensity of the B 1s peak, a linear background subtraction was applied to both spectra, the result of which is shown in the lower panel. The low intensity of B 1s point to a low concentration of boron at the surface. Additionally, we point out that the photoionization cross section of the B 1s core level for the Mg K_α x-ray source is rather low (compared to 1.0 for the C 1s core level). As mentioned, the top panel of Figure 53 shows the raw data in the B 1s detail region; additionally, the chosen linear background is shown as well.

The spectra after background subtraction (Figure 53, bottom panel) show a broad B 1s intensity distribution, indicating multiple chemical environments of boron at the surface. Both samples show a similar spectral shape after linear background subtraction, suggesting similar chemical environments in both samples, but with differences in peak intensity (note the magnification factors for the raw and background-subtracted "CIBSSe 10%" sample). Among the likely boron environments, we identify a B-S or a Na-B-O chemical environment, as the peak intensity overlaps with literature data[20] of $Na_2B_4O_7$ and B_2S_3 (and we find a strong Na 1s signal on these surfaces). We also note that there are no published references with a peak energy of ~190 eV. The intensity in this region could indicate boron in a CIBSSe chemical environment.

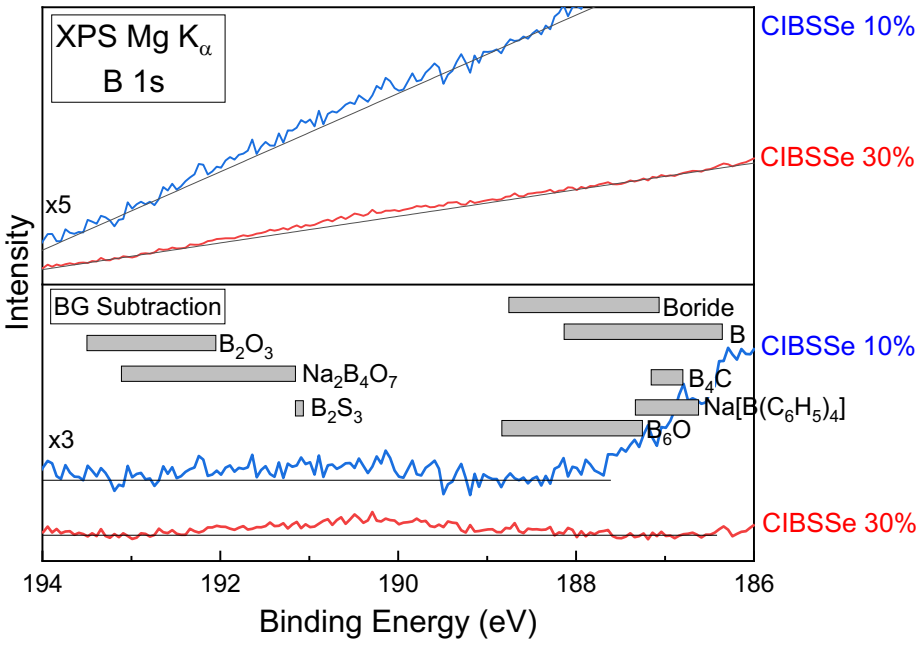

Figure 53. Mg K_α XPS detail regions of the boron 1s peak for the "CIBSSe 10%" and "CIBSSe 30%" samples. Top panel: linear baseline chosen for the spectra. Bottom panel: residual spectra after background subtraction. Grey boxes represent different chemical environments of boron.[20]

Chemical and electronic characterization of CdS/CISSe and CdS/Al-CISSe surfaces : Lastly, two sample sets were prepared to understand the surface and interface properties when adding Al to the absorber composition before forming the chalcopyrite absorber and its interface with a CdS buffer layer. One sample set included chalcopyrite absorbers similar to the samples described in previous sections, i.e., the $CuInS_2$ precursor (labeled "CIS as-deposited") was synthesized using CuCl, $InCl_3$, and thiourea. The $CuIn(S,Se)_2$ sample (labeled "CISSe selenized") was again prepared by annealing of the $CuInS_2$ precursor in a selenium atmosphere. Furthermore, two samples with a thin and thick CdS buffer layer on the $CuIn(S,Se)_2$ absorber were grown. The thickness was defined by the deposition time of 1 and 8 min (labeled "1 min CdS/CISSe" and "8 min CdS/CISSe", respectively). Using similar preparation method, the other sample set included chalcopyrite absorbers with Al incorporated into the synthesis process. The precursor is labeled "Al-CIS as-deposited" and is synthesized using CuCl, $InCl_3$, $AlNO_3$, and thiourea. The selenized sample is labeled "Al-CISe selenized", as no sulfur is present at the surface of the sample. Within

the sample set, a thin CdS buffer layer of 1 min deposition time (labeled "1 min CdS/Al-CISe") and a thick CdS buffer layer of 8 min deposition time (labeled "8 min CdS/Al-CISe") were deposited onto the "Al-CISe selenized" sample.

All samples were subjected to a 5 min, 50 eV Ar+ ion treatment to remove adsorbates, as adsorbates impact the characterization of absorber surfaces. However, exposure to the x-ray source and e- gun also "cleans" the surface (i.e., removes some adsorbates such as water), shown in Figure 54. "Initial survey (as-received)" represents the XPS survey spectrum taken when the sample was first exposed to x-rays, while "Final survey (as-received)" represents the XPS survey spectrum after ~6 hours of x-ray exposure. Similarly, "Initial survey (5 min ion treatment) and "Final survey (5 min ion treatment)" represent the XPS survey spectra taken after 5 min of low-energy ion treatment. An XPS survey spectrum was taken after ~12 hours of e- gun exposure (during an IPES measurement) – it is labeled "post-IPES" and was taken before the 5 min ion treatment. From the surveys, a decrease in O and C signals occurs after each XPS measurements, leading to an increased intensity of absorber-related peaks (e.g., the In 3d peaks). All spectra shown in this section were recorded after the 5 min Ar+ ion treatment step, i.e., with minimal amounts of adsorbates.

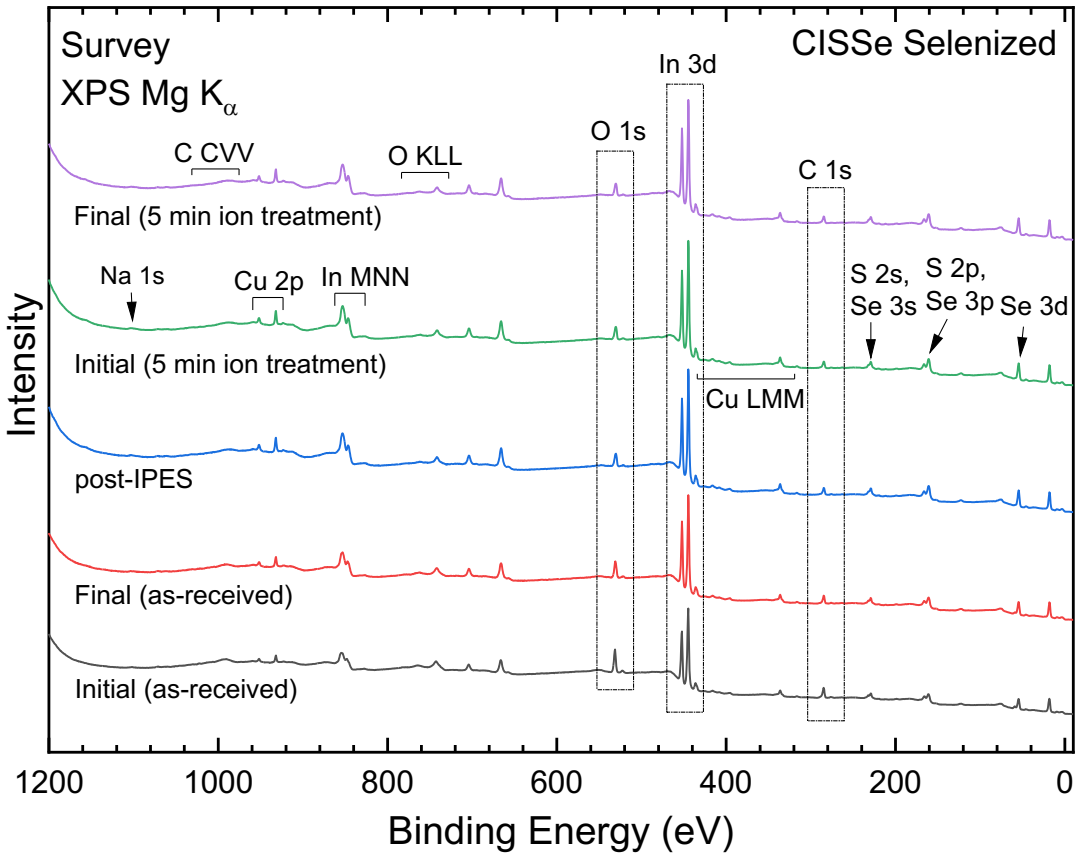

Figure 54. Mg K_α XPS survey spectra of the "CISSe selenized" sample samples. Prominent photoemission and Auger peaks are labeled. Several peaks are highlighted to indicate differences between each sample (see text).

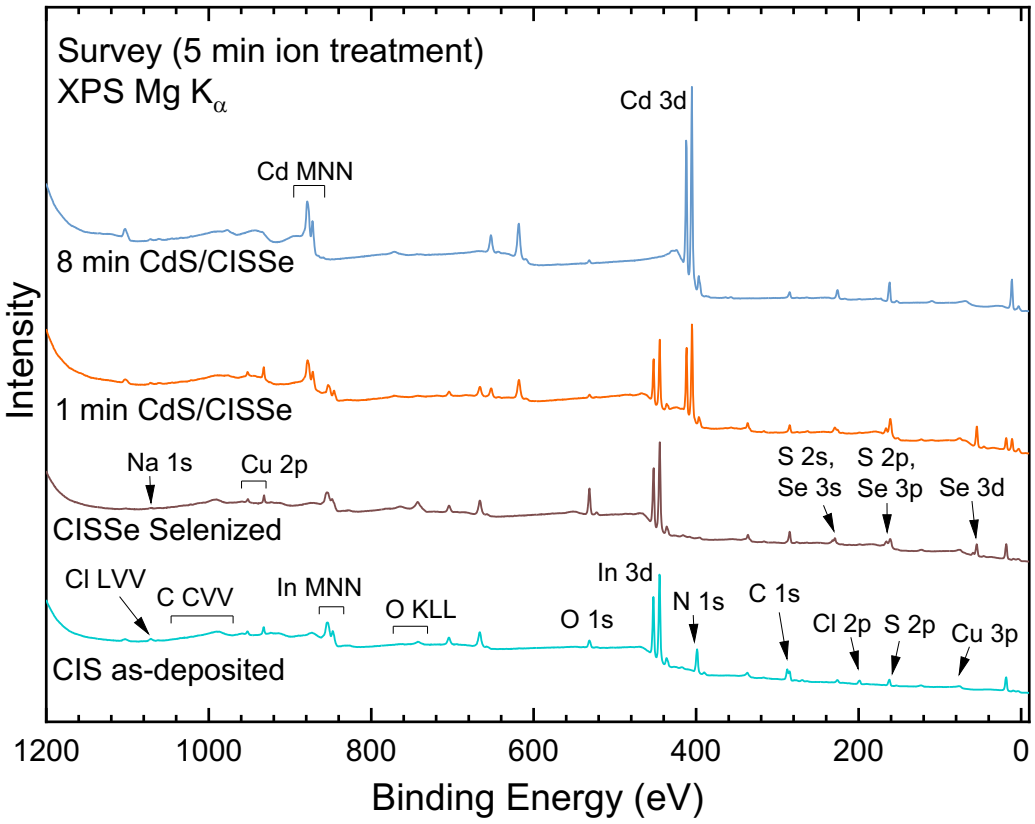

Figure 55. Mg K_α XPS survey spectra of the "CIS as-deposited" and "CISSe selenized" absorber surfaces, as well as the CdS/CISSe interface samples. Prominent photoemission and Auger peaks are labeled.

Figure 55 shows the XPS survey spectra of the sample set containing the (Al-free) $CuIn(S,Se)_2$ absorbers. The "CIS as-deposited" and "CISSe selenized" samples closely resemble the XPS survey spectra presented in Figure 42. Similar to past sample sets, removal of chlorine and nitrogen occurs after selenization. Additionally, the presence of cadmium-related signals (Cd 3d and Cd MNN) is observed after 1 and 8 mins of CdS deposition, and no absorber related peaks can be observed after the 8 min deposition of CdS. Detail regions of the Cu 2p and S 2p/Se 3p lines are shown in Figure 56. The "CIS as-deposited" sample again shows multiple chemical environments of sulfide present. A weak sulfate signal is present at ~169 eV as well, which is not unexpected as the synthesis process occurs in air. After selenization, selenium is present (in a selenide environment), with some sulfur remaining, as shown by the weak shoulder at ~162 eV. The presence of sulfur is also confirmed by the observation of S KLL peaks (not shown). In the "1 min CdS/CISSe" spectrum, the spectral feature at ~162 eV increases, as expected for the growth start of the CdS layer. A sulfide environment is clearly present after the 8 min deposition of CdS. Analyzing the Cu 2p peaks of the "CIS as-deposited" sample, the width of the peak suggests multiple environments of copper. For example, some excess CuCl from the starting materials likely remains on the surface. After selenization, the copper intensity increases significantly and the width of the Cu $2p_{3/2}$ peak remain the same. Due to the removal of chlorine after selenization, CuCl is also likely removed after selenization. However, copper sulfides and selenides might also be present, in addition to the CISSe main phase.

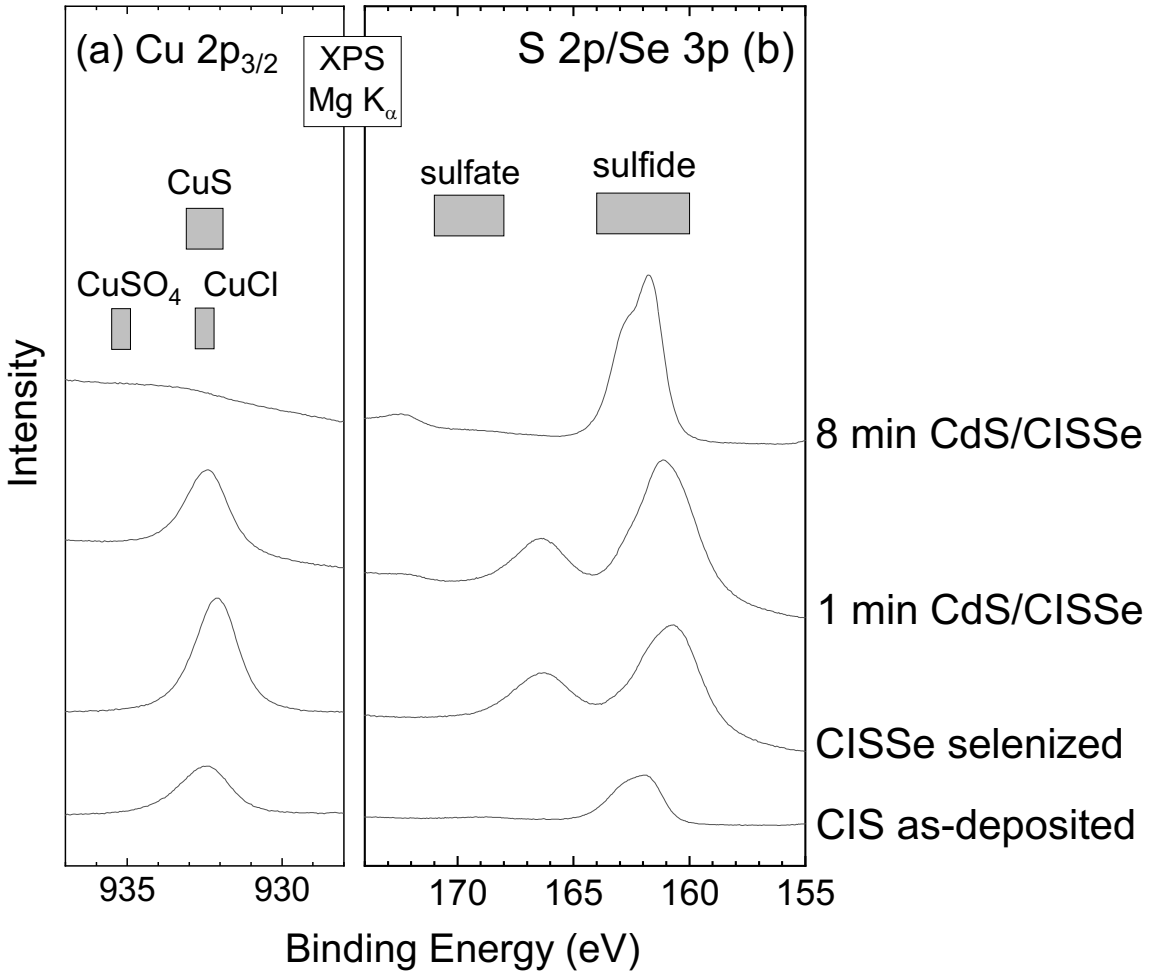

Figure 56. Mg K_α XPS detail regions of (a) the Cu 2p and (b) Se 3p/S 2p peaks. Grey boxes in the panel represent candidates for the different chemical environments of sulfur and copper present on the samples.

Figure 57 shows the He I UPS and IPES spectra of the "CISSe" selenized absorber and the CdS/CISSe sample with the thickest buffer layer (8 min deposition). The band edges of each spectrum were determined using linear extrapolations (in red) to derive the band offset at the interface, as well as the electronic surface band gap for each sample. The VBMs were found to be -0.60 and -1.68 eV for the CISSe and CdS/CISSe samples, respectively. The CBMs were found to be 0.22 eV and 0.79 eV for the CISSe and CdS/CISSe samples, respectively. This results in surface bands of 0.82 eV for the CISSe and 2.47 eV CdS/CISSe sample (±0.15 eV). The CISSe bandgap is unusually small for a chalcopyrite absorber, likely due to the presence of copper sulfides and/or selenides at the surface, as described in conjunction with the XPS results. The CdS/CISSe sample shows an electronic surface band gap well comparable to other CdS/chalcopyrite interface systems.[21]

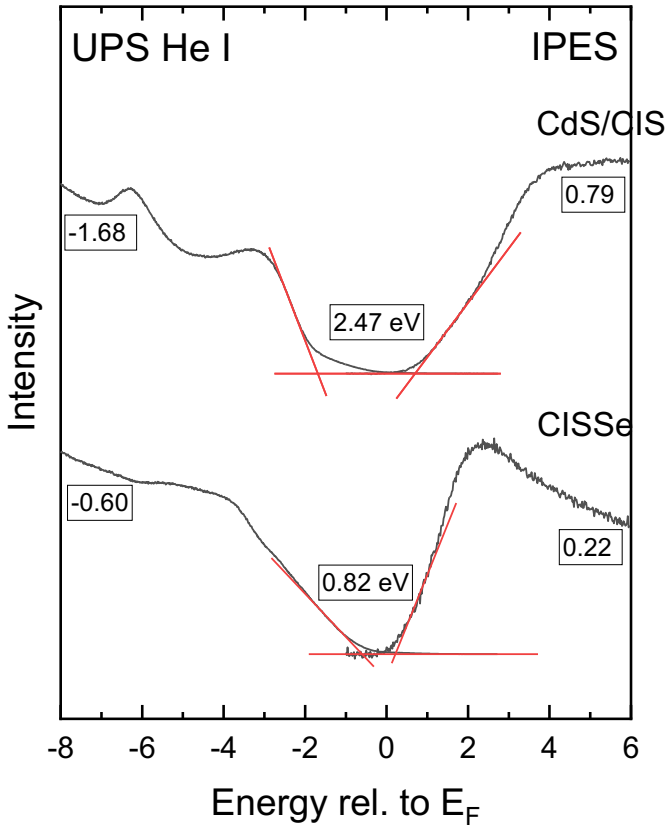

Figure 57. UPS (left) and IPES (right) spectra of the CISSe absorber and CdS/CISSe sample of the thickest buffer layer (8 min deposition). The band edges (in red) were determined using linear extrapolations of the leading edge.

The XPS survey spectra of the Al-incorporated chalcopyrite sample set are shown in Figure 58. They are very similar to the CISSe sample set and show aluminum at the surface, best seen with the presence of Al 2p and KLL peaks. Similar to the other sample sets, chlorine and nitrogen are present in the 'as-deposited" samples and removed after selenization. After selenization, the oxygen signal (O 1s) also increases. Figure 59 shows various detail regions of the Al-containing sample set. Al KLL peaks were used to identify the presence of aluminum due to the overlapping peaks of Cu 3s and Al 2p. The "as-deposited" sample again shows multiple chemical environments of sulfur, copper, and aluminum, likely due to excess starting materials. After selenization, the selenium completely replaces sulfur. No spectral feature of sulfur can be seen at ~163 eV in the "Al-CISe selenized" sample and no peaks are present in the S KLL region (not shown). As expected, the spectral feature at ~163 eV is present after 1 min deposition of CdS. No sulfate is present in the "as-deposited" sample, but some sulfate might be present in the "8 min CdS/Al-CISSe" sample. The width of the Cu $2p_{3/2}$ also suggests the presence of some excess starting material (i.e., CuCl) and the intensity of copper increases after selenization. The chemical environment of aluminum is likely an oxidized form (AlO_x) on the "Al-CIS selenized" and "1 min CdS/Al-CISe" samples. A very weak aluminum signal is still present after deposition of the thickest buffer layer – suggesting aluminum diffusing to the surface or a somewhat inhomogeneous thickness distribution of the CdS layer.

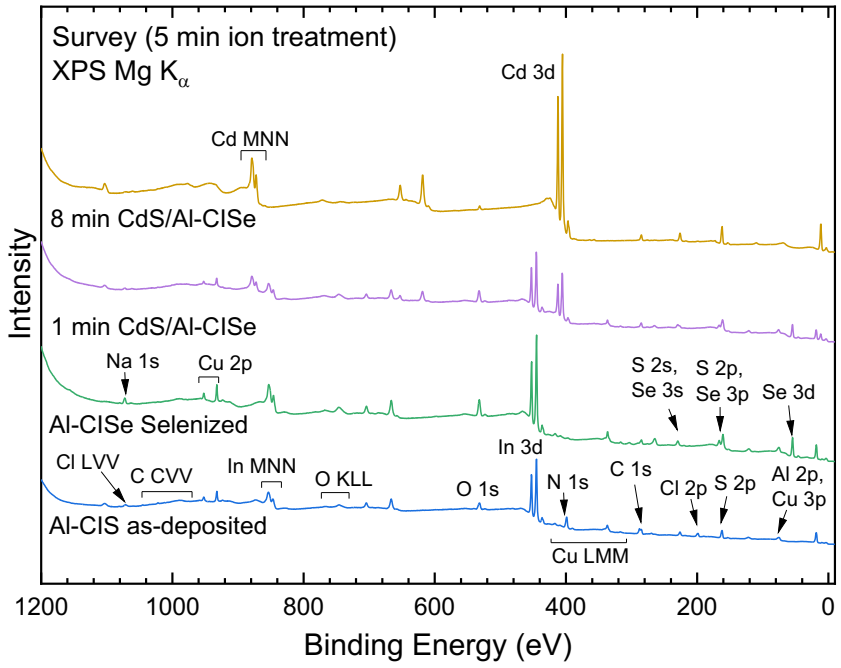

Figure 58. Mg Kα XPS survey spectra of the "Al-CISe selenized" sample set. Prominent photoemission and Auger peaks are labeled.

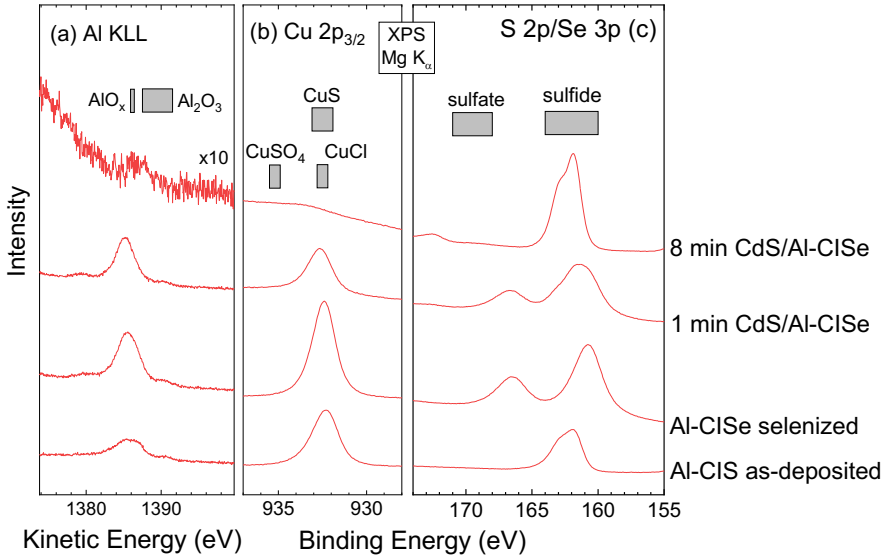

Figure 59. Mg Kα XPS detail regions of (a) the Al KLL, (b) Cu 2p, and (c) S 2p/Se 3p peaks. Grey boxes in the panel represent candidates for the different chemical environments of sulfur, copper, and aluminum present on the samples.

For comparison, Figure 60 shows the He I UPS and IPES spectra of the "Al-CISe" selenized absorber and the CdS/Al-CISSe sample with the thickest buffer layer (8 min deposition). The band edges of each sample were again determined using linear extrapolations. The VBMs are found to be -0.80 eV and -1.83 eV for the Al-CISe and CdS/Al-CISe samples, respectively. The CBMs

were derived to be 0.48 eV and 0.72 eV for the Al-CISe and CdS/Al-CISe samples, respectively. This results in electronic surface band gaps of 1.28 eV for the Al-CISe and 2.55 eV CdS/Al-CISe sample (±0.15 eV). The surface band gap of the Al-CISe surface is larger than that of the CISSe sample. Here, the incorporation of aluminum might lead to an overall widening of the bandgap and/or the removal of Cu species that led to an unusually small band gap in the Al-free case. The Cu 3d-derived states in the Al-CISe UPS spectrum are indeed weaker than in the CISSe UPS spectrum, but further analysis of the Cu data will be required to fully clarify this point. The bandgap for the CdS/Al-CISe sample is also slightly wider than the CdS/CISSe, but well within the error bars. The small difference in bandgap can be possibly attributed to the above-discussed Al surface diffusion and/or inhomogeneities in CdS film thickness (and properties).

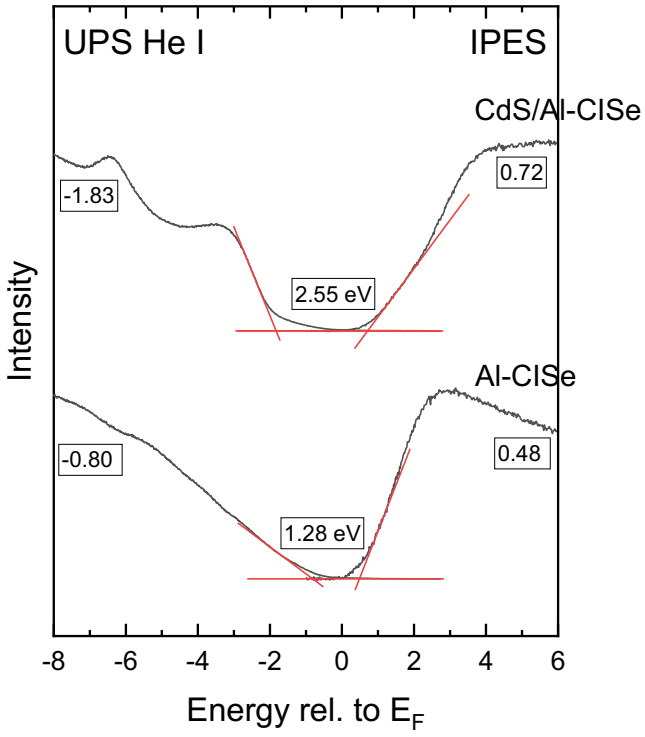

Figure 60. He I UPS (left) and IPES (right) spectra of the CdS/Al-CISe absorber and the CdS/AlCISe sample with the thickest buffer layer (8 min deposition). The band edges (in red) were determined using linear extrapolations of the leading edges.

Summary: Using a combination of electron and soft x-ray spectroscopies, both in the lab at UNLV (XPS, UPS, XAES, IPES), as well as at the ALS in Berkeley (XES), detailed insights into the complex electronic and chemical properties of solution-processed chalcogenide materials, their surfaces, and their interfaces could be obtained. Different preparation conditions as well as alloying partners could be investigated, and their development and optimization for PEC applications at our project partner in Hawaii could be supported with detailed insights into compositional and preparational variations, including surface adsorbates and precursor residues. Further data analysis is currently ongoing, and will be published in Amandee Hua's UNLV dissertation, as well as several peer-review publications, in the course of 2022.

b. Protection against photo-corrosion

A key challenge in PEC water splitting has been demonstrating technologically-relevant durability in the corrosive aqueous environments required for their operation.[22] Few semiconductors with high solar energy conversion efficiency have demonstrated intrinsic chemical stability while exposed to water under illumination. As a result, a common approach for solar water splitting devices involves physically isolating the light absorbing material from the electrolyte using a coating, while maintaining good optical transmittance and electrical conductivity through this layer.[23–25] For the hydrogen-evolving half-cell, studies have shown continuous operation for longer than ten days either by employing titanium dioxide (TiO_2) or molybdenum disulfide (MoS_2) coatings on silicon absorbers,[26–28] or by constructing their photoactive junction using a semiconducting material that achieves long-term operability in contact with the electrolyte.[6,29–32]

In seeking to fabricate a PEC device with high theoretical efficiency for water splitting and long-term operational durability, we selected ordered vacancy compound material copper gallium selenide ($CuGa_3Se_5$) as a candidate absorber for several reasons: 1) given that its 1.84 eV band gap is wider than that of many state-of-the-art chalcopyrite PEC absorbers,[10,29,31,33–44] it has the potential to produce the >1 V photovoltage[11] required to enable efficient tandem unassisted water splitting devices when paired with a narrow bandgap absorber; 2) it has achieved greater than 10 mA cm^{-2} in PEC hydrogen evolution under 1 sun illumination,[6] another requirement for high-efficiency devices; and 3) it has shown impressive durability under operation in aqueous electrolyte.[6,45]

While capping layers such as CdS,[29–31,39–41] TiO_2,[33,44] AZO/TiO_2,[42] Al_2O_3/TiO_2,[43] In_2S_3,[34] ZnS,[45,46] ZnO,[36] TiO_2/MoS_2,[10] and Ti/Mo[47,48] have been applied in chalcopyrite-based photocathode devices, only CdS, ZnS, and Ti/Mo coatings have enabled greater than 24 h of illuminated hydrogen-evolving operation,[29–31,41,45] and only in near-neutral electrolyte conditions that may prove unsuitable from a device engineering perspective. Alternatively, we hypothesized that pairing a $CuGa_3Se_5$ absorber with a coating of tungsten oxide (WO_3) would yield a device that is highly durable and high-performing. WO_3 is predicted to have good chemical stability in acidic environments[49] and limited absorption of visible light (due to its indirect E_g = 2.7 eV band gap),[50] motivating the study herein.

Drawing inspiration from the development of ultrathin TiO_2 protective coatings,[51] we evaluated WO_3 coatings as a new strategy for enabling long-term durability in solar hydrogen production, with the potential for utility in other acidic-media electrocatalytic reactions. While previous workers have utilized bulk n-type WO_3 as a heterojunction partner with p-type semiconductor photocathodes without addressing the long-term operation of these devices,[50,52,53] this work explores the durability advantages of WO_3 coatings.

Properties of ultrathin WO_3 coatings: Materials were synthesized via pulsed chemical vapor deposition[54] onto $CuGa_3Se_5$ absorbers that had been co-evaporated on molybdenum-coated soda-lime glass substrates.[6] The thickness of the WO_3 coatings was 3.8 nm, as determined by spectroscopic ellipsometry of the film synthesized on a silicon wafer substrate during the same deposition. Grazing incidence x-ray diffraction (GI-XRD) measurements were unable to detect signal from the ultrathin WO_3 coatings, indicating that the as-prepared films are either not sufficiently crystalline or too thin to yield detectable diffraction patterns in this instrument. The WO_3-coated samples were then loaded with a nanoparticulate platinum as the H_2-evolving catalyst.

Both the WO_3 and Pt coatings were shown to be uniformly distributed over the entire $CuGa_3Se_5$ substrate as measured by scanning electron microscopy and energy-dispersive x-ray (SEM-EDX) elemental mapping (Figure 61). These coatings were also shown to transmit a majority of the simulated solar flux, as demonstrated by UV/Vis transmittance measurements. Previous efforts aimed at studying these coatings through cross-sectional SEM imaging have been unable to distinguish the individual ultrathin layers,[10] however sophisticated imaging techniques such as cross-sectional high-resolution transmission electron microscopy could inform future studies.

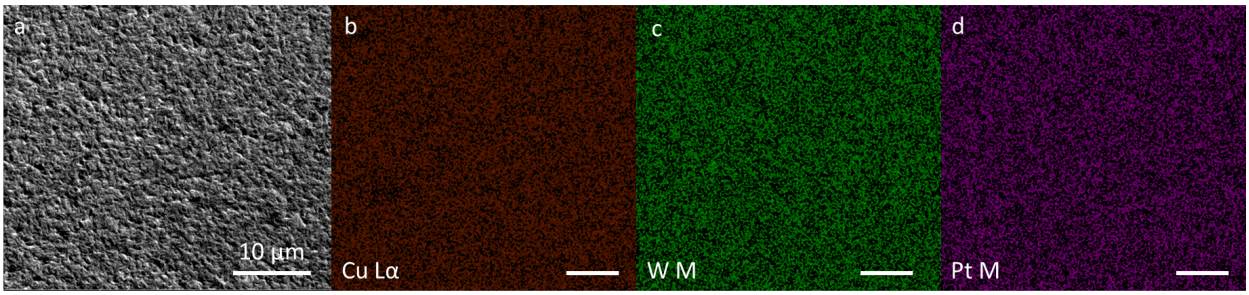

Figure 61: (a) SEM image of an as-prepared $CuGa_3Se_5|WO_3|Pt$ device and associated EDX elemental maps of the Cu Lα (b), W M (c), and Pt M (d) signals; all the scale bars are 10 µm in length.

Basic PEC characterization: The activity and durability of these photocathodes for the hydrogen evolution reaction (HER) under continuous simulated 1 Sun AM1.5G illumination were investigated via linear sweep voltammetry (LSV) and chronoamperometry (CA), respectively (Figure 62). As determined from the LSV data displayed in Figure 62a, the $CuGa_3Se_5|WO_3|Pt$ photocathode generated a saturation photocurrent density of -8.5 mA cm^{-2} and a photocurrent onset potential[10] of E = +0.32 V *vs*. RHE compared to -8.1 mA cm^{-2} and +0.30 V *vs*. RHE for the bare $CuGa_3Se_5$ photocathode. A separate $CuGa_3Se_5|Pt$ photocathode shows an improved onset potential (+0.39 V *vs.* RHE) compared to the bare $CuGa_3Se_5$ photocathode due to the improved catalysis of the Pt catalyst compared to the bare $CuGa_3Se_5$ surface. However, the $CuGa_3Se_5|WO_3|Pt$ photocathode has an onset potential 0.07 V lower than that of the $CuGa_3Se_5|Pt$ photocathode, apparently due to a suboptimal $CuGa_3Se_5|WO_3$ interface. From the idealized band energy diagrams for a $CuGa_3Se_5|WO_3|Pt$ device we might predict the possibility of achieving photovoltage exceeding of 0.5 V from an ideal $CuGa_3Se_5/WO_3$ heterojunction device.[55] The complicated effects of the Pt catalyst and WO_3 coating on the onset potential provide motivation for a quantitative investigation of the system's interfacial energetics involving multi-modal spectroscopies[56,57] that are, however, outside of the scope of the current work.

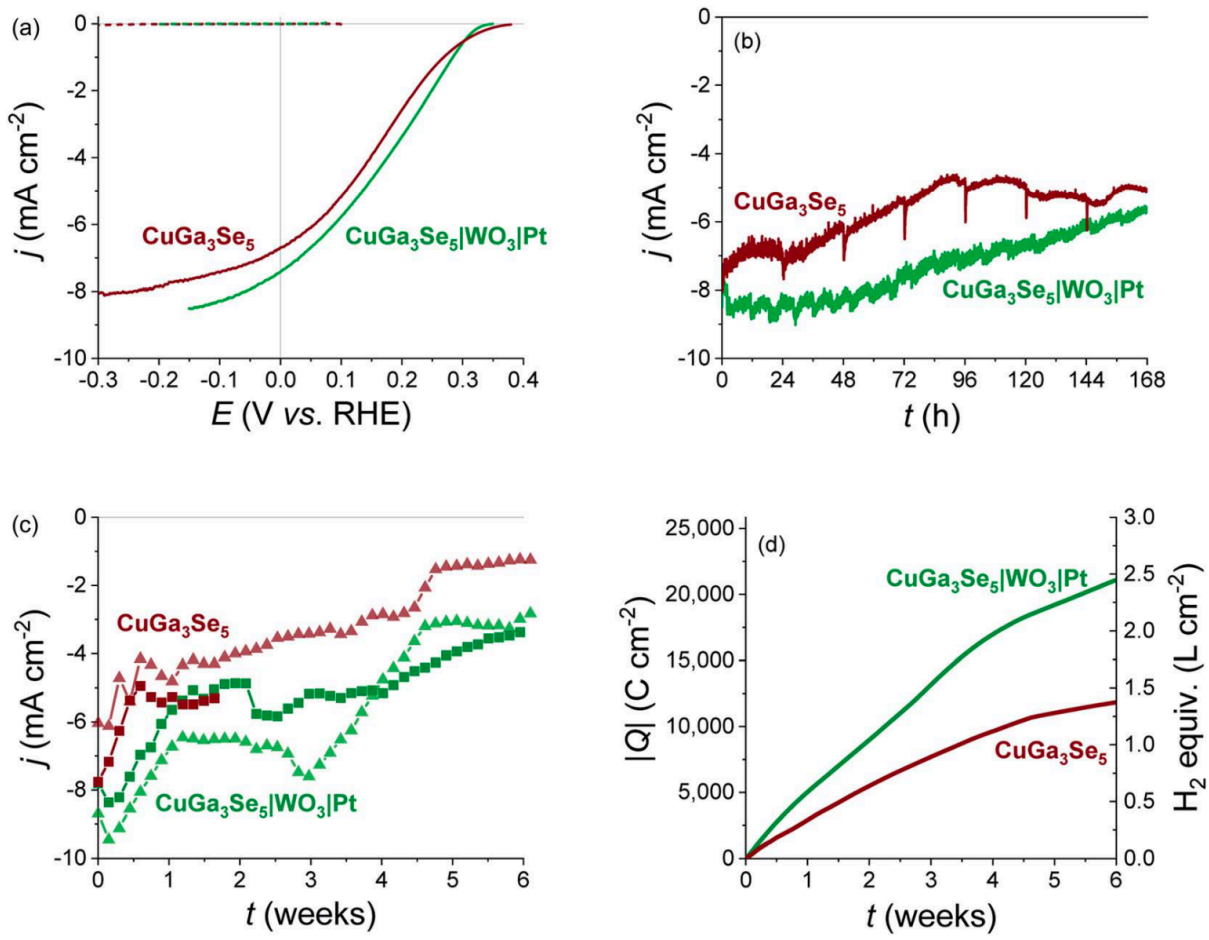

Figure 62: (a) PEC LSV of a bare $CuGa_3Se_5$ photocathode (maroon) and a $CuGa_3Se_5|WO_3|Pt$ photocathode (green); LSV with the light blanked ('dark LSV') shown in dashed lines, which track the j = 0 axis; (b) PEC CA of the same photocathodes over the first week of operation at potentials of -0.3 V vs. RHE (bare $CuGa_3Se_5$) and -0.15 V vs. RHE ($CuGa_3Se_5|WO_3|Pt$); (c) long-term CA of the same photocathodes (maroon squares and green squares) along with duplicates of each electrode type (pale maroon triangles and pale green triangles, E_{CA}=-0.2 V and -0.25 V vs. RHE, respectively)—here the lines are solely guides for the eye to connect the one daily data point shown; (d) integrated charge passed by a $CuGa_3Se_5|WO_3|Pt$ photocathode (green) and a bare $CuGa_3Se_5$ photocathode (maroon) over six weeks of CA testing, with the secondary vertical axis representing the equivalent volume of H_2 (at P =1 atm) that would be produced by this amount of charge; all experiments were performed in 0.5 M H_2SO_4 electrolyte purged with H_2 gas, utilizing a $Hg/HgSO_4$ reference electrode and an Ir/IrO_x counter electrode, with light experiments performed under continuous simulated 1 Sun AM1.5G illumination.

The photocurrent densities and onset potentials measured here are commensurate with those reported for other photocathodes employing $CuGa_3Se_5$ as absorber. In previous studies, the maximum photocurrent densities under simulated 1 Sun AM 1.5G illumination range from -5 mA cm^{-2} to -10.4 mA cm^{-2}, and the onset potentials range from +0.1 V *vs.* RHE with a bare $CuGa_3Se_5$ photocathode to +0.35 V *vs*. RHE with a Pt-catalyzed $CuGa_3Se_5$ photocathode.[6,58] With these studies for context, we will demonstrate further below that we were able to achieve milestone durability targets utilizing $CuGa_3Se_5$ photocathodes that approach state-of-the-art performance.

We aim to develop strategies for stability that can continue to be leveraged as $CuGa_3Se_5$ photocathodes approach ideality. As a single-junction device employing a 1.84 eV band gap absorber, a $CuGa_3Se_5$ photocathode can generate a theoretical maximum photocurrent density of -18.5 mA cm^{-2} under 1 Sun AM 1.5G illumination[59–61] and a theoretical photovoltage exceeding 1 V. The disparity between our photocathode activity and that of an ideal $CuGa_3Se_5$ photocathode could result from several factors, including: 1) the possibility of phase impurities in the absorber layer that could lead to recombination in the film that may limit the saturation photocurrent density, as discussed in previous work,[6] and 2) the absence of an interfacial buffer layer, *i.e.* a non-ideal junction between the $CuGa_3Se_5$ absorber and the applied overlayers that may suppress the demonstrated onset potential.

Durability testing: For chronoamperometric durability testing, each photocathode device was operated under continuous simulated 1 Sun illumination at a potential where its photocurrent density approaches its saturation value. Since this bias condition induces the maximum amount of charge to be passed through the PEC device, we note that this is a strenuous durability testing protocol, while recognizing the importance of standardizing durability testing within the solar hydrogen production community. Whereas the photocurrent density of the bare $CuGa_3Se_5$ photocathode immediately began to decrease from its initial value (-8.0 mA cm^{-2}), the $CuGa_3Se_5|WO_3|Pt$ photocathode was able to maintain its initial photocurrent density (-8.1 mA cm^{-2}) for 67 h of operation during the CA durability experiment (Figure 62b). This improved stability indicates that the $WO_3|Pt$ coating plays a substantial role in sustaining effective solar-driven hydrogen production over these initial stages of the experiment. This notion is supported by the fact that the durability of a Pt-coated $CuGa_3Se_5$ photocathode without any WO_3 coating is significantly worse than either the $CuGa_3Se_5|WO_3|Pt$ or bare $CuGa_3Se_5$ photocathode over a week of testing. Furthermore, a degenerately doped n-type Si conductive substrate coated with WO_3 and Pt ($n^+Si|WO_3|Pt$, an HER electrocatalytic analogue electrode) maintained reasonable activity over 40 h of continuous operation at -10 mA cm^{-2}, whereas a $n^+Si|Pt$ device without WO_3 coating degraded rapidly within 3 h of testing, demonstrating that the WO_3 coating also plays a role in extending durability in this case.

Ultimately, the aforementioned $CuGa_3Se_5|WO_3|Pt$ photocathode, another identically processed $CuGa_3Se_5|WO_3|Pt$ photocathode, and a bare $CuGa_3Se_5$ photocathode all sustained light-driven hydrogen evolution for over 6 weeks of continuous operation under applied bias (Figure 62c). Figure 62d compares the cumulative charge passed as a function of time for the most-durable $CuGa_3Se_5|WO_3|Pt$ device (pale green data in Figure 62c) to that of a bare $CuGa_3Se_5$ device (pale maroon data in Figure 62c); the experiments resulted in passing 21,490 C cm^{-2} and 12,590 C cm^{-2} of charge, respectively. In fact, both of the $CuGa_3Se_5|WO_3|Pt$ photocathodes surpassed the previous durability milestone (in C cm^{-2}) for any non-silicon solar hydrogen-producing device by generating 21,490 C cm^{-2} and 19,510 C cm^{-2}, respectively.[6,25] Table 2 contains a comparison of durability results calculated from literature reports of Cu chalcopyrite photocathodes, which have demonstrated the best durability of any non-silicon devices.

Table 2: Comparison of most-durable Cu chalcopyrite photocathodes

Absorber	Coating	pH	*t* (days)	*Q* (C cm^{-2})	ref.
$CuGaSe_2$	CdS	7	12	3400	Moriya, 2013
$(Ag,Cu)GaSe_2$|$CuGa_3Se_5$	CdS|Pt	7	20	12900	Zhang, 2015
$Cu(In,Ga)Se_2$	CdS|Ti|Mo|Pt	6.8	10	16300	Kumagai, 2015
$CuGa_3Se_5$	none	0.3	17	11750	Muzzillo, 2018
$CuGa_3Se_5$	none	0.3	48	12590	*this work*
$CuGa_3Se_5$	WO_3|Pt	0.3	44	21490, 19510	*this work*

Post durability materials characterization: For insight into morphological, chemical, and structural changes undergone by the device during PEC durability testing, SEM-EDX (Figure 63, Figure 64) and GI-XRD analyses were conducted on the $CuGa_3Se_5$\|WO_3\|Pt photocathode after six weeks of testing. Table 3 presents the atomic concentration of the $CuGa_3Se_5$\|WO_3\|Pt photocathodes as-prepared and after six weeks of durability testing, quantified from the EDX spectra in Figure 64. The most notable changes in composition over the course of testing are the dramatic increase in the Cu signal relative to the Ga and Se signals, the significant decrease in signal from Pt, and the absence of W signal after testing. The SEM image in Figure 63a reveals dramatic changes to the sample surface over the course of extended PEC testing, and the EDX mapping shows that in contrast to previously uniform distribution, Cu-rich regions appear in a striated pattern after testing (Figure 63b). EDX mapping of the Ga and Se signals from this same sample reveals that the Cu-poor regions are enriched in Ga and Se, and vice versa. The GI-XRD analysis indicate that the crystalline component of the $CuGa_3Se_5$ absorber layer remains largely unchanged before and after long-term operation of the $CuGa_3Se_5$ and the $CuGa_3Se_5$\|WO_3\|Pt devices, and no signal was detected from the WO_3 or Pt overlayers either before or after testing. The appearance of a new peak near $2\theta = 25°$ after testing in the $CuGa_3Se_5$\|WO_3\|Pt device is best attributed to the formation of a crystalline phase resembling Cu_3Se_2. As reported previously,[6] this feature is not present in the tested bare $CuGa_3Se_5$ device, indicating that the WO_3\|Pt coating may play a role in the stabilization or formation of this phase.

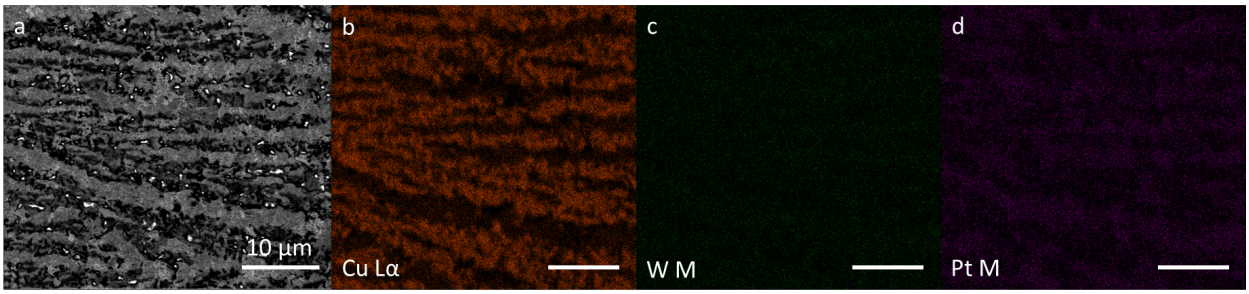

Figure 63: (a) SEM image of a $CuGa_3Se_5$\|WO_3\|Pt photocathode after six weeks of PEC durability testing, and associated EDX elemental maps of the Cu Lα (b), W M (c), and Pt M (d) signals; all the scale bars are 10 µm in length.

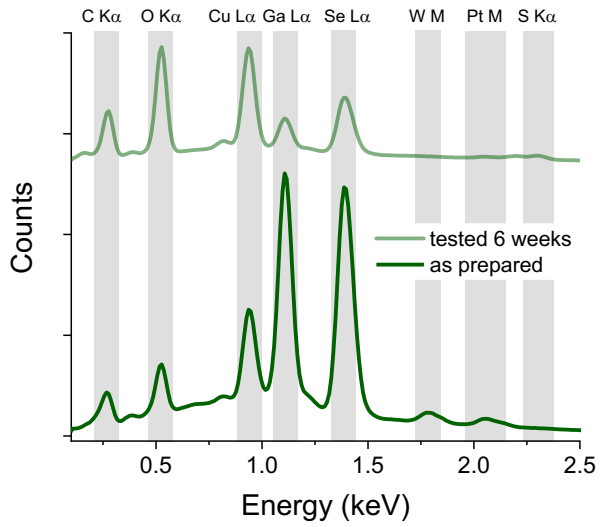

Figure 64: EDX spectra of an as-prepared $CuGa_3Se_5|WO_3|Pt$ photocathode (green) and a $CuGa_3Se_5|WO_3|Pt$ photocathode that had undergone six weeks of PEC durability testing (pale green)

Table 3: Atomic concentration quantified from EDX analysis; with an accelerating voltage of 3 keV, the interaction volume for the technique does not include the entire thickness of the $CuGa_3Se_5$ layer

Device	Sample	Cu %	Ga %	Se %	W %	Pt %
$CuGa_3Se_5|WO_3|Pt$	as prepared	12.2	36.7	48.5	0.9	1.7
$CuGa_3Se_5|WO_3|Pt$	tested 6 weeks	52.4	16.0	31.1	0	0.5

Given the evolution of the Cu:Ga:Se ratio in the absorber film and drawing on previous work demonstrating the dissolution of Cu from copper gallium selenide photocathodes in acidic media,[62] it is evident that the key contributor to diminishing photoactivity in these devices is dissolution of the constituent elements from the absorber film. The presented data lead to at least two general pathways for the degradation by dissolution: 1) the WO_3 and Pt coatings themselves dissolve over the course of extended durability testing, followed by dissolution of the exposed $CuGa_3Se_5$, and 2) the $CuGa_3Se_5$ absorber dissolves through pin holes in the WO_3 and Pt coatings, ultimately compromising the mechanical integrity of the WO_3 and Pt overlayers. We propose that the ultrathin WO_3 coating employed in this study is extending the durability of these photocathodes by decreasing the rate of dissolution of the $CuGa_3Se_5$ absorber by mitigating its exposure to the corrosive electrolyte. Future work on WO_3 coating of $CuGa_3Se_5$ absorbers will involve both optimizing the deposition and investigating the mechanical and (electro)chemical stability of the WO_3 coatings, especially given the possibility of phase change occurring in the material under the present operating conditions.[49] Given the relative increase in Cu content within the information depth probed by this EDX measurement, it is evident that the net rate of Ga and Se dissolution is greater than the net rate of Cu dissolution under the photoreductive operating conditions of the durability test. Investigating these kinetics of dissolution from photoelectrode absorbers and coatings through methods such as inductively-couple mass spectrometry is an important area of method development.[63]

Importantly, we note that most of the observed charge passed over this extended time scale is due to solar hydrogen evolution rather than parasitic processes that occur without light impetus. This point is evidenced in several ways: (i) the initial 'dark LSV' for all photocathodes shows a current response that nearly overlaps the $j = 0$ axis (Figure 62a), (ii) the current densities of the $CuGa_3Se_5|WO_3|Pt$ devices decrease by an order of magnitude (to -0.11 and -0.26 mA cm^{-2}, respectively) when the lamp is blanked at the end of the durability tests, and (iii) hydrogen bubbles were seen forming and detaching from the electrode surface for the duration of the experiment. Developing methods for collecting and quantifying hydrogen over the course of long-term durability testing is a recognized need for the solar hydrogen community.[6,26–31,64–67]

Summary: We demonstrated the utility of $CuGa_3Se_5$ absorbers coated with ultrathin WO_3 coatings for long-term operation of solar-driven hydrogen production and achieve a new durability milestone for any non-silicon photocathode device, passing 21,490 C cm^{-2} of charge over six weeks of continuously illuminated testing under applied bias. Since solar cell devices based upon $CuGa_3Se_5$ absorbers have generated open-circuit voltages exceeding 0.75 V by employing interfacial buffer layers such as CdS,[6] there is great opportunity to adapt the durability strategies developed herein to $CuGa_3Se_5$ photocathode devices that exceed the maximum +0.39 V *vs*. RHE onset potential demonstrated in this work. With the incorporation of such a buffer layer and further optimization of the WO_3 deposition process, this system has the potential to reach technologically relevant activity and durability for a wide band gap photocathode. These WO_3 coatings, in turn, have the potential to be widely applicable in extending the durability of solar-driven hydrogen-evolving systems toward meaningful technological timeframes.

c. Combinatorial development of buffer materials

Chalcopyrite photocathodes suffer from non-ideal band-edge positions with respect to the redox potentials of water-splitting, requiring interfacing the absorber with CdS as a contact material (also known as n-type 'buffer') to create the pn-junction. However, CdS layers suffer from short wavelength absorption and instability in electrolyte solution. In addition, CdS has a cliff-like ~0.2 eV conduction band (CB) offset with stoichiometric $CuGaSe_2$, and a similar CB offset is expected for $CuGa_3Se_5$.[68] If the conduction band minimum (CBM) of the contact is lower than that of the absorber (a 'cliff' type offset), the device suffers from lower photovoltage, increased interface recombination, and other detrimental effect to device performance.[69–71] If a CBM of the contact is more than 0.3 eV above that of the absorber (a 'spike' type offset), the resulting barrier impedes the collection of photo-generated carriers.[72–74]

To address these challenges, $Mg_xZn_{1-x}O$ (MZO)[75,76] with tunable conduction band position as a function of Mg content has been proposed as an attractive n-type contact layer. MZO thin film was demonstrated with up to $x = 0.46$ grown by radio-frequency (RF) co-sputtering without any phase segregation resulting in a bandgap of up to 4.2 eV, while ZnO has a bandgap of 3.24 eV.[75] Combinatorial studies explored the composition spreads of MZO with different deposition methods, such as pulsed laser deposition[77,78] and chemical vapor deposition.[79] In a previous combinatorial study, we showed that the conduction band position could be tuned by 0.5 eV as Mg concentration changes from 4 to 12%,[80] suggesting that it might be a suitable contact to $CuGa_3Se_5$ absorber. Integration of MZO as contact material resulted in significant efficiency improvements of CdTe[81] and CIGS[82,83] PV, as well as $CuGaSe_2$[84] that likely has similar CB position to $CuGa_3Se_5$.

In this program, MZO was investigated as the contact layer material for $CuGa_3Se_5$ absorber-based PV and PEC devices. Structural, optical, and electrical properties of MZO thin films were studied as a function of different experimental conditions such as Mg composition, Ga doping, substrate temperature and deposition ambient. MZO depositions were performed by combinatorial RF sputtering. For functional $CuGa_3Se_5$/MZO PV device, absorber surface pretreatment with Cd^{2+} solution was crucial because it removed surface oxidation, led to Cd incorporation, and possibly changed the surface conductivity type. MZO deposition and the surface pretreatment conditions were optimized for solid state solar cell performance. The outcome was a significant improvement in open circuit voltage (up to 920 mV) compared to conventional CdS-contact $CuGa_3Se_5$ devices (~730 mV). Replacement of CdS also improved quantum efficiency in the blue region of the spectrum. These outcomes indicate that $CuGa_3Se_5/Mg_xZn_{1-x}O$ could serve as an efficient top cell for tandem PV and PEC water splitting devices.

$Mg_xZn_{1-x}O$ thin film synthesis and characterization: Ga-doped $Mg_xZn_{1-x}O$ thin film sample libraries with orthogonal composition gradients of Mg and Ga were deposited by combinatorial RF magnetron sputtering from ZnO, Mg and Ga_2O_3 targets (Figure 65a). For $CuGa_3Se_5$ device integration, combinatorial RF sputtered $Mg_xZn_{1-x}O$ was deposited with x values in the 0 to 0.15 range, and Ga/(Ga+Zn) atomic ratio from 0% to 15%. Figure 1b shows the composition profile of one such Ga:$Mg_xZn_{1-x}O$ library. XRD patterns of the MZO films were all (0002) oriented wurtzite ZnO; no peaks related to MgO or Ga_2O_3 secondary phases were observed for the investigated span of Mg and Ga compositions (Figure 66). With increasing Mg composition, the ZnO (0002) peak broadened, intensity reduced and shifted towards lower angles. This shift was more significant at higher Ga/(Ga+Zn) samples. Mg atomic size is much lower than Zn or Ga. Mg incorporation at large degree could induce strain in the ZnO crystal, indicated by the peak broadening at high Mg samples.

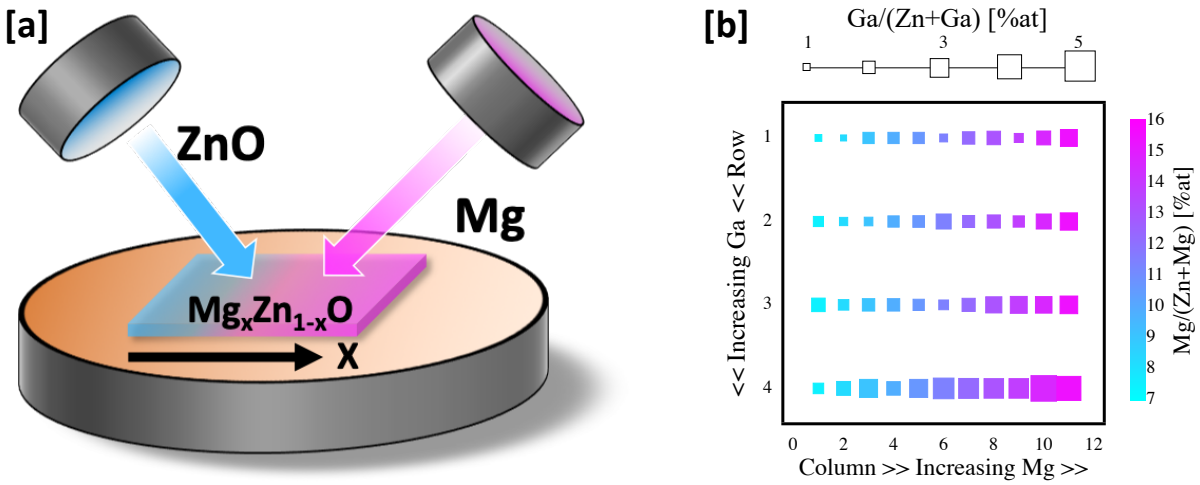

Figure 65. (a) Combinatorial sputter deposition of $Mg_xZn_{1-x}O$ thin films. (b) 4x11 composition measurement grid for Ga:$Mg_xZn_{1-x}O$ films on a 50mm × 50mm glass substrate.

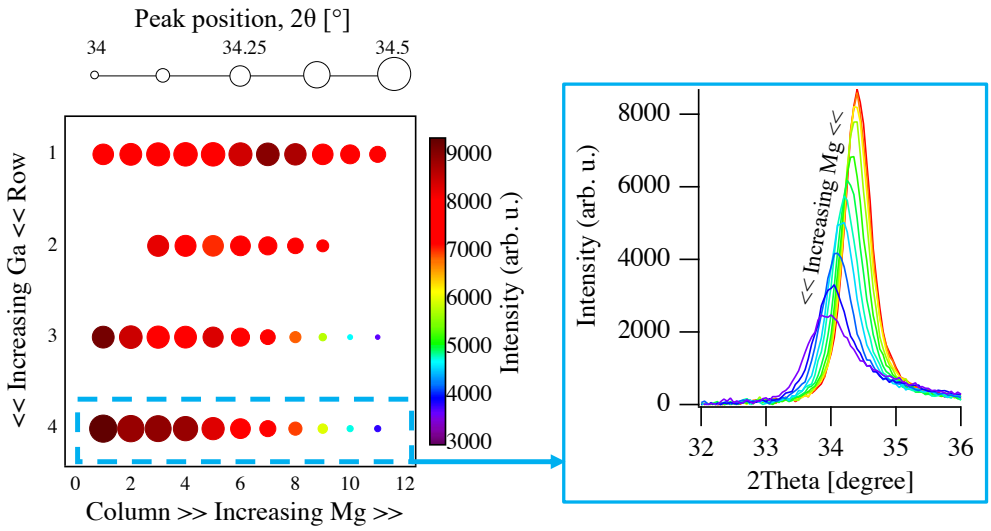

Figure 66. ZnO (0002) peak position and intensity for a Ga:$Mg_xZn_{1-x}O$ sample library deposited at 200°C.

The film conductivity for the undoped MZO films deposited at 100°C or below were too low to be measured. The conductivity for the doped MZO films were dependent on Ga and Mg compositions (Figure 67a). Conductivity decreased with increasing Mg composition, possibly due to wider bandgap and increased carrier scattering. Introduction of Ga as dopant increased conductivity, and then decreased it at higher Ga concentrations when Ga/(Ga+Zn) atomic ratio exceeded 5%. This was likely due to the reduced crystallinity of those samples, as evident from the XRD data. The highest conductivity was 20 S/cm and was observed at Ga/(Ga+Zn) value of 4%. Mg incorporation also resulted in the expected bandgap widening. Increasing Mg composition increased the optical bandgap of MZO, calculated from the Tauc plot of the absorption data from UV-Vis spectroscopy (Figure 67b). For the highest experimented Mg composition of 13%, optical band gap values up to 3.57 eV was estimated.

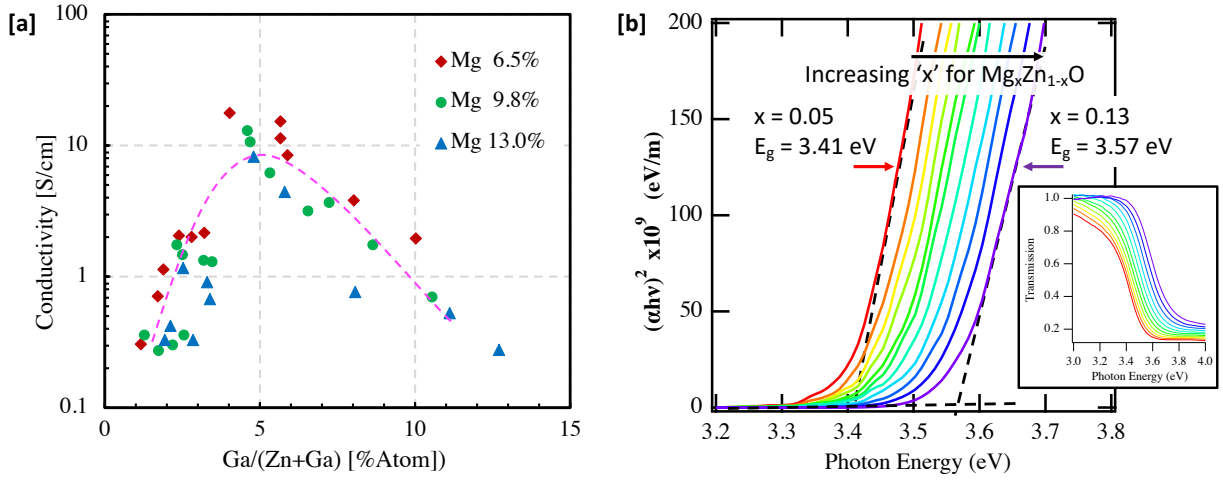

Figure 67. (a) Conductivity vs. Ga/(Ga+Zn) atomic ratio for $Mg_xZn_{1-x}O$:Ga thin films deposited at 200°C. (b) Tauc plot from the transmittance data showing the shift in the estimated optical bandgap for undoped MZO films with increasing Mg composition.

Photovoltaic characterization: $Mg_xZn_{1-x}O$ with varying composition was integrated with $CuGa_3Se_5$ absorbers into solid state test structures with top TCO and metal contacts. For the baseline PV device ($CuGa_3Se_5$/CdS/i-ZnO material stack), the open circuit voltage (V_{OC}) = 730 mV, short-circuit current (J_{SC}) = 5.7 mA/cm^2, fill factor (FF) = 61%, and efficiency 2.6% were achieved. Initial devices with CdS contact layer, and MZO layer replacing i-ZnO layer showed promising results: V_{OC} = 755 mV, J_{SC} = 7.6 mA/cm^2, FF = 38.4%, and efficiency 2.1%. A clear CdS layer was observed in SEM (Figure 68a), STEM/HAADF (Figure 68c) and STEM/EDX (Figure 68e) images.

$Mg_xZn_{1-x}O$ was then studied as a replacement for the CdS/i-ZnO contact stack. PV devices without any surface treatment of the as-deposited $CuGa_3Se_5$ didn't exhibit any quantifiable current generation. Solution treatments of $CuGa_3Se_5$ indicated a pathway to replace CdS with MZO, with MZO grown directly on NH_4OH-treated and Cd^{2+} solution treated $CuGa_3Se_5$ surfaces. The NH_4OH treatment of the absorber prior to MZO deposition resulted in some photovoltaic activity, although the device performance values were quite low. Cd^{2+} solution treated $CuGa_3Se_5$ surfaces led to improved PV performance, and some incorporation of Cd into $CuGa_3Se_5$ surfaces.

The material stack for the PV devices with Cd-treated $CuGa_3Se_5$ absorbers and MZO contacts are shown in Figure 68. The effect of the Cd^{2+} solution treatment could not be resolved from the SEM (Figure 68b) or STEM/HAADF (Figure 68d) images, indicating that very small amount of Cd was substituted at the surface. However, STEM/EDX elemental map of the device revealed Cd present at the $CuGa_3Se_5$/MZO interface (Figure 68f). A small amount of Sulphur (S) is also present at this interface, which is likely due to $CdSO_4$ that was the source of Cd^{2+}.

The device performances were dependent on the temperature and the duration of the Cd^{2+} treatment (Figure 69). Lower treatment temperature (65°C, 15 min) improved the V_{OC} up to 925 mV, while higher temperature (85°C, 7 min) treatment resulted in higher J_{SC} up to 8.3 mA/cm^2 (Figure 69c). Cd^{2+} treatment at 85°C could deposit a thicker Cd containing layer, and/or cause the inversion of surface conductivity to n-type. The J_{SC} enhancement due to improved carrier collection at longer wavelengths (QE data, Figure 69b) indicating longer depletion width supports this. This inversion layer could form a barrier at the (Cd^{2+})/$Mg_xZn_{1-x}O$/Al:ZnO junction to reduce the V_{OC}. The highest open circuit voltage of 925 mV was observed for Mg composition of x = 10.8% in $Mg_xZn_{1-x}O$ (Figure 69a). Comparing QE of different device configurations (Figure 69b) showed that replacing CdS with $Mg_xZn_{1-x}O$ improved the carrier collection in the short wavelengths due to the higher bandgap of MZO. As shown previously, the conductivity of $Mg_xZn_{1-x}O$ could be improved by doping with Ga, which required higher substrate temperature. However, device performance was significantly reduced with V_{OC} in the range of 400 to 500 mV and many devices with doped MZO were shunted (data not shown), possibly due to the higher temperature exposure.

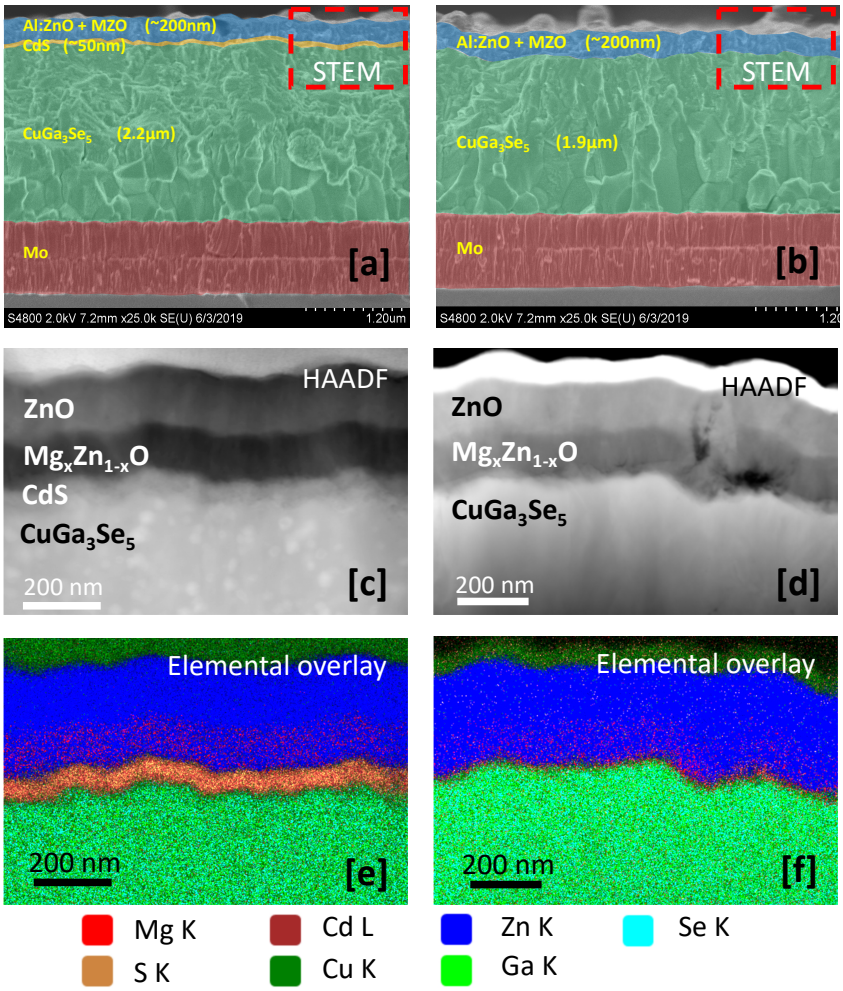

Figure 68. (a, b) SEM images with color overlay for the PV devices. (c, d) STEM HAADF images and (e, f) STEM EDX elemental maps at the $CuGa_3Se_5$/MZO interfaces. $CuGa_3Se_5$/MZO PV device with CdS (a, c, e), and Cd^{2+} solution treatment (b, d, f).

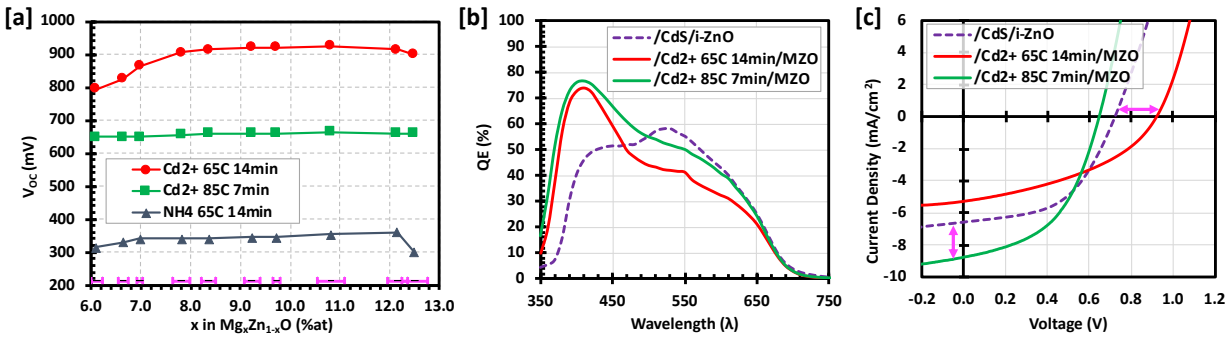

Figure 69. PV performance for CdS-free $CuGa_3Se_5/Mg_xZn_{1-x}O$ devices with different surface treatments, including (a) open circuit voltage, (b) external quantum efficiency, and (c) current voltage characteristics. The magenta bars at the bottom axis of panel (a) represent standard errors in each Mg composition.

The photovoltaic device performance for various configurations are summarized in Table 4. Although significant open-circuit voltage improvement was observed in MZO based devices, the fill factor and photocurrent output were reduced. The $CuGa_3Se_5/(Cd^{2+})$/MZO photovoltaic devices had superior open-circuit voltage of 925 mV compared to 730 – 755 mV for CdS based devices, likely due to the combined effect of favorable conduction band offset and surface passivation by Cd^{2+} treatment. Besides, the thin Cd containing layer on the $CuGa_3Se_5$ surface could have a protective effect against bombardment of the sputtering ions on the absorber during MZO growth. Looking at the complete device structure, $CuGa_3Se_5/(Cd^{2+})/Mg_xZn_{1-x}O$/Al:ZnO/metal grid, the n-type counterpart for the p-type $CuGa_3Se_5$ absorber in this case is likely $Mg_xZn_{1-x}O$/Al:ZnO bilayer. Change of absorber surface conductivity type to either intrinsic or slightly n-type could create a better p-i-n junction that improved the device V_{OC}, where bulk of the $CuGa_3Se_5$ absorber is the p-type layer, the $Mg_xZn_{1-x}O$/Al:ZnO is the n-type bilayer stack, and the Cd^{2+}-treated $CuGa_3Se_5$ surface is the intrinsic (i) layer.

$Mg_xZn_{1-x}O$ contacted $CuGa_3Se_5$ absorber PV device data fulfilled two important requirements for top cell tandem device application: high V_{OC} and improved QE in the blue region of the spectrum. Although direct water splitting tests were not performed yet due to the instability of MZO in acidic solutions, LSV testing in sacrificial redox couple showed promising outcomes (data not shown). A thin protective layer deposited on top of MZO could improve stability and facilitate water splitting experiments, like demonstrated for bare CGS surfaces.[85] More experiments are in progress to integrate such protective coatings on MZO without degrading underlying absorber/contact interface, and will be reported in the future.

Table 4. Photovoltaic device performance for different configurations

Device Configuration	V_{OC} (mV)	J_{SC} (mA/cm^2)	FF (%)	Efficiency (%)
CGS/CdS/i-ZnO	730	5.7	61.4	2.6
CGS/CdS/MZO	755	7.6	38.4	2.1
CGS/Cd^{2+} 65°C 14min/MZO	925	4.8	41.9	1.9
CGS/Cd^{2+} 85°C 7min/MZO	650	8.3	47.6	2.6

Summary: $Mg_xZn_{1-x}O$ contact integration with $CuGa_3Se_5$ absorber was demonstrated. MZO deposition and absorber surface treatment parameters are determined for improved photovoltaic device performance, which allowed the elimination of the CdS contact layer. Characterization of the $CuGa_3Se_5$ films with Cd^{2+} solution surface treatment indicated that the beneficial effect of the treatment is due to removal of surface oxidation and change in surface doping by Cd substitution. Replacing CdS/i-ZnO with MZO improved the carrier collection in the short wavelengths and resulted in open circuit voltage of 925 mV, which is promising for top-cell tandem PV device applications. The results of this research will facilitate the understanding of $CuGa_3Se_5/Mg_xZn_{1-x}O$ interface, and the use of $CuGa_3Se_5$ absorbers for both PEC and PV device applications.

5. Achievements in Task 3 "Hybrid Photoelectrode Device Integration"

Monolithic integration, the process by which solid-state devices are made by sequentially depositing layers of materials on top of each other, is used in all commercial thin film-based technology. This process is so foundational nowadays that it is difficult to imagine any other way to create high-efficiency solid-state devices. In the context of PV, monolithically-integrated multi-junction (MJ) cells have demonstrated their capability in overcoming the thermodynamic efficiency limits of single-junction (SJ) devices, as well as being a practical solution to create PEC devices for direct solar-to-hydrogen conversion. Despite its wide acceptance, however, monolithic integration presents major limitations in process compatibility, restricting materials selection and synthesis to a sub-set of compatible systems while limiting the adoption of emerging candidates.

The few attempts reported on MJ chalcopyrite devices have exposed key limitations of the class for monolithic integration, primarily the rapid degradation of underlying materials and junctions. For example, exposing a $Cu(In,Ga)Se_2$ cell to temperatures above 300°C for only 10 minutes reduces its efficiency by over 50%.[86] At these temperatures, elements such as Cd and Zn from the buffer and window layer easily diffuse throughout the entire device, thereby deteriorating the metallurgical junction.[12] As such, the record efficiency for monolithic whole-$Cu(In,Ga)Se_2$ tandems remain modest (e.g., 4.3%). Sub-cells grown on transparent conductive substrates that can be mechanically stacked and wired in series has been proposed as a MJ architecture to circumvent temperature incompatibility. Whole-chalcopyrite mechanically stacked tandems with efficiencies reaching beyond that of monolithic chalcopyrite tandems have been reported (8.5%),[87] however significant optical and electrical losses from transparent conductive oxide layers combined with electrical circuit complexity prevent adoption of this technology outside research laboratories.

In this task, we examine the development of a robust tandem integration process that permits direct successive integration of unmodified SJ thin-film technology into MJ devices without compromise in material and fabrication methods. Our strategy, further referred to as *semi-monolithic* integration, relies on the bonding and exfoliation of independently processed, substrate-grown SJ devices to create a whole thin film-based MJ device. By design, this scheme allows successive integration of thermally, chemically and/or mechanically incompatible material classes onto a single substrate without compromising state-of-the art SJ fabrication processes.

Our semi-monolithic approach relies on to key processes: i) bonding of fully processed chalcopyrite devices onto a handle using a transparent conductive composite (TCC) and ii) delamination of the bonded stack at the $Cu(In,Ga)Se_2$/Mo interface which is permitted by the weak out of plane van-der Waals forces in the $MoSe_2$ layer which naturally forms during chalcopyrite integration on Mo substrates. We present in the following sections our efforts to develop TCC layers, establish a reliable exfoliation process and integrate chalcopyrite absorbers into fully functional PV and PEC tandem devices.

a. Development of transparent conductive composites (TCC)

Our team at UH has developed a new composite integrating multi-functionalities such as *lightweight*, *flexibility* and *tunable optoelectronics*. Unlike most conductive flexible polymers, where media are coated on top providing only *in-plane* conductivity, our transparent conductive composites (TCC) innovate by allowing simultaneous high optical transparency and high *out-of-plane* electrical conductivity. This unique characteristic is permitted by highly conductive 50 micron Ag-coated PMMA spheres protruding out of a transparent non-conductive polymer (Figure 70a and b). TCCs are formed by pressing a sphere/polymer mix between two substrates. Depending on the surface treatment pre-applied to the substrates, TCCs can be either i) fully liberated to create free-standing films (Figure 70b and c), ii) remain bonded to only one substrate or iii) permanently bonded to both substrates. By design, the final thickness of TCC is determined by the diameter of the Ag-coated PMMA spheres.

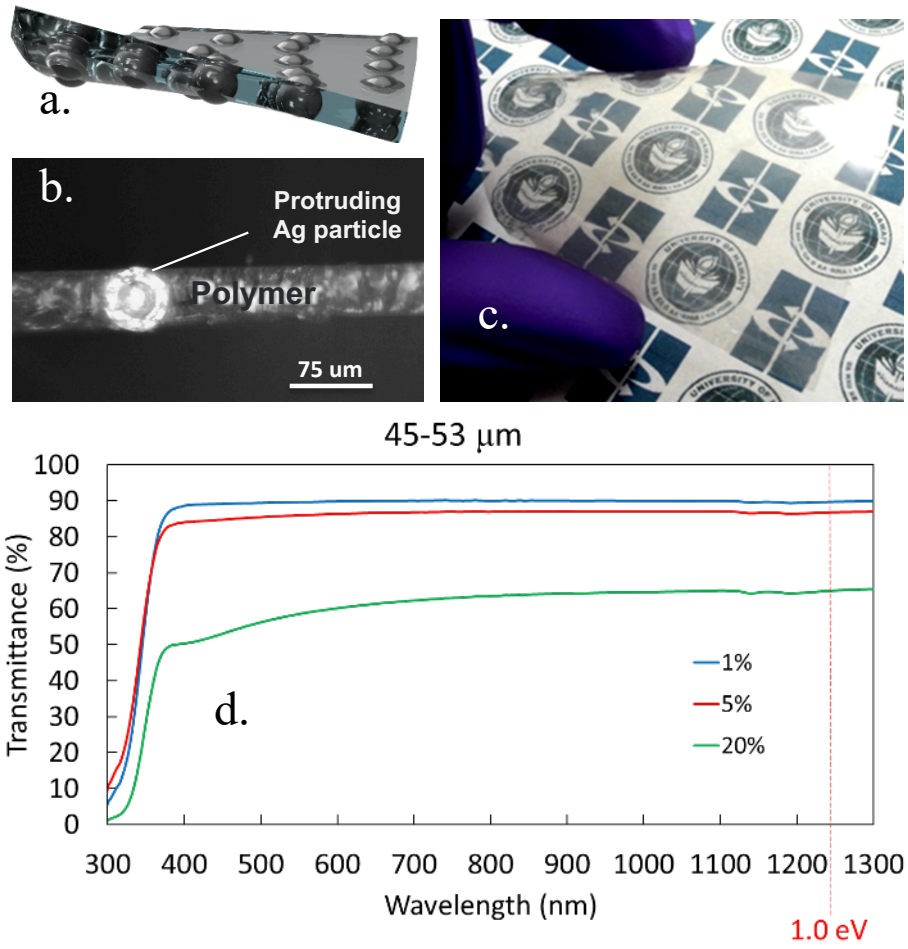

Figure 70. (a) Concept image, (b) cross-sectional microscopic and (c) photographic views of a TCC made of 50 micron Ag-coated PMMA spheres protruding out of a flexible polymer. (d) Transmittance measurements of freestanding TCCs with 1%, 5% and 20% concentrations of 45-53 µm Ag-PMMA. The dashed red line indicates 1.0 eV (1240 nm).

One of the benefits of the freestanding configuration was the ability to measure the true series *out-of-plane* resistance as well as optical transmittance of the TCC. Producing a freestanding TCC was easily achieved due to the polymer selected, a two-part epoxy. Since epoxy does not adhere to plastics, sheets of polypropylene were used as barriers to mold the TCC between two flat surfaces until cured. Then the freestanding TCC was peeled away from the polypropylene sheets yielding a freestanding artifact as seen in Figure 70c. A transparent two-part epoxy provided the optical transparency, as well as the adhesion required for bonding the thin films together. The electrically conductive particles used in the TCC were silver-coated poly methyl methacrylate spheres (Ag-PMMA) with a diameter of 45-53 μm. The flexibility of the PMMA allows the microspheres to make contact to rough surfaces.

Varied concentrations of microspheres (1%, 5% and 20%) produced TCCs with different transmittance as a percentage of the area normal to the light source. Transmittance measurements performed on 1%, 5% and 20% TCCs are plotted in Figure 70d with a dashed line indicating 1.0 eV. As expected, the transmittance decreased with an increase in microsphere concentration. The high transmittance value of the 1% TCC is evidence that the transparent epoxy is indeed highly transmissive. As expected, the decrease in transmittance from 90% to 85% was observed as the microsphere concentration increase from 1% to 5%.

Fully bonded 5% TCCs were applied to silver-coated SLG substrates to assess the *out-of-plane* conductive of TCCs. Resistance measurements were performed with a linear sweep voltammetry technique and yielded identical results for the fully bonded and freestanding TCC, i.e., 0.17 $\Omega \cdot cm^2$. We also measured the series resistance of a freestanding TCC in the same configuration except bare PMMA microspheres were substituted for the Ag-PMMA microspheres: the series resistance increased to $4.11 \cdot 10^4$ $\Omega \cdot cm^2$, confirming that current is traveling along the silver coating of the microspheres in TCCs.

Then, we employed AFM to measure the topography over a 45-53 μm Ag-PMMA microsphere in a TCC semi-bonded to FTO-coated SLG. The topography supports the claim that the electrical conductance of the TCCs is a result of microspheres protruding through the epoxy and contacting adjacent surfaces (Figure 71a). Furthermore, conductive AFM (C-AFM) measured current through the exact same TCC area where the microsphere protrudes (Figure 71b). The topography and conductance scans evaluated along the red and green lines in Figure 71a and b and presented in Figure 71c, demonstrating again that the microspheres are protruding through the exposed side of the semi-bonded TCC and the microsphere is electrically conductive in that same region.

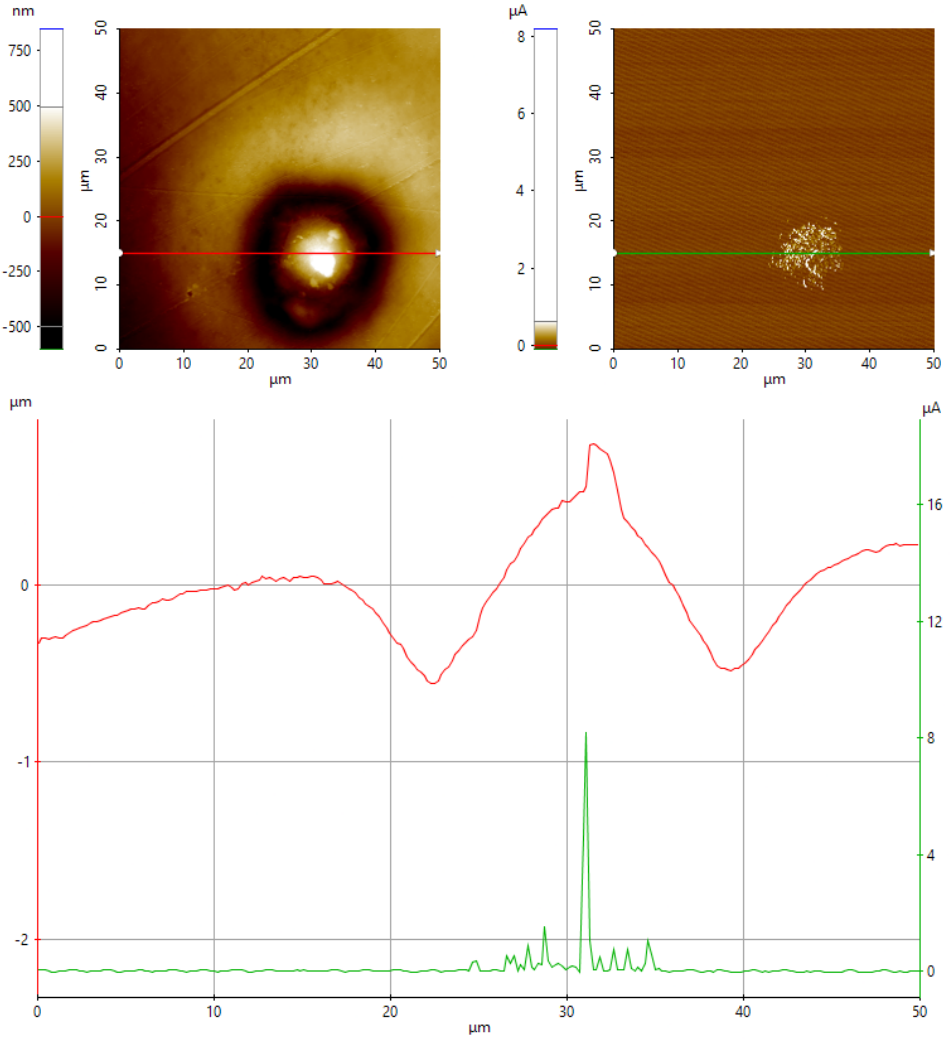

Figure 71. (a) AFM and (b) C-AFM measurements taken over a silver-coated microsphere protruding out of the epoxy layer. (c) Topography (red) and conductance (green) lines measured across the surface of a TCC.

b. Development of Semi-Monolithic Solid-State Devices

Mechanical exfoliation and characterization of $CuGa_3Se_5$ top cell: The top cell bond-and-transfer procedure is a key component in the semi-monolithic manufacturing process. Instances of rudimentary CIGSe exfoliations of small areas (< 10 × 10 mm^2) have been used as a means to access the rear of CIGSe films in order to analyze their chemical composition and electronic structure by photoelectron spectroscopy,[88] or to allow the deposition of metal contacts (other than Mo) to modify back interface energetics.[89] Also, fully processed $Cu(In,Ga)Se_2$ cells have been successfully transferred from conventional Mo/SLG substrate to both rigid and flexible substrates, however reduction in PCE by no less than 30% was reported after exfoliation and due for the most part from both high series (R_S) resistance and reduced shunt (R_{SH}) resistance from crack formation.[90] In contrast, our proposed technique allows to exfoliate chalcopyrite layers as large as 25 × 25 mm^2 while maintaining virtually 100% of the solar cell's solid-state properties, providing a viable avenue to develop MJ architectures as we demonstrate further in this communication.

First, a fully processed un-patterned CGSe PV stack (ZnO:Al (AZO)/i-ZnO/CdS/$CuGa_3Se_5$-/Mo/SLG) was bonded (face down) to a rigid FTO glass substrate at the AZO front contact using a TCC comprising Ag-coated PMMA spheres embedded in a polyepoxy matrix. Using an in-house built mechanical exfoliation device (Figure 72a), a razor blade cutting edge was inserted between the FTO and SLG substrates until separation of the AZO/i-ZnO/CdS/$CuGa_3Se_5$ PV stack from its original Mo/SLG substrate (Figure 72b), thereby transferring it onto the host FTO substrate (Figure 73).

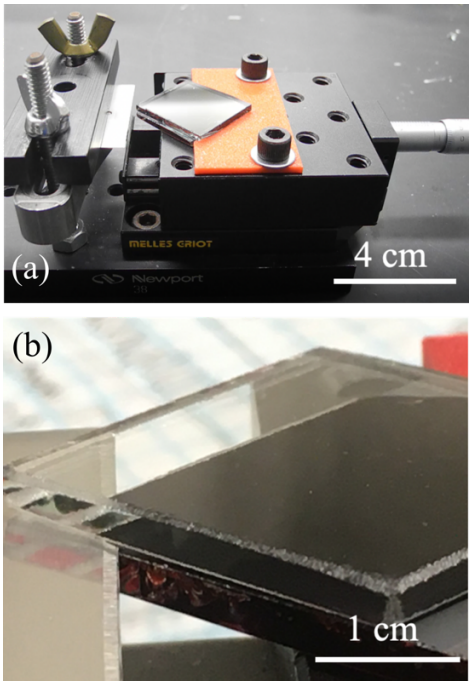

Figure 72. (a) Mechanical exfoliation device. (b) A demonstration of stack exfoliation and transfer (blade insertion depth exaggerated for visualization).

Figure 73b shows an optical image of an exfoliated 25 × 25 mm^2 CGSe PV stack transferred onto a FTO substrate. The exfoliated rear surface of CGSe appears smooth and virtually free of pinholes, aside from few point-defects originating from collapsed microspheres and/or air bubbles. Cross-sectional scanning electron microscopy (SEM) micrograph of the exfoliated PV stack (Figure 73c) shows a microsphere physically contacting both the CGSe film and FTO substrate. Raman spectroscopy analysis was performed on the top surface of CGSe as well as on both the back side of the exfoliated CGSe and top of the separated Mo substrate (Figure 74a). The spectrum measured on CGSe top surface shows peaks known for $CuGa_3Se_5$ OVC, however the rear surface of the exfoliated CGSe shows both OVC and chalcopyrite ($CuInGaSe_2$), indicating unintentional composition grading in the film. More importantly, Raman spectroscopy revealed $MoSe_2$ only on the Mo substrate and not on the rear surface of the CGSe exfoliated cell, demonstrating that $MoSe_2$ layers remained predominantly on the substrate upon exfoliation, leaving a clean CGSe surface for subsequent junction formation. This point is further demonstrated from SEM micrographs of the exfoliated CGSe back surface and top surface of the separated Mo substrate in Figure 74b and c,

showing no signs of residual material left on either film after exfoliation. Moreover, energy dispersive spectroscopy (EDS) measurements indicated no Mo being present at the CGSe back exfoliated surface (see tabulated data in Figure 74b and c). Other reports also indicated no traces of Mo on the rear surface of exfoliated chalcopyrite films, with adhesion/peeling of the absorber material from the original substrate having crucial dependence on $MoSe_2$ layer orientation. We note that some Ga (2.3%) was detected on the $MoSe_2$/Mo substrate. This finding can be explained either by diffusion of Ga into the $MoSe_2$/Mo substrate ($MoSe_2$:Ga) or the formation of Ga_mSe_x between CIGSe and $MoSe_2$.[91]

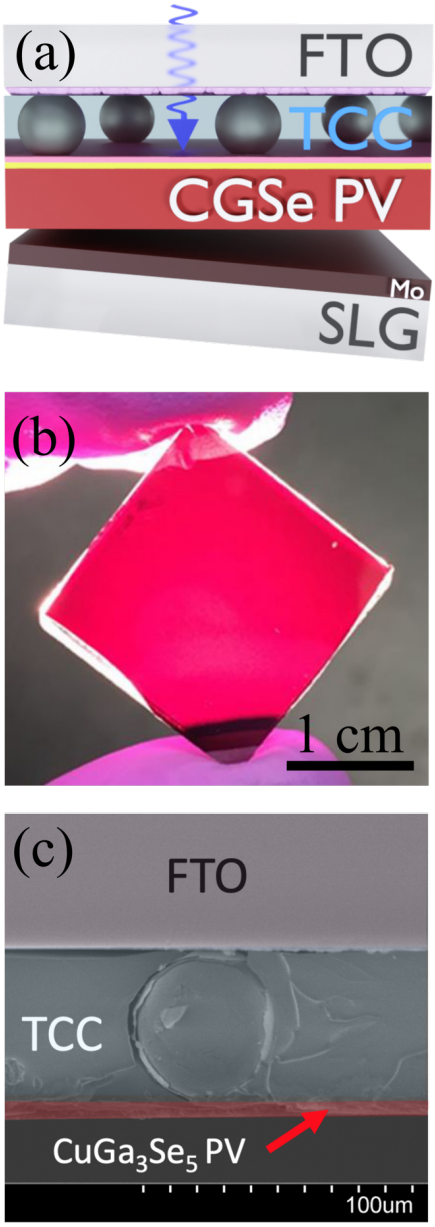

Figure 73. (a) Schematic, (b) optical image and (c) colored cross-sectional scanning electron microscopy micrograph of a CGSe PV exfoliated from its Mo substrate and transferred onto FTO using a TCC layer.

Performance verification of the CGSe post-exfoliation is an important benchmark in identifying the suitability of this method for MJ integration. To gather statistical information of device quality across the exfoliated layer, two samples comprising fully processed un-patterned CGSe PV stacks (25×25 mm^2) were prepared, exfoliated, and transferred onto two individual FTO substrates using TCC containing 15±5% conductive microsphere concentration by area. For back contact formation, metals such as Mo would be typically used due to their ideal energetics with chalcopyrites, however for the purpose of this work on MJ devices, a reflective back contact could not be used for the top cell and as such, room temperature sputtered degenerate n^+-type ITO (sheet resistance of 77.1 Ω/sq.) was used as ohmic contact with CGSe and sputtered through a shadow mask onto the two 25×25 mm^2 CGSe PV stacks previously exfoliated and transferred on FTO, leading to a total of 27 PV devices of area 0.12 cm^2 with following final structure: FTO/TCC/AZO/i-ZnO/CdS/$CuGa_3Se_5$/ITO. Figure 75 shows the V_{OC}, J_{SC}, FF and PCE statistical boxplots of the 27 devices formed on the exfoliated PV stacks, alongside the reference measurements from 4 representative baseline devices integrated with Al/Ni grids. The device performance across the exfoliated layer area show reasonable homogeneity and reproducibility. The mean V_{OC}, J_{SC}, FF and PCE were 647 mV, 5.69 mA/cm^2, 44.1%, and 1.6 %, corresponding to 91%, 91%, 76% and 64% that of the mean baseline, respectively.

It is worth noting that the PCE reduction stem primarily from lower FF, a parameter known to be impacted by series resistance (R_S) and/or shunt resistance (R_{SH}). Beside two outliers, R_{SH} remains virtually unchanged after exfoliation (avg. R_{SH} =857.8 Ω-cm^2) compared to the baseline (avg. R_{SH} =975.4 Ω-cm^2), demonstrating that the exfoliation process does not lead to significant microstructural defect formation, such as pinholes or cracks. In contrast, a 3-fold increase in R_S was measured after exfoliation. The R_S increase is associated with the size distribution of the microsphere (90% of which with diameter withing the 45-53µm in range) embedded in TCC, since not all microspheres will contact both the FTO substrate and the AZO layer. Transfer of this technology to larger scale modules will need further control of the TCC coating process, particularly the applied pressure and temperature during assembly. Detailed models of the microsphere mechanical behavior (e.g., deformation), distribution in the polymer matrix and electrical contact across the TCO layers are being conducted by our team and will be reported soon.

Instances of champion devices using samples from a high-quality batch with TCC having 3% microsphere loading demonstrates that chalcopyrite cells can undergo the exfoliation process and transparent back contact incorporation without degradation in performance. The exfoliated CGSe champion device (0.12 cm^2) exhibits a near coincident JV curve (Figure 76) with the corresponding baseline cell with Ni/Al grid (0.42 cm^2). The illumination losses through both FTO and TCC with 3% loading appear comparable to that with Al grid (~6.5% area coverage), while the baseline CGSe cell without Al grid (0.13 cm^2) exhibited slightly higher J_{SC}. The exfoliated champion device displayed a V_{OC}, J_{SC}, and PCE of 712.8 mV, 8.68 mA/cm^2, and 3.13%, corresponding to 95.3%, 95.5%, and 93.7% that of the none-grid baseline cell, respectively.

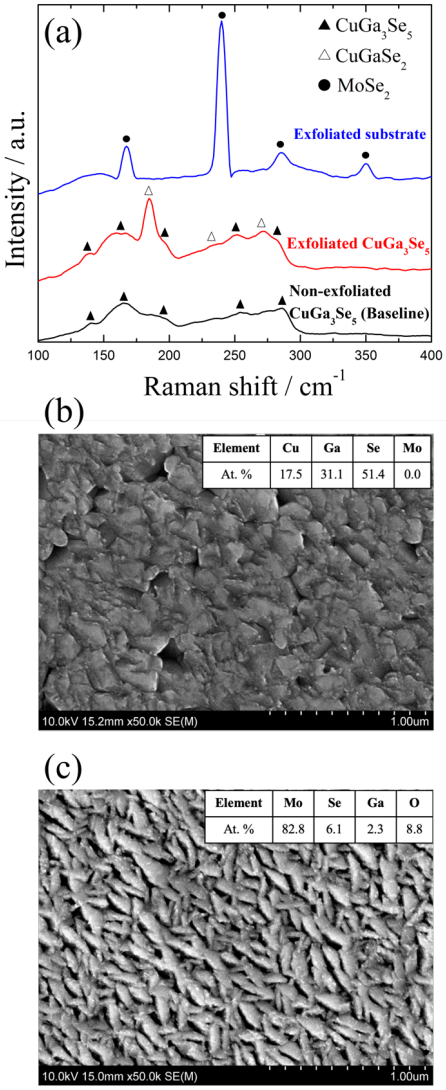

Figure 74: (a) Raman spectroscopy measurement of a bare $CuGa_3Se_5$ top layer (black), the exfoliated CuGa3Se5 rear surface (red), and the separated Mo substrate surface (blue). SEM micrographs of (b) the exfoliated $CuGa_3Se_5$ rear surface and (c) the front of the separated Mo substrate with tabulated EDS measurements.

Electrical characterization of semi-monolithic tandem device: A CGSe SJ top PV stack exfoliated/transferred onto a FTO substrate and coated with a full layer of room temperature sputtered ITO (200nm, 184 Ω/sq.) at the back interface served as the new host onto which a second fully processed narrow-bandgap CIGSe bottom cell was bonded (face down) using a second TCC layer (microsphere loading: also ~3%). The CIGSe cell was then liberated from its Mo/SLG using the same wedge technique as employed for the top cell, leading to a complete transfer of both sub-cells onto the same FTO substrate (Figure 77a and b). A 200nm thick Mo layer (sheet resistance of 2.26 Ω/sq.) was sputtered at room temperature as the CIGSe rear contact after exfoliation of the Mo/SLG substrate, with final tandem architecture of FTO/TCC/Al:ZnO/i-ZnO/CdS/$CuGa_3Se_5$/ITO/TCC/Al:ZnO/i-ZnO/CdS/$CuInGaSe_2$/Mo.

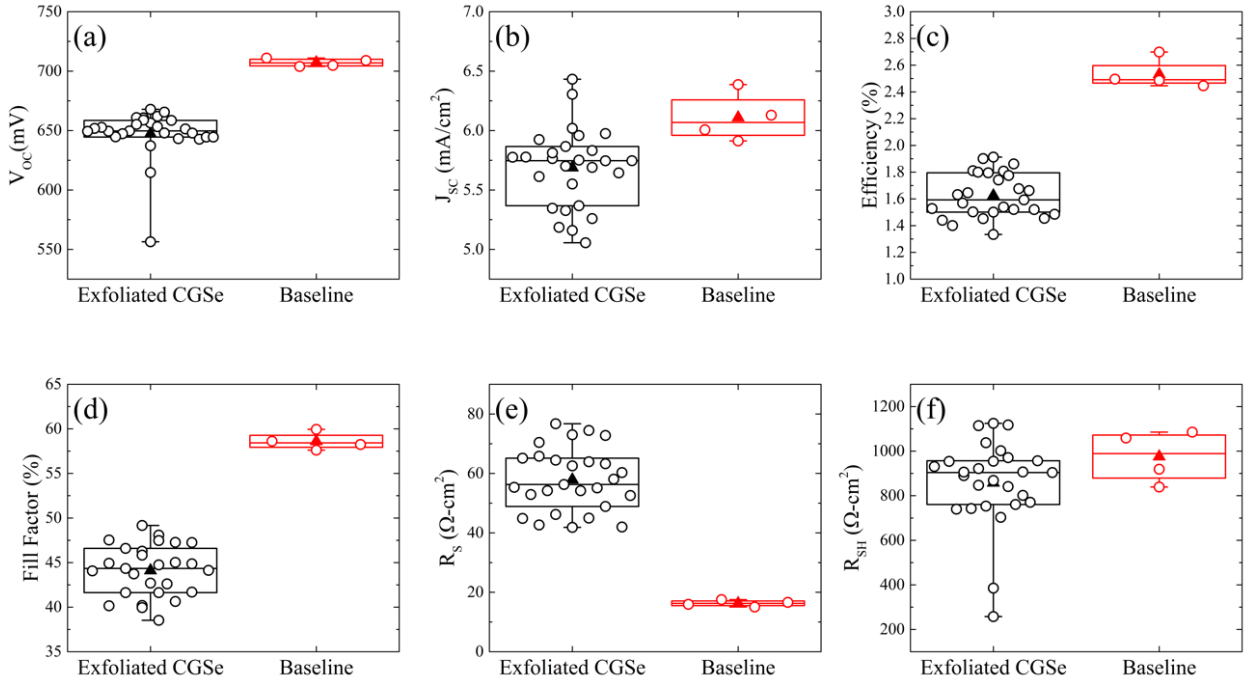

Figure 75: Performances of 27 devices of dimensions 0.12 cm2 isolated measured across two 25 × 25 mm2 exfoliated CGSe PV stack (without Al/Ni grids) and compared to 4 baseline reference cells (with Al/Ni grids).

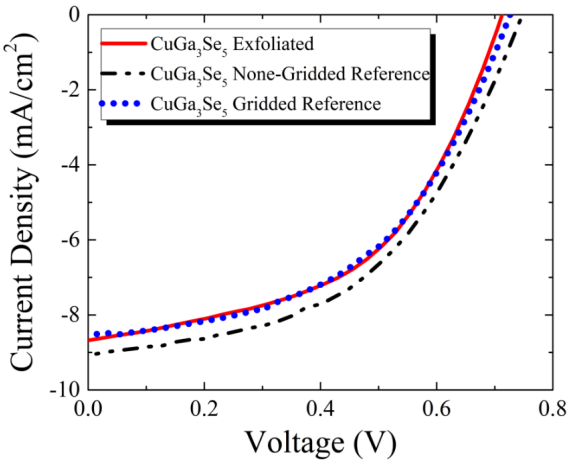

Figure 76: Highest efficiency JV measurements for baseline none-grid cell (black), baseline cell with Ni/Al grid (blue) and exfoliated cell (red).

The external quantum efficiency independently measured on the top CGSe cell and bottom CIGSe cell optically-shaded by the CGSe PV stack are presented in Figure 77c. Both showed complementary absorption range, exhibiting approximately 50% quantum efficiency in a wide range of wavelength value (400-600nm for CGSe, 750-1000nm for CIGSe), although a slight imbalance in current generation between the sub-cells were measured: 6.96 mA/cm^2 for the CGSe cell, 9.63 mA/cm^2 for the shaded CIGSe. Necessity for current matching by bandgap and thickness optimization to maximize performance is evident by the EQE measurements, however the complementary light response was satisfactory for our proof-of-concept experiment.

Subsequent JV measurements were performed on CGSe/CIGSe semi-monolithic MJ cells. Since the solar simulator cannot be accurately calibrated simultaneously for both the narrow- and wide-bandgap sub-cells once integrated into the tandem device, the short-circuit current density of a CGSe/CIGSe semi-monolithic MJ cell (J_{SC} = 7.3 mA/cm^2) measured under outdoor conditions, recorded the moment an adjacent NREL-certified Si photodiode (300-1100nm) reached its calibrated value for AM1.5G illumination, was used to calibrate the intensity of the solar simulator. The champion device of area 0.06 cm^2 showed a PCE of 5.04% with V_{OC}, J_{SC} and FF of 1.24 V, 7.19 mA/cm^2, and 56.72%, respectivey (Figure 77d). The solid-state characteristics of the champion device along with that of its sub-cells are summarized in Table 5. With the current state-of-the-art of our process, the 5% PCE is lower than what was achieved with mechanical stacks, but higher than that reported for monolithic tandems. Semi-monolithically integrated chalcopyrite-based tandems with higher PCE are expected as the exfoliation/transfer process is refined, and our understanding of wide-bandgap chalcopyrite PV, especially their interface with better optimized buffer layers, improves.

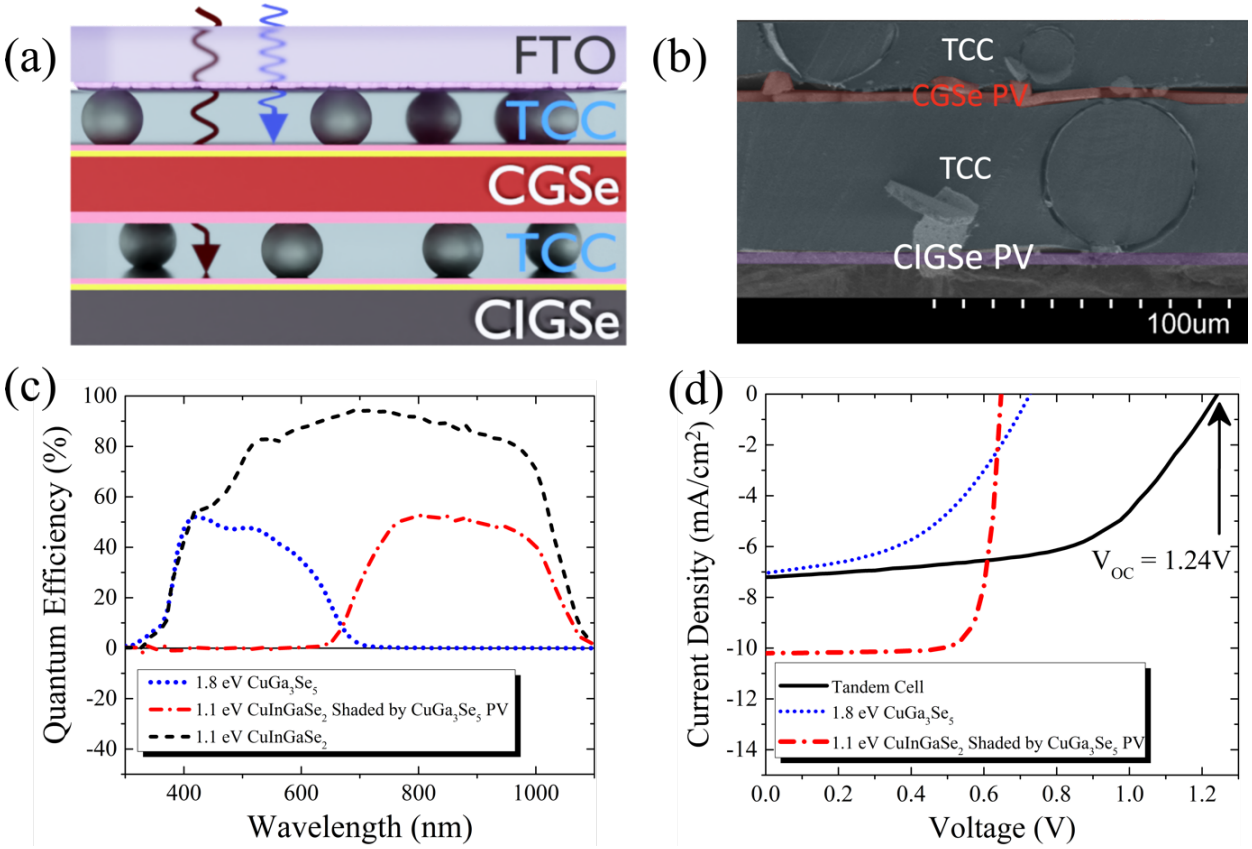

Figure 77: (a) Schematic and (b) colored cross-sectional SEM micrograph of a semi-monolithic tandem cell comprising a $CuGa_3Se_5$ and a $CuInGaSe_2$ sub-cells exfoliated from their original Mo/SLG substrates, interconnected, and bonded onto a FTO substrate using TCC layers. (c) EQE of the top $CuGa_3Se_5$ cells and optically shaded bottom $CuInGaSe_2$ cell. The EQE of unshaded $CuInGaSe_2$ is included for reference. (d) Photocurrent-voltage characteristic of the champion tandem device presented along that of the constituent top $CuGa_3Se_5$ cell and optically shaded bottom $CuInGaSe_2$ cell.

Table 5: Performance summary of the champion semi-monolithic tandem device and its constituent sub-cell baseline measurements. Performances of the un-shaded CuInGaSe2 cell are included for reference.

Device	Voc (V)	Jsc (mA/cm^2)	FF (%)	PCE (%)
$CuGa_3Se_5$ / $CuInGaSe_2$	1.24	7.2	56.7	5.0
$CuGa_3Se_5$	0.73	7.0	47.1	2.4
$CuInGaSe_2$ Shaded	0.65	10.2	79.7	5.3
$CuInGaSe_2$	0.68	33.0	79.6	17.9

c. Hybrid Photoelectrochemical Devise Integration

Knowing the semi-monolithic approach can lead to efficient multi-junction solid-state devices, we then focused on combining wide bandgap chalcopyrite cells with narrow bandgap "PV drivers" to create functional tandem water splitting devices. First, a 25mm x 25mm 1.85 eV $CuGa_3Se_5$ (CGSe) PV stacks grown on Mo-coated glass was bonded face down onto a FTO substrate using a TCC layer. After overnight curing, the FTO/TCC/CGSe PV/Mo/glass sandwich was subject to exfoliation, inducing delamination at the CGSe/Mo interface and transferring the PV stack from the Mo/glass to the FTO substrate. The FTO/TCC/CGSe stack was then bonded onto a fully processed 1.4 eV perovskite solar cell (PSC), forming the world's first CGSe/PSC semi-monolithic tandem structure (Figure 78a). Solid-state current-voltage (J-V) measurements performed on champion tandem exhibited a short-circuit photocurrent density (Jsc) and open circuit voltage (Voc) of 7.58 mA/cm^2 and 1.52 V, respectively (Figure 78b).

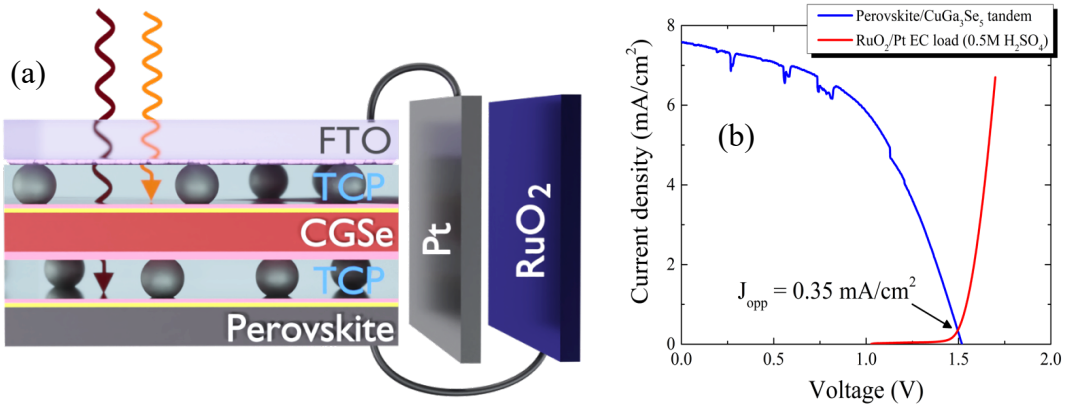

Figure 78. (a) Schematic of the perovskite/chalcopyrite semi-monolithic tandem cell connected to a Pt-RuO_2 electrochemical load. (b) Load line analysis between the perovskite/chalcopyrite semi-monolithic tandem cell and Pt-RuO_2 electrochemical load with operating short circuit photocurrent density of 0.35 mA/cm^2.

The high Voc produced by the tandem allowed us to achieve for the first time unbiased PEC water splitting with chalcopyrite-based PEC devices, as demonstrated by the load line analysis in Figure 78b. In this graph, the linear sweep voltammetry (LSV) measured independently on a Pt/RuO_2 electrochemical load (2-electrode configuration, no sacrificial agent) is plotted alongside the JV of the tandem. The operating point of the coupled tandem-Pt/RuO_2 device was 0.35 mA/cm^2 at

1.48V, leading to a solar-to-hydrogen efficiency (STH) of 0.34% (using a faradaic efficiency of 96% measured in house on Pt cathode). Unbiased water splitting was confirmed by chronoamperometry measurement of the wired tandem-Pt/RuO_2 device, as presented in Figure 79a. Although modest, this achievement demonstrates that the proposed semi-monolithic approach is a viable technique to combine thermally, mechanically and/or chemically incompatible material classes, such as chalcopyrite and perovskites. It is worth noting that any improvement of each sub-cell's solid-state properties would lead to significant STH increase. Our team demonstrated that Voc for CGSe as high as 925mV can be achieved with MgZnO (MZO) buffer layers, however this present PEC experiment was accomplished using a CdS buffer which produced Voc of 670 mV at best. Using MZO instead of CdS would have "shifted" the tandem JV curve to the right by ~250 mV and move the operating point to a higher current density, resulting in greater STH efficiency.

To better illustrate this point, we plot in Figure 79b the applied bias photon-to-current efficiency (APBE) calculated for the tandem-Pt/RuO_2 device. In short, ABPE represents the efficiency the device would produce with help from an additional (modest) bias. It is worth noting that APBE is not STH, however it provides important diagnostics on the limitations of the current tandem structures and highlight where efforts should be devoted in the future. With no additional bias, ABPE is equal to STH (0.34% in this case). Applying a bias of 250 mV leads to a ABPE of 2.3%, a value our group would have achieved under zero bias using MZO instead of CdS. Finally, a maximum ABPE of 3.25% was calculated for a bias of 400 mV. Beyond this maximum value, ABPE drops and eventually reaches 0% when the applied bias is equal to or greater than the water splitting potential (1.23V).

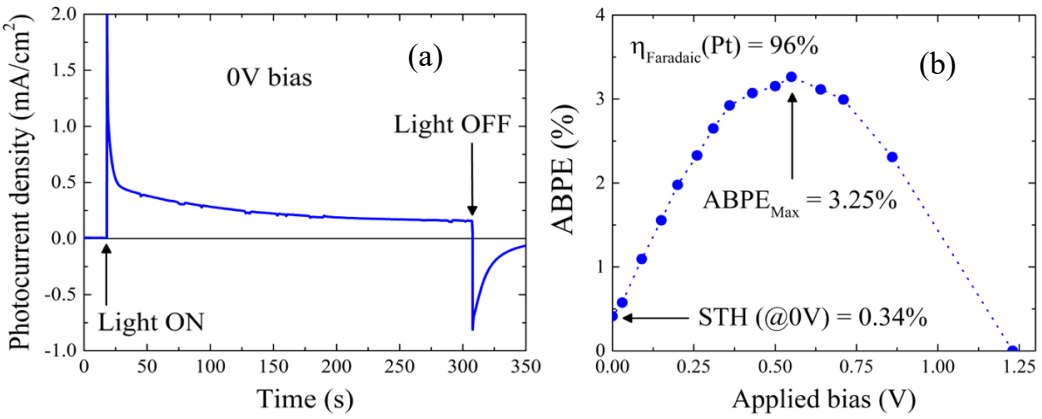

Figure 79. (a) Current vs. time characteristic measured on the perovskite/chalcopyrite semi-monolithic tandem cell series connected to a Pt-RuO_2 electrochemical load. (b) Applied bias photon-to-current efficiency characteristic of the device.

The same methodology was applied to form a semi-monolithic tandem cell comprising a 1.85 eV CGSe top cell and a 1.13eV $CuInGaSe_2$ PV driver. The tandem produced a Jsc and Voc of 7.2 mA/cm^2 and 1.2V, respectively (Figure 80a). Considering overpotentials for water splitting, such device cannot spontaneously drive the hydrogen evolution reaction, as indicated by the absence of any operating point between the tandem J-V and the Pt-RuO_2 electrochemical load in Figure 80a. An maximum ABPE of 2.56% was calculated for an applied bias of 0.7V (Figure 80b). This analysis suggest triple junction architecture will be most likely needed for whole-chalcopyrite based PEC water splitting.

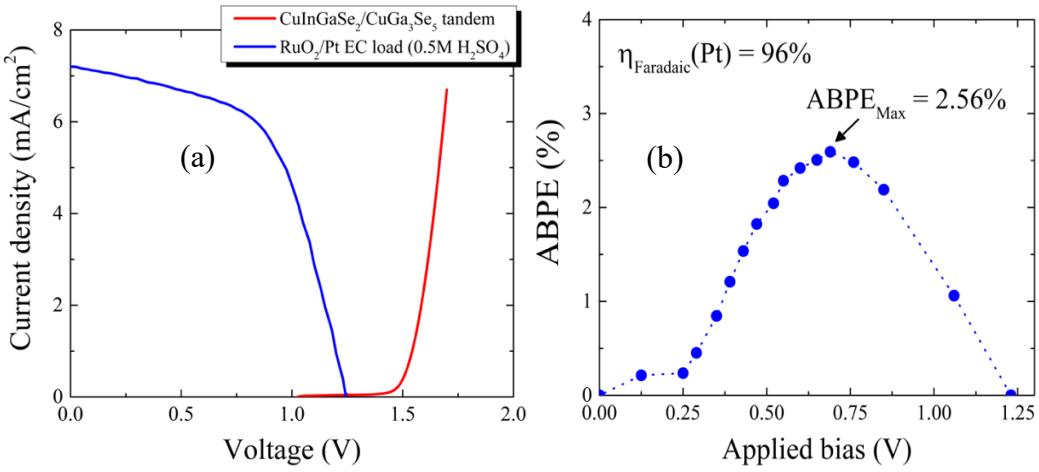

Figure 80. (a) Load line analysis between a chalcopyrite/chalcopyrite semi-monolithic tandem cell and a Pt-RuO_2 electrochemical load with no appreciable operating short circuit photocurrent density. (b) Applied bias photon-to-current efficiency characteristic of the device.

Summary: Our results demonstrate a multi-junction assembly of a new kind that circumvents thin-film chemical, thermal and mechanical incompatibilities during integration. Proof-of-concept whole-chalcopyrite tandems were obtained by consecutive exfoliation and transfer of fully integrated 1.85 eV $CuGa_3Se_5$ and 1.13 eV $CuInGaSe_2$ PV stacks from their Mo/SLG substrates onto a new single FTO host substrate. Areas as large as 25 × 25 mm^2 were successfully transferred without appreciable cracking or formation of pinholes in the absorber from the separation. A champion device of area 0.06 cm^2 showed a PV efficiency of 5.04% with an open-circuit voltage, short-circuit current density and fill factor of 1.24 V, 7.19 mA/cm^2, and 56.7%, respectivey. In the context of PEC water splitting, semi-monolithically integrated tandems comprising a chalcopyrite top cell and perovskite bottom cell were created for the first time. Although modest, the achieved STH efficiency (0.34%) proves the feasibility of proposed concept. Higher efficiencies are expected with future refinement of the exfoliation/transfer process, and our understanding of wide-bandgap chalcopyrite PV, especially their interface with better optimized buffer layers,[11] improves.

6. Project summary and outlook

By combining unique analytical techniques, state-of-the-art theoretical modeling with cutting-edge thin film materials synthesis, we permitted the development of promising materials candidates with tunable bulk and/or interface properties for PEC water splitting. Using theoretical modeling, we have surveyed a number of alloys covering the compositional space of $(Cu,Ag)(B,Al,Ga,In)(S,Se)_2$ chalcopyrites to identify materials that exhibit the most promising combination of electronic structure and reliable synthesis, translating to materials with suitable band gaps, band edge positions, stability, and favorable defect properties for realizing the required properties necessary to drive photoelectrochemical hydrogen production. Novel synthesis processes were developed, including solution-processed approaches capable of passivating defects in chalcopyrites during growth. Advanced surface passivation methods were investigated to improve the durability of chalcopyrite PEC candidates. For instance, X-ray photoelectron spectroscopy characterization of $CuGa_3Se_5$ films indicated that a Ga_2O_3 thin native oxide forms on the surface of $CuGa_3Se_5$ films, as predicted by the Pourbaix diagram of the gallium-water system. We speculate that Ga_2O_3 can self-passivate chalcopyrites and enhance their durability, as suggested by the prolonged durability of Ga-rich OVCs ($CuGa_3Se_5$) over CGSe photoelectrodes. We demonstrated the utility of $CuGa_3Se_5$ absorbers coated with ultrathin WO_3 coatings for long-term operation of solar-driven hydrogen production and achieve a new durability milestone for any non-silicon photocathode device, passing 21,490 C cm^{-2} of charge over six weeks of continuously illuminated testing under applied bias. Using novel MgZnO (MZO) buffer layers, we achieved open circuit voltage (V_{OC}) of 925 mV with $CuGa_3Se_5$ wide bandgap top cell. Combined with a high efficiency narrow bandgap $CuInGaSe_2$ (V_{OC} = 700 mV), a MZO-$CuGa_3Se_5$-based tandem could potentially generate sufficient photovoltage for unassisted PEC water splitting. Finally, we developed a *semi-monolithic* integration method to circumvent processing incompatibility between materials of dissimilar classes and combine them into efficient multi-junction PEC devices. Proof-of-concept whole-chalcopyrite tandems were obtained by consecutive exfoliation and transfer of fully integrated un-patterned 1.85 eV $CuGa_3Se_5$ and 1.13 eV $CuInGaSe_2$ PV stacks from their Mo/soda lime glass substrates onto a new single host substrate. A champion semi-monolithic tandem device showed a PV efficiency of 5.04% with open-circuit voltage as high as 1.24 V. This first-time manufacturing process of a fully operational semi-monolithic device whilst maintaining state-of-the-art sub-cell cell processing provides a new prospect for thin-film/thin-film tandem PEC devices beyond the chalcopyrite class.

7. Disclaimer

This report was prepared as an account of work sponsored by an agency of the United States Government. Neither the United States Government nor any agency thereof, nor any of their employees, makes any warranty, express or implied, or assumes any legal liability or responsibility for the accuracy, completeness, or usefulness of any information, apparatus, product, or process disclosed, or represents that its use would not infringe privately owned rights. Reference herein to any specific commercial product, process, or service by trade name, trademark, manufacturer, or otherwise does not necessarily constitute or imply its endorsement, recommendation, or favoring by the United States Government or any agency thereof. The views and opinions of authors expressed herein do not necessarily state or reflect those of the United States Government or any agency thereof.

8. Products developed under the Award

a. Research papers

(6) **Invited:** *A Perspective on Ordered Vacancy Compound and Parent Chalcopyrite Thin Film Absorbers for Photoelectrochemical Water Splitting (Featured Article),* N. Gaillard*, Appl. Phys. Lett **119**, 090501 (2021). https://doi.org/10.1063/5.0061774

(5) *Performance and Limits of 2.0 eV Bandgap $CuInGaS_2$ Solar Absorber Integrated with CdS Buffer on F:SnO_2 Substrate for Multijunction Photovoltaic and Photoelectrochemical Water Splitting Devices,* N. Gaillard*, W. Septina, J. Varley, T. Ogitsu, K. Ohtaki, H. A. Ishii, J. P. Bradley, C. P. Muzzillo, K. Zhu, F. Babbe and J. Cooper, Mater. Adv. 2, 5752 (2021). https://doi.org/10.1039/D1MA00570G

(4) *In-situ Al_2O_3 Incorporation Enhances the Efficiency of $CuIn(S,Se)_2$ Solar Cells Prepared from Molecular-Ink Solutions*, W. Septina, C. Muzzillo, C. Perkins, A. Curtis Giovanelli, T. West, K. K. Ohtaki, H. A. Ishii, J. P. Bradley, K. Zhu and N. Gaillard*, J. Mater. Chem. A 9, 10419 (2021). https://doi.org/10.1039/D1TA00768H

(3) *$Mg_xZn_{1-x}O$ Contact to $CuGa_3Se_5$ Absorber for Photovoltaic and Photoelectrochemical Devices*, I. Kahn, C. Muzzillo, C. Perkins, A. Norman, J. Young N. Gaillard and A. Zakutayev, Journal of Physics: Energy **3**, 024001 (2021). doi.org/10.1088/2515-7655/abd3b3

(2) *Tungsten Oxide-Coated Copper Gallium Selenide Sustains Long-Term Solar Hydrogen Evolution*, D. W. Palm, C. P. Muzzillo, M. Ben-Naim, I. Kahn, N. Gaillard and T. F. Jaramillo*, Sustainable Energy & Fuel (2021). https://doi.org/10.1039/D0SE00487A

(1) *Assessing the roles of Cu- and Ag-deficient layers in chalcopyrite-based solar cells through first principles calculations (Editor's Pick), A. Sharan, F. P. Sabino, A. Janotti*, N. Gaillard, T. Ogitsu and J. B. Varley*, Journal of Applied Physics **127**, 065303 (2020). https://doi.org/10.1063/1.5140736

b. Invited presentations

(3) *Potentials and Challenges of Wide Bandgap Copper Chalcopyrite Thin Film Absorbers for Photoelectrochemical Water Splitting Applications ,* N. Gaillard, 239th Electrochemical Society Meeting, Symposium I03, I03-1242, Spring Digital Meeting, 2021.

(2) *Synthesis and Integration of Wide Bandgap Chalcopyrite Candidates for Photoelectrochemical Water Splitting Applications,* N. Gaillard, 238th Electrochemical Society Meeting, Symposium L04, L04-3091, Virtual Conference, 2020.

(1) *Emerging Chalcopyrite Photo-absorbers for Renewable Hydrogen Production*, N. Gaillard, 236th Electrochemical Society Meeting, Symposium I04, 1909, Atlanta (GA), 2019.

c. Contributed presentations

(7) *Semi-Monolithic Chalcopyrite-Based Multijunction Solar Devices*, N. Gaillard, W. Septina, J. Crunk, K. Outlaw-Spruell and T. West, European Materials Research Society Spring Meeting, Virtual Meeting, A.II.2, (2021).

(6) *A Transparent Polymer Impregnated with Conductive Particles for Tandem Photovoltaic Devices*, J. Crunk, K. Outlaw-Spruell and N. Gaillard, Materials Research Society Spring Meeting, Joint Symposium EN07/EN06, EN07.01/EN06.01.05, Digital Meeting, 2021.

(5) *Semi-Monolithic Tandem Solar Cell Architecture for Photoelectrochemical Water Splitting*, K. Outlaw-Spruell, J. Crunk, W. Septina and N. Gaillard, Materials Research Society Spring Meeting, Symposium EN02, EL02.04.04, Digital Meeting, 2021.

(4) *Emerging Wide Bandgap Chalcopyrites and Integration Methods for Efficient Multijunction Solar Devices*, N. Gaillard, A. Deangelis, W. Septina and J. Crunk, Virtual Chalcogenide PV Conference, Session 01 – Tandems, 0915, 2020.

(3) *First-Principles Simulations of Stability, Optical and Electronic Properties of Competing Phases in Chalcopyrite-Based Photoelectrodes*, J. Varley, A. Sharan, P. Sabino, A. Janotti, T. Ogitsu and N. Gaillard, Materials Research Society Fall Meeting, Symposium EL04, EL04.10.07, Boston (MA), 2019.

(2) *Atomic Layer Deposited Tungsten-Based Coatings for Durable Solar Hydrogen Production,* D. Palm, C. Muzzillo, N. Gaillard and T. Jaramillo, 236th Electrochemical Society Meeting, Symposium I04, 1899, Atlanta (GA), 2019.

(1) *First-Principles Simulations of Stability, Optical and Electronic Properties of Competing Phases in Chalcopyrite-Based Photoelectrodes*, J. Varley, A. Sharan, T. Ogitsu, A. Janotti, A. Deangelis and N. Gaillard, 235th Electrochemical Society Meeting, Symposium I03, 1627, Dallas (TX), 2019.

d. Poster presentations

(3) *Enhanced Efficiency of Solution-Processed CuIn(S,Se)$_2$ Solar Cells by In Situ Incorporation of Al_2O_3,* W. Septina, C. Muzzillo, C. Perkins, A. C. Giovanelli, T. West, K. Ohtaki, H. Ishii, J. Bradley, Kai Zhu and N. Gaillard, Materials Research Society Spring Meeting, Symposium EN07, EN07.909.05, Digital Meeting, 2021.

(2) *High Efficiency Solution-Processed Aluminum-Alloyed Chalcopyrite Thin Film Solar,* W. Septina, T. West, A. C. Giovanelli and N. Gaillard, 238th Electrochemical Society Meeting, Symposium H02, H02-1908, Virtual conference, 2020.

(1) *Tandem Solar Device Integration Using Transversely Conductive Polymer Composites,* J. Crunk, A. Deangelis and N. Gaillard, 238th Electrochemical Society Meeting, Symposium L04, L04-3124, Virtual conference, 2020.

9. References cited

1. Gaillard, N.; Chang, Y.; Kaneshiro, J.; Deangelis, A.; Miller, E. L. Status of Research on Tungsten Oxide-Based Photoelectrochemical Devices at the University of Hawai'i. in *Proc. SPIE - Int. Soc. Opt. Eng.* (eds. Idriss, H.; Wang, H.) **2010**, 7770, 77700V.
2. Rocheleau, R. E.; Miller, E. L.; Misra, A. High-Efficiency Photoelectrochemical Hydrogen Production Using Multijunction Amorphous Silicon Photoelectrodes. *Energy & Fuels* **1998**, 12, 3–10.
3. Kaneshiro, J.; Gaillard, N.; Rocheleau, R.; Miller, E. Advances in Copper-Chalcopyrite Thin Films for Solar Energy Conversion. *Sol. Energy Mater. Sol. Cells* **2010**, 94, 12–16.
4. Gaillard, N.; Prasher, D.; Chong, M.; Deangelis, A.; Horsley, K.; Ishii, H. A.; Bradley, J. P.; Varley, J.; Ogitsu, T. Wide-Bandgap Cu(In,Ga)S 2 Photocathodes Integrated on Transparent Conductive F:SnO 2 Substrates for Chalcopyrite-Based Water Splitting Tandem Devices. *ACS Appl. Energy Mater.* **2019**, 2, 5515–5524.
5. DeAngelis, A. D.; Horsley, K.; Gaillard, N. Wide Band Gap CuGa(S,Se) 2 Thin Films on Transparent Conductive Fluorinated Tin Oxide Substrates as Photocathode Candidates for Tandem Water Splitting Devices. *J. Phys. Chem* 122, 14304–14312,.
6. Muzzillo, C. P.; Klein, W. E.; Li, Z.; Deangelis, A. D.; Horsley, K.; Zhu, K.; Gaillard, N. Low-Cost, Efficient, and Durable H2 Production by Photoelectrochemical Water Splitting with CuGa3Se5 Photocathodes. *ACS Appl. Mater. Interfaces* **2018**, 10, 19573–19579.
7. Jacobsson, T. J.; Fjällström, V.; Sahlberg, M.; Edoff, M.; Edvinsson, T. A Monolithic Device for Solar Water Splitting Based on Series Interconnected Thin Film Absorbers Reaching over 10% Solar-to-Hydrogen Efficiency. *Energy Environ. Sci.* **2013**, 6, 3676.
8. Gaillard, N.; Septina, W.; Varley, J.; Ogitsu, T.; Ohtaki, K. K.; Ishii, H. A.; Bradley, J. P.; Muzzillo, C.; Zhu, K.; Babbe, F.; Cooper, J. Performance and Limits of 2.0 EV Bandgap CuInGaS 2 Solar Absorber Integrated with CdS Buffer on F:SnO 2 Substrate for Multijunction Photovoltaic and Photoelectrochemical Water Splitting Devices. *Mater. Adv.* **2021**.

9. Septina, W.; Muzzillo, C. P.; Perkins, C. L.; Giovanelli, A. C.; West, T.; Ohtaki, K. K.; Ishii, H. A.; Bradley, J. P.; Zhu, K.; Gaillard, N. In Situ Al2O3 Incorporation Enhances the Efficiency of CuIn(S,Se)2 Solar Cells Prepared from Molecular-Ink Solutions. *J. Mater. Chem. A* **2021**, 9, 10419–10426.

10. Hellstern, T. R.; Palm, D. W.; Carter, J.; Deangelis, A. D.; Horsley, K.; Weinhardt, L.; Yang, W.; Blum, M.; Gaillard, N.; Heske, C.; Jaramillo, T. F. Molybdenum Disulfide Catalytic Coatings via Atomic Layer Deposition for Solar Hydrogen Production from Copper Gallium Diselenide Photocathodes. *ACS Appl. Energy Mater.* **2019**, 2, 1060–1066.

11. Kahn. MgxZn1-XO Contact to CuGa3Se5 Absorber for Photovoltaic Andphotoelectrochemical Devices. **2021**,

12. Kijima, S.; Nakada, T. High-Temperature Degradation Mechanism of Cu(In,Ga)Se2-Based Thin Film Solar Cells. *Appl. Phys. Express* **2008**, 1, 0750021–0750023.

13. Seitz, L. C.; Chen, Z.; Forman, A. J.; Pinaud, B. A.; Benck, J. D.; Jaramillo, T. F. Modeling Practical Performance Limits of Photoelectrochemical Water Splitting Based on the Current State of Materials Research. *ChemSusChem* **2014**, 7, 1372–1385.

14. Sharan, A.; Sabino, F. P.; Janotti, A.; Gaillard, N.; Ogitsu, T.; Varley, J. B. Assessing the Roles of Cu- and Ag-Deficient Layers in Chalcopyrite-Based Solar Cells through First Principles Calculations. *J. Appl. Phys.* **2020**, 127, 065303.

15. Ishizuka, S.; Nishinaga, J.; Iioka, M.; Higuchi, H.; Kamikawa, Y.; Koida, T.; Shibata, H.; Fons, P. Si-Doped Cu(In,Ga)Se2 Photovoltaic Devices with Energy Conversion Efficiencies Exceeding 16.5% without a Buffer Layer. *Adv. Energy Mater.* **2018**, 8, 1–7.

16. Gaillard, N. A Perspective on Ordered Vacancy Compound and Parent Chalcopyrite Thin Film Absorbers for Photoelectrochemical Water Splitting. *Appl. Phys. Lett.* **2021**, 119, 090501.

17. Wolter, M. H.; Carron, R.; Avancini, E.; Bissig, B.; Weiss, T. P.; Nishiwaki, S.; Feurer, T.; Buecheler, S.; Jackson, P.; Witte, W.; Siebentritt, S. How Band Tail Recombination Influences the Open-Circuit Voltage of Solar Cells. *Prog. Photovoltaics Res. Appl.* **2021**, 1–11.

18. Babbe, F.; Choubrac, L.; Siebentritt, S. The Optical Diode Ideality Factor Enables Fast Screening of Semiconductors for Solar Cells. *Sol. RRL* **2018**, 2, 1–6.

19. Heske, C.; Groh, U.; Fuchs, O.; Umbach, E.; Franco, N.; Bostedt, C.; Terminello, L. J.; Perera, R. C. C.; Hallmeier, K. H.; Preobrajenski, A.; Szargan, R.; Zweigart, S.; Riedl, W.; Karg, F. X-Ray Emission Spectroscopy of Cu(In,Ga)(S,Se)2-Based Thin Film Solar Cells: Electronic Structure, Surface Oxidation, and Buried Interfaces. *Phys. Status Solidi* **2001**, 187, 13–24.

20. NIST X-Ray Photoelectron Spectroscopy Database, NIST Standard Reference Database Number 20, National Institute of Standards and Technology, Gaithersburg MD, 20899. **2000**,

21. Weinhardt, L.; Fuchs, O.; Groß, D.; Storch, G.; Umbach, E.; Dhere, N. G.; Kadam, A. A.; Kulkarni, S. S.; Heske, C. Band Alignment at the CdS Cu (In,Ga) S2 Interface in Thin-Film Solar Cells. *Appl. Phys. Lett.* **2005**, 86, 1–3.

22. Walter, M. G.; Warren, E. L.; McKone, J. R.; Boettcher, S. W.; Mi, Q.; Santori, E. a; Lewis, N. S. Solar Water Splitting Cells. *Chem. Rev.* **2010**, 110, 6446–73.

23. Hu, S.; Lewis, N. S.; Ager, J. W.; Yang, J.; McKone, J. R.; Strandwitz, N. C. Thin-Film Materials for the Protection of Semiconducting Photoelectrodes in Solar-Fuel Generators. *J. Phys. Chem. C* **2015**, 119, 24201–24228.

24. Guijarro, N.; Prévot, M. S.; Sivula, K. Surface Modification of Semiconductor Photoelectrodes. *Phys. Chem. Chem. Phys.* **2015**, 17, 15655–15674.

25. Bae, D.; Seger, B.; Vesborg, P. C. K.; Hansen, O.; Chorkendorff, I. Strategies for Stable Water Splitting via Protected Photoelectrodes. *Chem. Soc. Rev.* **2017**, 46, 1933–1954.

26. Seger, B.; Tilley, D. S.; Pedersen, T.; Vesborg, P. C. K.; Hansen, O.; Grätzel, M.; Chorkendorff, I. Silicon Protected with Atomic Layer Deposited TiO2: Durability Studies of Photocathodic H2 Evolution. *RSC Adv.* **2013**, 3, 25902.

27. King, L. A.; Hellstern, T. R.; Park, J.; Sinclair, R.; Jaramillo, T. F. Highly Stable Molybdenum Disulfide Protected Silicon Photocathodes for Photoelectrochemical Water Splitting. *ACS Appl. Mater. Interfaces* **2017**, 9, 36792–36798.

28. Bae, D.; Seger, B.; Hansen, O.; Vesborg, P. C. K.; Chorkendorff, I. Durability Testing of Photoelectrochemical Hydrogen Production under Day/Night Light Cycled Conditions. *ChemElectroChem* **2019**, 6, 106–109.

29. Moriya, M.; Minegishi, T.; Kumagai, H.; Katayama, M.; Kubota, J.; Domen, K. Stable Hydrogen Evolution from CdS-Modified CuGaSe2 Photoelectrode under Visible-Light Irradiation. *J. Am. Chem. Soc.* **2013**, 135, 3733–5.

30. Zhang, L.; Minegishi, T.; Nakabayashi, M.; Suzuki, Y.; Seki, K.; Shibata, N.; Kubota, J.; Domen, K. Durable Hydrogen Evolution from Water Driven by Sunlight Using (Ag,Cu)GaSe 2 Photocathodes Modified with CdS and CuGa 3 Se 5. *Chem. Sci.* **2015**, 6, 894–901.

31. Kumagai, H.; Minegishi, T.; Sato, N.; Yamada, T.; Kubota, J.; Domen, K. Efficient Solar Hydrogen Production from Neutral Electrolytes Using Surface-Modified Cu(In,Ga)Se 2 Photocathodes. *J. Mater. Chem. A* **2015**, 3, 8300–8307.

32. Wang, Y.; Wu, Y.; Schwartz, J.; Sung, S. H.; Hovden, R.; Mi, Z. A Single-Junction Cathodic Approach for Stable Unassisted Solar Water Splitting. *Joule* **2019**, 3, 2444–2456.

33. Guijarro, N.; Prévot, M. S.; Yu, X.; Jeanbourquin, X. A.; Bornoz, P.; Bourée, W.; Johnson, M.; Le Formal, F.; Sivula, K. A Bottom-Up Approach toward All-Solution-Processed High-Efficiency Cu(In,Ga)S 2 Photocathodes for Solar Water Splitting. *Adv. Energy Mater.* **2016**, 6, 1501949.

34. Gunawan; Septina, W.; Ikeda, S.; Harada, T.; Minegishi, T.; Domen, K.; Matsumura, M. Platinum and Indium Sulfide-Modified CuInS 2 as Efficient Photocathodes for Photoelectrochemical Water Splitting. *Chem. Commun.* **2014**, 50, 8941.

35. Mali, M. G.; Yoon, H.; Joshi, B. N.; Park, H.; Al-Deyab, S. S.; Lim, D. C.; Ahn, S.; Nervi, C.; Yoon, S. S. Enhanced Photoelectrochemical Solar Water Splitting Using a Platinum-Decorated CIGS/CdS/ZnO Photocathode. **2015**,

36. Jacobsson, T. J.; Platzer-Björkman, C.; Edoff, M.; Edvinsson, T. CuInxGa1−xSe2 as an Efficient Photocathode for Solar Hydrogen Generation. *Int. J. Hydrogen Energy* **2013**, 38, 15027–15035.

37. Ikeda, S.; Nakamura, T.; Lee, S. M.; Yagi, T.; Harada, T.; Minegishi, T.; Matsumura, M. Photoreduction of Water by Using Modified CuInS2 Electrodes. *ChemSusChem* **2010**, 4, n/a-n/a.

38. Marsen, B.; Cole, B.; Miller, E. L. Photoelectrolysis of Water Using Thin Copper Gallium Diselenide Electrodes. *Sol. Energy Mater. Sol. Cells* **2008**, 92, 1054–1058.

39. Kumagai, H.; Minegishi, T.; Moriya, Y.; Kubota, J.; Domen, K. Photoelectrochemical Hydrogen Evolution from Water Using Copper Gallium Selenide Electrodes Prepared by a Particle Transfer Method. *J. Phys. Chem. C* **2014**, 118, 16386–16392.

40. Septina, W.; Gunawan; Ikeda, S.; Harada, T.; Higashi, M.; Abe, R.; Matsumura, M. Photosplitting of Water from Wide-Gap Cu(In,Ga)S2 Thin Films Modified with a CdS Layer and Pt Nanoparticles for a High-Onset-Potential Photocathode. *J. Phys. Chem. C* **2015**, 119, 8576–8583.

41. Zhang, L.; Minegishi, T.; Kubota, J.; Domen, K. Hydrogen Evolution from Water Using AgxCu1−xGaSe2 Photocathodes under Visible Light. *Phys. Chem. Chem. Phys.* **2014**, 16, 6167.

42. Luo, J.; Tilley, S. D.; Steier, L.; Schreier, M.; Mayer, M. T.; Fan, H. J.; Grätzel, M. Solution Transformation of Cu 2 O into CuInS 2 for Solar Water Splitting. *Nano Lett.* **2015**, 15, 1395–1402.

43. Chen, M.; Liu, Y.; Li, C.; Li, A.; Chang, X.; Liu, W.; Sun, Y.; Wang, T.; Gong, J. Spatial Control of Cocatalysts and Elimination of Interfacial Defects towards Efficient and Robust CIGS Photocathodes for Solar Water Splitting. *Energy Environ. Sci.* **2018**, 11, 2025–2034.

44. Zhao, J.; Minegishi, T.; Zhang, L.; Zhong, M.; Gunawan; Nakabayashi, M.; Ma, G.; Hisatomi, T.; Katayama, M.; Ikeda, S.; Shibata, N.; Yamada, T.; Domen, K. Enhancement of Solar Hydrogen Evolution from Water by Surface Modification with CdS and TiO 2 on Porous CuInS 2 Photocathodes Prepared by an Electrodeposition-Sulfurization Method. *Angew. Chemie Int. Ed.* **2014**, 53, 11808–11812.

45. Kim, J.; Minegishi, T.; Kobota, J.; Domen, K. Enhanced Photoelectrochemical Properties of CuGa3Se5 Thin Films for Water Splitting by the Hydrogen Mediated Co-Evaporation Method. *Energy Environ. Sci.* **2012**, 5, 6368–6374.

46. Kageshima, Y.; Minegishi, T.; Goto, Y.; Kaneko, H.; Domen, K. Particulate Photocathode Composed of (ZnSe) 0.85 (CuIn 0.7 Ga 0.3 Se 2) 0.15 Synthesized with Na 2 S for Enhanced Sunlight-Driven Hydrogen Evolution. *Sustain. Energy Fuels* **2018**, 2, 1957–1965.

47. Higashi, T.; Kaneko, H.; Minegishi, T.; Kobayashi, H.; Zhong, M.; Kuang, Y.; Hisatomi, T.; Katayama, M.; Takata, T.; Nishiyama, H.; Yamada, T.; Domen, K. Overall Water Splitting by Photoelectrochemical Cells Consisting of (ZnSe) 0.85 (CuIn 0.7 Ga 0.3 Se 2) 0.15 Photocathodes and BiVO 4 Photoanodes. *Chem. Commun.* **2017**,

48. Kaneko, H.; Minegishi, T.; Nakabayashi, M.; Shibata, N.; Kuang, Y.; Yamada, T.; Domen, K. A Novel Photocathode Material for Sunlight-Driven Overall Water Splitting: Solid Solution of ZnSe and Cu(In,Ga)Se 2. *Adv. Funct. Mater.* **2016**, 26, 4570–4577.

49. Pourbaix, M. *Atlas of Electrochemical Equilibria in Aqueous Solutions*. **1966**,

50. Yoon, K. H.; Shin, C. W.; Kang, D. H. Photoelectrochemical Conversion in a WO3 Coated P-Si Photoelectrode: Effect of Annealing Temperature. *J. Appl. Phys.* **1997**, 81, 7024–7029.

51. Chen, Y. W.; Prange, J. D.; Dühnen, S.; Park, Y.; Gunji, M.; Chidsey, C. E. D.; McIntyre, P. C. Atomic Layer-Deposited Tunnel Oxide Stabilizes Silicon Photoanodes for Water Oxidation. *Nat. Mater.* **2011**, 10, 539–544.

52. Yoon, K. H.; Lee, J. W.; Cho, Y. S.; Kang, D. H. Photoeffects in WO 3 /GaAs Electrode. *J. Appl. Phys.* **1996**, 80, 6813–6818.

53. Yoon, K. H.; Seo, D. K.; Cho, Y. S.; Kang, D. H. Effect of Pt Layers on the Photoelectrochemical Properties of a WO3/p-Si Electrode. *J. Appl. Phys.* **1998**, 84, 3954–3959.

54. Liu, R.; Lin, Y.; Chou, L.-Y.; Sheehan, S. W.; He, W.; Zhang, F.; Hou, H. J. M.; Wang, D. Water Splitting by Tungsten Oxide Prepared by Atomic Layer Deposition and Decorated with an Oxygen-Evolving Catalyst. *Angew. Chemie* **2011**, 123, 519–522.

55. Bär, M.; Weinhardt, L.; Marsen, B.; Cole, B.; Gaillard, N.; Miller, E.; Heske, C. Mo Incorporation in WO3 Thin Film Photoanodes: Tailoring the Electronic Structure for Photoelectrochemical Hydrogen Production. *Appl. Phys. Lett.* **2010**, 96, 032107.

56. Mezher, M.; Garris, R.; Mansfield, L. M.; Horsley, K.; Weinhardt, L.; Duncan, D. A.; Blum, M.; Rosenberg, S. G.; Bär, M.; Ramanathan, K.; Heske, C. Electronic Structure of the Zn(O,S)/Cu(In,Ga)Se 2 Thin-Film Solar Cell Interface. *Prog. Photovoltaics Res. Appl.* **2016**, 24, 1142–1148.

57. Hauschild, D.; Meyer, F.; Benkert, A.; Kreikemeyer-Lorenzo, D.; Dalibor, T.; Palm, J.; Blum, M.; Yang, W.; Wilks, R. G.; Bär, M.; Reinert, F.; Heske, C.; Weinhardt, L. Improving Performance by Na Doping of a Buffer Layer-Chemical and Electronic Structure of the In x S Y :Na/CuIn(S,Se) 2 Thin-Film Solar Cell Interface. *Prog. Photovoltaics Res. Appl.* **2018**, 26, 359–366.

58. Kim, J.; Minegishi, T.; Kobota, J.; Domen, K. Investigation of Cu-Deficient Copper Gallium Selenide Thin Film aS a Photocathode for Photoelectrochemical Water Splitting. *Jpn. J. Appl. Phys.* **2012**, 51,

59. Gueymard, C. SMARTS: Simple Model of the Atmospheric Radiative Transfer of Sunshine. *Natl. Renew. Energy Lab.*

60. Gueymard, C. *SMARTS2, A Simple Model of the Atmospheric Radiative Transfer of Sunshine: Algorithms and Performance Assessment*. **1995**,

61. Gueymard, C. Parameterized Transmittance Model for Direct Beam and Circumsolar Spectral Irradiance. *Sol. Energy* **2001**, 71, 325–346.

62. Hellstern, T. R. *Engineering Catalysts, Interfaces, and Semiconductors for Sustainable Hydrogen Production via Solar Driven Water Splitting*. *PhD Thesis, Stanford University* **2017**,

63. Knöppel, J.; Zhang, S.; Speck, F. D.; Mayrhofer, K. J. J.; Scheu, C.; Cherevko, S. Time-Resolved Analysis of Dissolution Phenomena in Photoelectrochemistry – A Case Study of WO3 Photocorrosion. *Electrochem. Commun.* **2018**, 96, 53–56.

64. Tan, C. S.; Kemp, K. W.; Braun, M. R.; Meng, A. C.; Tan, W.; Chidsey, C. E. D.; Ma, W.; Moghadam, F.; McIntyre, P. C. 10% Solar-to-Hydrogen Efficiency Unassisted Water Splitting on ALD-Protected Silicon Heterojunction Solar Cells. *Sustain. Energy Fuels* **2019**,

65. Wang, Y.; Schwartz, J.; Gim, J.; Hovden, R.; Mi, Z. Stable Unassisted Solar Water Splitting on Semiconductor Photocathodes Protected by Multifunctional GaN Nanostructures. *ACS Energy Lett.* **2019**, 1541–1548.

66. Wang, T.; Liu, S.; Li, H.; Li, C.; Luo, Z.; Gong, J. Transparent Ta 2 O 5 Protective Layer for Stable Silicon Photocathode under Full Solar Spectrum. *Ind. Eng. Chem. Res.* **2019**, 58, 5510–5515.

67. Bae, D.; Pedersen, T.; Seger, B.; Iandolo, B.; Hansen, O.; Vesborg, P. C. K.; Chorkendorff, I. Carrier-Selective p- and n-Contacts for Efficient and Stable Photocatalytic Water Reduction. *Catal. Today* **2017**, 290, 59–64.

68. *Wide-Gap Chalcopyrites*. *Springer* **2006**,

69. Ruckh, M.; Schmid, D.; Schock, H. W. Photoemission Studies of the ZnO/CdS Interface. *J. Appl. Phys.* **1994**, 76, 5945–5948.

70. Weinhardt, L.; Heske, C.; Umbach, E.; Niesen, T. P.; Visbeck, S.; Karg, F. Band Alignment at the I-ZnO/CdS Interface in Cu(In,Ga)(S,Se) 2 Thin-Film Solar Cells. *Appl. Phys. Lett.* **2004**, 84, 3175–3177.

71. Zhang, S. B.; Wei, S. H.; Zunger, A. A Phenomenological Model for Systematization and Prediction of Doping Limits in II-VI and I-III-VI2compounds. *J. Appl. Phys.* **1998**, 83, 3192–3196.

72. Gloeckler, M.; Sites, J. R. Efficiency Limitations for Wide-Band-Gap Chalcopyrite Solar Cells. *Thin Solid Films* **2005**, 480–481, 241–245.

73. Song, T.; Kanevce, A.; Sites, J. R. Emitter/Absorber Interface of CdTe Solar Cells. *J. Appl. Phys.* **2016**, 119, 233104.

74. Minemoto, T.; Matsui, T.; Takakura, H.; Hamakawa, Y.; Negami, T.; Hashimoto, Y.; Uenoyama, T.; Kitagawa, M. Theoretical Analysis of the Effect of Conduction Band Offset of Window/CIS Layers on Performance of CIS Solar Cells Using Device Simulation. *Sol. Energy Mater. Sol. Cells* **2001**, 67, 83–88.

75. Minemoto, T.; Negami, T.; Nishiwaki, S.; Takakura, H.; Hamakawa, Y. Preparation of Zn1-XMgxO Films by Radio Frequency Magnetron Sputtering. *Thin Solid Films* **2000**, 372, 173–176.

76. Ohtomo, A.; Kawasaki, M.; Koida, T.; Masubuchi, K.; Koinuma, H.; Sakurai, Y.; Yoshida, Y.; Yasuda, T.; Segawa, Y. MgxZn1-XO as a II-VI Widegap Semiconductor Alloy. *Appl. Phys. Lett.* **1998**, 72, 2466–2468.

77. Takeuchi, I.; Yang, W.; Chang, K. S.; Aronova, M. A.; Venkatesan, T.; Vispute, R. D.; Bendersky, L. A. Monolithic Multichannel Ultraviolet Detector Arrays and Continuous Phase Evolution in MgxZn1-XO Composition Spreads. *J. Appl. Phys.* **2003**, 94, 7336–7340.

78. Bendersky, L. A.; Takeuchi, I.; Chang, K. S.; Yang, W.; Hullavarad, S.; Vispute, R. D. Microstructural Study of Epitaxial Zn1-XMg XO Composition Spreads. *J. Appl. Phys.* **2005**, 98, 083526.

79. Lautenschlaeger, S.; Sann, J.; Klar, P. J.; Piechotka, M.; Meyer, B. K. Combinatorial Growth of MgxZn1-XO Epilayers by Chemical Vapor Deposition. *Phys. Status Solidi Basic Res.* **2009**, 246, 383–386.

80. Rajbhandari, P. P.; Bikowski, A.; Perkins, J. D.; Dhakal, T. P.; Zakutayev, A. Combinatorial Sputtering of Ga-Doped (Zn,Mg)O for Contact Applications in Solar Cells. *Sol. Energy Mater. Sol. Cells* **2017**, 159, 219–226.

81. Ablekim, T.; Colegrove, E.; Metzger, W. K. Interface Engineering for 25% CdTe Solar Cells. *ACS Appl. Energy Mater.* **2018**, 1, 5135–5139.

82. Chantana, J.; Kato, T.; Sugimoto, H.; Minemoto, T. 20% Efficient Zn0.9Mg0.1O:Al/Zn0.8Mg0.2O/Cu(In,Ga)(S,Se)2 Solar Cell Prepared by All-Dry Process through a Combination of Heat-Light-Soaking and Light-Soaking Processes. *ACS Appl. Mater. Interfaces* **2018**, 10, 11361–11368.

83. Minemoto, T.; Hashimoto, Y.; Satoh, T.; Negami, T.; Takakura, H.; Hamakawa, Y. Cu(In,Ga)Se2 Solar Cells with Controlled Conduction Band Offset of Window/Cu(In,Ga)Se2 Layers. *J. Appl. Phys.* **2001**, 89, 8327–8330.

84. Hultqvist, A.; Platzer-Björkman, C.; Pettersson, J.; Törndahl, T.; Edoff, M. CuGaSe2 Solar Cells Using Atomic Layer Deposited Zn(O,S) and (Zn,Mg)O Buffer Layers. *Thin Solid Films* **2009**, 517, 2305–2308.

85. D. W. Palm, C. P. Muzzillo, M. Ben-Naim, I. Khan, N. G. and T. F. J. Tungsten Oxide-Coated Copper Gallium Selenide Sustains Long-Term Solar Hydrogen Evolution. *Sustain. Energy Fuel* **2020**, Accepted,

86. Flammini, M. G.; Debernardi, N.; Le Ster, M.; Dunne, B.; Bosman, J.; Theelen, M. The Influence of Heating Time and Temperature on the Properties of CIGSSe Solar Cells. *Int. J. Photoenergy* **2016**, 2016,

87. Nishiwaki, S.; Siebentritt, S.; Walk, P.; Lux-Steiner, M. C. A Stacked Chalcopyrite Thin-Film Tandem Solar Cell with 1.2 V Open-Circuit Voltage. *Prog. Photovolt. Res. Appl* 11, 243–248,.

88. Weinhardt, L.; Blum, M.; Bär, M.; Heske, C.; Fuchs, O.; Umbach, E.; Denlinger, J. D.; Ramanathan, K.; Noufi, R. Chemical Properties of the Cu(In,Ga)Se2/Mo/Glass Interfaces in Thin Film Solar Cells. *Thin Solid Films* **2007**, 515, 6119–6122.

89. Nishimura, T.; Hamada, N.; Chantana, J.; Mavlonov, A.; Kawano, Y.; Masuda, T.; Minemoto, T. Application of Two-Dimensional MoSe2 Atomic Layers to the Lift-Off Process for Producing Light-Weight and Flexible Bifacial Cu(In, Ga)Se2 Solar Cells. *ACS Appl. Energy Mater.* **2020**, 3, 9504–9508.

90. Osada, S.; Abe, Y.; Anegawa, T.; Minemoto, T.; Takakura, H. Cu(In,Ga)Se2 Solar Cells with Superstrate Structure Using Lift-off Process. *Sol. Energy Mater. Sol. Cells* 95, 223–226,.

91. Bär, M.; Weinhardt, L.; Heske, C.; Nishiwaki, S.; Shafarman, W. N. Chemical Structures of the Cu (In,Ga) Se2 /Mo and Cu (In,Ga) (S,Se) 2 /Mo Interfaces. *Phys. Rev. B - Condens. Matter Mater. Phys.* **2008**, 78, 1–8.